

1 **Surface-guided computing to analyze subcellular morphology and membrane-associated**
2 **signals in 3D**

3
4 **Authors**

5 Felix Y. Zhou^{1,2}, Andrew Weems^{1,2}, Gabriel M. Gihana^{1,2}, Bingying Chen^{1,2}, Bo-Jui Chang^{1,2}, Meghan
6 Driscoll^{1,2,3} and Gaudenz Danuser^{1,2}

7
8 **Affiliation**

9 ¹Lyda Hill Department of Bioinformatics, University of Texas Southwestern Medical Center, Dallas, TX, USA.

10 ²Cecil H. & Ida Green Center for System Biology, University of Texas Southwestern Medical Center, Dallas,
11 TX, USA

12 ³Current address: Department of Pharmacology, University of Minnesota, Minneapolis, MN, USA

13
14
15
16 **Correspondence**

17 Correspondence to Felix Zhou or Gaudenz Danuser: {felix.zhou, [gaudenz.danuser](mailto:gaudenz.danuser@utsouthwestern.edu)}@utsouthwestern.edu
18

19 Abstract

20 Signal transduction and cell function are governed by the spatiotemporal organization of membrane-
21 associated molecules. Despite significant advances in visualizing molecular distributions by 3D light
22 microscopy, cell biologists still have limited quantitative understanding of the processes implicated in the
23 regulation of molecular signals at the whole cell scale. In particular, complex and transient cell surface
24 morphologies challenge the complete sampling of cell geometry, membrane-associated molecular
25 concentration and activity and the computing of meaningful parameters such as the co-fluctuation between
26 morphology and signals. Here, we introduce u-Unwrap3D, a framework to remap arbitrarily complex 3D cell
27 surfaces and membrane-associated signals into equivalent lower dimensional representations. The
28 mappings are bidirectional, allowing the application of image processing operations in the data representation
29 best suited for the task and to subsequently present the results in any of the other representations, including
30 the original 3D cell surface. Leveraging this surface-guided computing paradigm, we track segmented surface
31 motifs in 2D to quantify the recruitment of Septin polymers by blebbing events; we quantify actin enrichment
32 in peripheral ruffles; and we measure the speed of ruffle movement along topographically complex cell
33 surfaces. Thus, u-Unwrap3D provides access to spatiotemporal analyses of cell biological parameters on
34 unconstrained 3D surface geometries and signals.

36 Main

37 Advances in 3D high-resolution live-cell microscopy and biosensor design enable integrative studies of the
38 dynamic interplay and causal relations between cell morphology and signal transduction *in vitro* and *in vivo*.
39 By reshaping the plasma membrane into diverse morphologies, cells sense, respond to and remodel their
40 local environment¹⁻⁶. Many cell types adopt shapes that are tailored to their characteristic function⁷⁻¹¹. Cell
41 morphology has thus long been recognised as a proxy of cell state and as a marker of differentiation^{9,11,12}.
42 Mechanically, the plasma membrane integrates internal and external forces, which affects cell fate through
43 mechanotransductive proteins and changes in cytoskeleton and nuclear morphology¹³⁻¹⁵. Structurally, the
44 plasma membrane serves as a platform for catalysing chemical reactions¹⁶⁻²⁰ and as a spatiotemporal
45 organiser of signalling activity through the creation of binding sites, local confinements and molecular
46 concentration in scaffolds, diffusion traps, and by phase separation^{16,21-23}. These reactions occur locally at
47 the nanometer or micron length scale or in global bursts that span the entire cell^{18,24}. Understanding the
48 salient biophysical processes that govern the formation and persistence of these subcellular signalling
49 domains and how these domains regulate biochemical signal transduction remains enigmatic. Systematic
50 identification of this intricate regulatory interplay between cell shape and molecular signalling necessitates
51 consistent temporal tracking of the local 3D cell geometry and conjoint sampling of the corresponding
52 membrane-associated molecular concentration and activity.

53
54 Cell surfaces are extracted from binary segmented image volumes and stored as a mesh, a data structure
55 described by a list of the Cartesian 3D vertex coordinates on the surface and a second list specifying how
56 the individual vertices are connected into triangles or faces. Tracking the correspondence between two 3D
57 surface meshes is an active area of research in computer graphics²⁵⁻²⁸ and none of the methods have been
58 adopted to cell imaging. A particular technical challenge that arises when adapting techniques from computer
59 graphics with applications to cell biology is the non-convexity, irregularity and high curvature of surface
60 protrusions on most cell shapes. Very few methods have been proposed to accurately follow such geometries
61 over time and have largely been demonstrated on well-defined shapes such as human pose²⁹ or hands^{30,31}.
62 Generally, these methods track by matching meshes from consecutive timepoints. To match meshes,
63 methods attempt to assign a unique signature per vertex or face to establish a matching between vertices
64 and faces by minimizing a loss metric^{32,33}. However, this approach is inherently sensitive to mesh quality,
65 uniqueness of the signature, optimizer convergence and is difficult to generalize when tracking surfaces over
66 many timepoints. Crucially, meshes segmented from two different timepoints have different numbers of
67 vertices and faces and the lack of the exact same surface features poses ambiguity in matching. Alternatively,
68 individual 3D image volumes may be first registered spatiotemporally before mesh extraction, as is done in
69 neuroscience³⁴⁻³⁷. This approach is robust to mesh quality and sampling errors, however deformations must
70 be small between timepoints. For example, long or thin cell surface structures such as lamellipodia and
71 filopodia suffer voxel undersampling, limiting the registration to cell surfaces with largely globular features
72 such as blebs³⁸. This problem could be remedied by mapping the 3D surface to the unit sphere³⁹⁻⁴¹. Indeed,
73 in macroscopic imaging application, this procedure has enabled registration of complex geometrical features
74 such as brain folds directly on the 3D sphere or in derivative 2D unwrapped images^{27,42-44}. Unfortunately, this
75 strategy requires closed surface topologies with no holes (genus-0 surfaces), which is not generally
76 guaranteed in live-cell microscopy. Alternatively, one can selectively segment surface motifs and track these
77 in 3D whilst mapping surface-proximal molecular signal intensity^{38,45-47}. Like the 3D surface tracking, this

78 approach is also susceptible to the variable quality of the segmented motifs used for matching and non-
79 convexities of the surface.

80
81 Here, we develop a general and comprehensive software solution, u-Unwrap3D, for surface-guided
82 computing. u-Unwrap3D remaps arbitrarily complex 3D subcellular morphology and membrane associated
83 signals to equivalent lower dimensional representations that allow for optimized computation of surface
84 features and spatiotemporal tracking and sampling of cell geometry and associated molecular entities. We
85 demonstrate the power of this approach in applications to i) the unsupervised segmentation of diverse surface
86 motifs; ii) the quantification of septin polymer recruitment to dynamic cell surface blebs and iii) the
87 measurement of travel speed of actin-enriched surface ruffles.

88 89 Results

90 91 u-Unwrap3D for surface-guided computing

92 Given an input Cartesian 3D surface $S(x, y, z)$ as a 3D mesh, u-Unwrap3D computes a series of equivalent
93 surface representations (Fig. 1a, Suppl. Video 1). The input surface $S(x, y, z)$ is smoothed to find a genus-
94 0 reference surface $S_{\text{ref}}(x, y, z)$ and then mapped to the sphere, $S^2(x, y, z)$, unwrapped into a 2D $S_{\text{ref}}(u, v)$
95 using UV-unwrapping and the (u, v) parameterized $S_{\text{ref}}(x, y, z)$ propagated along the steepest gradient of its
96 signed distance transform to construct a topographic representation of the input surface, $S(d, u, v)$. The
97 mappings between representations are bijective and constructed to minimize the associated conformal
98 (preservation of aspect ratio) and equiareal (preservation of surface area fraction) errors⁴⁸ (Extended Fig.
99 1a,b). We denote $S(\cdot)$ and $V(\cdot)$ as surfaces and volumes, respectively, relative to a coordinate system
100 indicated in brackets. The variables $F_i(S(\cdot))$ and $I_i(V(\cdot))$ denote surface- and volume- associated signals of
101 interest. These signals may describe geometrical quantities, (like mean curvature, H), integer labels (like
102 segmented surface protrusions) or molecular activities (like molecular concentrations or activities). Thus, u-
103 Unwrap3D provides a framework to map these variables between different surface representations, each of
104 which is suited for different computational tasks.

105
106 **Step 1** iteratively smoothens out salient surface features on $S(x, y, z)$ using conformalized mean curvature
107 flow (cMCF)⁴⁹ to determine a genus-0 reference surface $S_{\text{ref}}(x, y, z)$ without holes or ‘handles’. The term
108 ‘handle’ refers to the holes in a loop mesh structure such as the handle of a teacup that unlike ‘holes’ does
109 not involve missing/incomplete surface patches in a mesh. cMCF iteratively displaces vertices with a speed
110 proportional to the mean curvature at each vertex (Extended Fig. 1c). The input surface is thereby
111 preferentially deformed into the largest inscribable sphere. In the absence of *a priori* markers for the reference
112 shape such as cell cortex markers, the rate of decrease in mean absolute Gaussian curvature K is monitored
113 to determine a stopping iteration (Methods). The Gaussian curvature K is a shape-invariant measure of local
114 curvature. Accordingly, the same shape (e.g. a sphere) has identical K value irrespective of size⁵⁰. K is thus
115 well-suited as a criterion to terminate the cMCF iterations. cMCF is agnostic to minor mesh imperfections
116 such as small holes and handles but does not change the genus. Any holes or handles in the input surface
117 are still present. However, because of the smoothing, these holes are more regular and smaller. Still in Step
118 1, we compute a genus-0 mesh of the reference surface $S_{\text{ref}}(x, y, z)$ through filling all holes in the volume
119 enclosed by the intermediary cMCF-processed surface and remeshing of the resulting body (Methods). The
120 remeshing changes the vertex position and face topology. To restore bijectivity between the input surface
121 $S(x, y, z)$ and $S_{\text{ref}}(x, y, z)$ we match the mesh $S_{\text{ref}}(x, y, z)$ with the mesh of the intermediary cMCF-processed
122 surface that is bijective to $S(x, y, z)$, (Methods). Any associated measurements $F_i(S(x, y, z))$ are mapped to
123 $F_i(S_{\text{ref}}(x, y, z))$ by interpolation. In **Step 2**, the genus-0 reference surface, $(S_{\text{ref}}(x, y, z))$ is quasi-conformally
124 mapped to the unit sphere without folds^{39,51} (Extended Fig. 1d). This spherical parametrization is denoted
125 $S_{\Omega}^2(x, y, z)$. Per the uniformization theorem, such a mapping always exists for a genus-0 surface⁵²⁻⁵⁵. The
126 quasi-conformal spherical parameterization $S_{\Omega}^2(x, y, z)$ severely shrinks surface extremities deviating from the
127 sphere²⁷, even for roughly globular shapes (Extended Fig. 1d). Consequently, surface features with high
128 curvature are undersampled and disproportionately represented relative to their original Cartesian 3D surface
129 area. This can detrimentally affect downstream analyses such as segmentation and tracking²⁷. To mitigate
130 this problem, we iteratively diffuse in **Step 3** the area distortion factor per face by advecting vertex positions
131 on the sphere²⁷ at the expense of increased conformal error (Extended Fig. 1e). In **Step 4**, this quasi-
132 equiareal sphere $S_{\Omega}^2(x, y, z)$ is bijectively unwrapped to the 2D plane, $S(u, v)$, using equirectangular projection,
133 in short UV-mapping, with (u, v) denoting the spherical polar and azimuthal angles, respectively. UV-
134 mapping introduces the strongest distortions to signals at the north and south poles of the sphere. To visualize
135 features of interest with minimal distortion, u-Unwrap3D optionally infers a rotation matrix based on a

weighted principal component analysis of surface variables, such as the local curvature (Extended Fig. 1f,g, Methods). If the input Cartesian 3D surface mesh $S(x, y, z)$ is genus-0, the generation of a reference surface, $S_{\text{ref}}(x, y, z)$ may be skipped and 2D equiareal surface unwrapping realised directly (Fig. 1b, Suppl. Video 2). We note that an input genus-X Cartesian 3D surface $S(x, y, z)$ is also directly unwrapped into 2D through steps 1-4 of u-Unwrap3D, but not in an equiareal manner (Extended Fig. 1h). In **Step 5**, the first part remaps the Cartesian 3D volume $V(x, y, z)$ and associated signals $I_i(V(x, y, z))$ into a topographic volume $V(d, u, v)$ coordinate system that is normal to the reference surface, $S_{\text{ref}}(x, y, z)$. The second part establishes a bijective mapping of (d, u, v) to (x, y, z) coordinates, $S_{\text{ref}}(u, v)$, i.e. the (u, v) parameterized reference surface of $S_{\text{ref}}(x, y, z)$, is propagated in Cartesian 3D space in the surface normal direction at equidistant steps of α voxels along the steepest gradient of the signed distance function, $\nabla\Phi(x, y, z)$, for a total of D steps. Interpolation of the respective Cartesian volumetric signal intensities, $I_i(V(x, y, z))$ at the (x, y, z) coordinates indexed by (d, u, v) generates the topographic 3D volume equivalents, $I_i(V(d, u, v))$. Finally, in **Step 6** the topographic 3D surface representation, $S(d, u, v)$ of the input surface $S(x, y, z)$ is obtained by surface meshing the topographic binary volume segmentation.

In summary, u-Unwrap3D generates bijective mappings of a given genus-X surface between 5 equivalent surface representations; Cartesian 3D, $S(x, y, z)$, genus-0 reference 3D, $S_{\text{ref}}(x, y, z)$, the unit 3D sphere, $S^2(x, y, z)$, topographic 3D, $S(d, u, v)$, and the 2D plane image, $S(u, v)$ (Fig. 2a), while simultaneously transforming Cartesian 3D to topographic 3D volumes (Fig. 2b). This was made possible by two crucial choices; the use of cMCF and voxelization to construct a genus-0 reference surface, $S_{\text{ref}}(x, y, z)$ to realise spherical parameterization (Step 1) and the implementation of an efficient numerical scheme to relax area distortion on the 3D sphere (Step 3). The former allows us to construct $S_{\text{ref}}(x, y, z)$ as a proxy of the genus-X $S(x, y, z)$ surface mesh and to unwrap this 3D surface into one 2D (u, v) image, instead of requiring multiple 2D (u, v) images, which simplifies downstream analysis⁵⁶⁻⁵⁹. The latter ensures that the unwrapped 2D (u, v) image captures the salient surface features of $S_{\text{ref}}(x, y, z)$, and by extension the genus-X $S(x, y, z)$ surface. Importantly, the bijectivity of the mappings guarantees that for any point on any of the surface or volume representations matching points exist on any of the other surfaces or volumes. Moreover, the bijectivity guarantees preservation of the point topology, i.e. a series of points ordered in clockwise fashion on one surface representation maps to a series of points ordered in the same way on any of the other surface representations and preserves the local neighbourhood relationships. As a result, we can apply mathematical operations defined in any one of the representations and map the results to any other. u-Unwrap3D thus supports the optimal spatiotemporal analysis of unconstrained surface geometries and associated signals.

Validation of u-Unwrap3D on diverse surface motifs

We validated the generality and performance of u-Unwrap3D by application to 66 single cell images acquired by high-resolution light sheet imaging^{45,60}. The dataset span morphologically diverse cells with blebs, lamellipodia and filopodia. The cell surfaces were meshed with marching cubes and segmented within the u-Shape3D software⁴⁵. Small errors in the initial segmentation and meshing process cause high-order genus surfaces with topological holes and handles, which cannot be unwrapped directly (Extended Fig. 2a). Holes can also generate non-watertight surface meshes – surfaces that are not closed and have no clearly defined inside volume^{48,61} possessing potentially complex internal volumetric structures that violate the assumptions of standard 3D mesh processing algorithms.

We first tested the number of input cell surfaces for which u-Unwrap3D could successfully run all steps 1-6 and compute all 5 of the representations as a measure of generality and robustness. Notably only 6/66 (11%) input cell surfaces were genus-0 and only 36/66 (55%) were watertight (Extended Fig 2b). In 63/66 cases, (>95%) we successfully ran all steps and obtained all representations (Extended Fig 2b). The three failures occurred in scenarios, in which the holes and handles remaining after the application of cMCF were still too large for the volume dilation to generate a genus-0 reference surface after remeshing (Fig. 1b, Step 1) (Extended Fig. 2c). In all successful cases, cMCF and binary voxelization under volume dilation generated genus-0 reference surfaces within a median of 10 iterations (Extended Fig 2c, c.f. lamellipodia). Fig. 2c shows extracted representations for challenging examples with blebs, lamellipodia and filopodia (Suppl. Video 3-5).

We next tested the robustness and performance of the $S_{\text{ref}}(x, y, z)$ spherical parameterizations, (Fig. 1b, Steps 2-3). Extended Fig. 3a confirms that the quasi-conformal spherical parameterization (Step 2) minimizes the conformal error to the ideal value of 1, with the largest error in cells with filopodia (1.016 ± 0.013). We also verified the need to relax local area distortion. Whilst quasi-conformal spherical parameterization $S_{\Omega}^2(x, y, z)$ is equiareal for blebs (0.978 ± 0.037), the median area distortion showed that the surface fraction of lamellipodia was down to 0.432 and in filopodia to just 0.140 with respect to their original area fraction on the

reference 3D, $S_{\text{ref}}(x, y, z)$ surface, let alone $S(x, y, z)$. Our scheme for area distortion relaxation (Methods) produces a quasi-equiareal spherical parameterization (Step 3) in blebs (0.985 ± 0.012), and successfully achieves the ideal value of 1 in lamellipodia (1.000 ± 0.000) and filopodia (1.000 ± 0.001), within a maximum median of 23 iterations for lamellipodia (Extended Fig.3b, Table i). We further tested the ability of our relaxation scheme to balance the trade-off between the two extremes of conformal to equiareal spherical parameterizations using different stopping criteria (Extended Fig.3b, Table ii-iv). The initial parameterization without any area-distortion relaxation (iteration 0) is by design conformal but also found to satisfy the most isometric parameterization (MIP)⁶². Running for $t_{\Omega} <$ a maximum of 50 iterations yields an equiareal parameterization for all motifs. At $t \approx \frac{1}{2} t_{\Omega}$ iterations the relaxed mesh jointly minimizes the summation ($Q + \ln \lambda$, Methods) of conformal (Q) and area distortion (λ) errors. At $t \lesssim t_{\Omega}$ iterations the relaxed mesh is the area-preserving MIP⁶³. As expected, this latter parameterization does not fully minimize area distortion (blebs (0.997 ± 0.011), lamellipodia (0.979 ± 0.005) and filopodia (0.980 ± 0.028)) but exhibits slightly lower conformal errors and consequently higher quality faces than a pure equiareal mapping.

Lastly, we tested how accurately $S_{\text{topo}}(x, y, z)$, which defines the topographic 3D mesh, $S(d, u, v)$ (step 5) mapped back into Cartesian coordinates -reconstructs the input surface, $S(x, y, z)$. For all cells, $S(d, u, v)$ was computed with a (u, v) image grid size of 1024×512 pixels. The aspect ratio, $2N \times N$ ($N = 512$) was chosen to preserve the ratio between the equatorial circumference and the length of the arc between north and south poles of a sphere. Compared to the input surface $S(x, y, z)$, $S(d, u, v)$ is lower genus and provides higher face quality (Extended Fig. 3c). We assessed the discrepancy between $S_{\text{topo}}(x, y, z)$ and $S(x, y, z)$ using 4 metrics; Chamfer distance (CD), sliced Wasserstein distance (SW_1)⁶⁴, and differences in total surface area (ΔA) and volume (ΔV) (Extended Fig. 3d, Methods). Considering inevitable rasterization errors when mapping the floating-point precision 3D sphere $S_{\Omega}^2(x, y, z)$ to $S(u, v)$ defined on an integer (u, v) image grid, we measured low vertex position errors according to CD and SW_1 . Cells with lamellipodia had the lowest error (median CD=1.77 voxel, $SW_1=0.93$ voxel) and cells with blebs were slightly worse (median CD=2.79 voxel, $SW_1=4.28$ voxel), likely due to their intrinsically small height (small topographic d). As one would expect, cells with long, thin filopodia displayed the largest discrepancies (median CD=10.33 voxel, $SW_1=18.45$ voxel). Correspondingly we measured a small ΔA (+1.2%) and ΔV (+7.9%) for cells with lamellipodia. ΔA was larger for cells with blebs (-11.6%) and measured to be too large for filopodia (-55.3%) when compared to ΔV differences measured after making $S(x, y, z)$ watertight (+4.2% blebs, +3.4% filopodia). Visualization of exemplar cells show good geometric correspondence between $S_{\text{topo}}(x, y, z)$ and $S(x, y, z)$ (Extended Fig. 3e). Salient surface features were largely captured, albeit smoothed and blurred in $S_{\text{topo}}(x, y, z)$ when local surface regions were underrepresented due to being distant relative to $S_{\text{ref}}(x, y, z)$ (Extended Fig. 3e, black triangles, 1st row blebs and 4th row lamellipodia). Most of the primary morphological features, namely the length and thickness of long, thin filopodia (Extended Fig. 3e, green triangles), except those located both densely together and distant relative to $S_{\text{ref}}(x, y, z)$ (Extended Fig. 3e, red triangles), were captured. u-Unwrap3D was able to capture both the complex lamellipodia folds and curved cell bodies to high accuracy (Extended Fig. 3e, row 2,4). Closer inspection of $S_{\text{topo}}(x, y, z)$ and $S(x, y, z)$ in these cells traced a large ΔA to meshing errors in the input surface $S(x, y, z)$, which caused internal volumetric structures to be merged into the cell surface representation, and overestimation of total surface area. These errors affect the CD and SW_1 to lesser extent.

In summary, our results demonstrate that u-Unwrap3D is robust and applicable to process unconstrained geometries. For maximum resolution of high curvature surface features, a genus-0 reference surface $S_{\text{ref}}(x, y, z)$ proximal to the input surface $S(x, y, z)$ is recommended with a large (u, v) grid size N and small α step_sizes when propagating $S_{\text{ref}}(u, v)$. However, these choices depend on the quality of the input surface mesh $S(x, y, z)$, which depends on the robustness of cell segmentation in the face of noisy image raw data.

u-Unwrap3D enables unsupervised instance segmentation of subcellular surface motifs

The unbiased identification and segmentation of individual protrusive features in unconstrained 3D surface geometries is nontrivial. Cellular protrusions present complex morphological characteristics that are difficult to define descriptively. Even well-known morphological motifs exhibit significant heterogeneity and ambiguity. Not all blebs are spherical, lamellipodia are often plate-like with high curvature ridges but otherwise have no readily-defined shape prior, and filopodia, though long and thin, can sprout haphazardly from elevated 'stumps' or even off of each other. In areas of dynamic and dense protrusions, where does one protrusion start and another end? Consequently, most existing approaches focus on particular surface features of interest such as 'ridge' networks that can be segmented by designed imaging filters or through trained semantic segmentation, with morphological processing and parameter tuning^{46,47,65,66}. With u-Shape3D we

introduced a multi-class morphological motif detection by partitioning the 3D surface into convex patches and applying support vector machines trained with expert annotation to classify the patches into pre-specified motif types⁴⁵. However, this approach cannot detect and segment all protrusions generally, only the limited motifs for which the supervised classifier has been trained on. Lastly, even after obtaining the segmentations, how do we systematically measure salient protrusion properties? For example, with respect to what reference surface should protrusion height be measured? Where is the protrusion width to be measured? How is the internal volume of a protrusion determined?

These segmentation and characterization problems can be significantly better defined in the topographic 3D surface representation $S(d, u, v)$, which captures in one field-of-view all surface features protruding normally to $S_{\text{ref}}(x, y, z)$. As d preserves the total Cartesian 3D curvilinear distance from $S(x, y, z)$ to $S_{\text{ref}}(x, y, z)$ along the gradient of steepest descent we can formally define a 'protrusive' feature as having a d -coordinate greater than that of a reference topographic surface, $S_{\text{ref}}(d_{\text{ref}}, u, v)$, and measure the protrusion height as the difference, $h = d - d_{\text{ref}}$. For example, protrusive features could be specified as those having $h > \bar{h}^{\text{cMCF}}$, the mean height of $S(d, u, v)$ relative to the planar topographic 3D cMCF surface $S_{\text{ref}}^{\text{cMCF}}(d, u, v)$ (i.e. $d_{\text{ref}} = f(u, v) = 0$). However, this definition leads to under-segmentation (Extended Fig. 4a). A remedy would be an intermediate surface $S_{\text{ref}}(d_{\text{ref}} = f_{\text{smooth}}(u, v), u, v)$, which interpolates between the input rugged topographic cell surface, $S(d, u, v)$ and the 2D planar cMCF cell surface $S_{\text{ref}}^{\text{cMCF}}(d, u, v)$, (Fig. 3a,b). Whereas this problem is difficult to frame in Cartesian 3D, in the topographic space the interpolation can be solved naturally by using asymmetric least squares (ALS) optimization with a Whittaker smoother^{67,68}, where the asymmetric weights allow us to account for the heterogeneous protrusion height; and the desired level of surface smoothness can be incorporated as a regularization term (Extended Fig. 4b, Methods). To use ALS, we create a (u, v) -parameterized approximation of $S(d, u, v)$ with $d \simeq f(u, v)$ using straightforward image processing procedures (Extended Fig. 4b, Methods). By exploiting these properties of the topography space, we developed a general approach to segment any protrusion motif including blebs, lamellipodia and filopodia (Extended Fig. 4c,d) with minimal heuristic parameters to tune. Importantly, we did not need to design specialized image filters^{65,66}, compute and cluster feature descriptors^{46,69-71}, or require data training⁴⁵⁻⁴⁷.

We demonstrate the segmentation of individual protrusion instances, capturing motifs identified by uShape3D, but without the need for training annotations. By construction, in topographic 3D (d, u, v) space all surface protrusions are oriented upwards with increasing d . Moreover, the tops of protrusions are individually separated as local regions of high topographic mean curvature, which we identify by thresholding and applying connected component labelling in the topographic volume, $V(d, u, v)$ (Fig. 3c). Mapping the segmented regions back onto the topographic mesh $S(d, u, v)$, we diffuse these initial 'seed' labels across the surface using a combined geodesic distance and dihedral angle affinity matrix to naturally segment the 'stem' of the individual protrusions (Methods). The dihedral angle measures the discontinuity in local mean curvature. It incorporates the prior intuition that the boundaries of a label should expand faster on local surfaces of homogeneous curvature such as that on a 'hill', compared to another label experiencing large curvature differences in its local surface region, such as in a valley between multiple 'hills'. The combined affinity matrix thus introduces a morphology-aware competition between segmentation labels and provides a biophysical rationale for defining which surface patches belong to individual 'seed' protrusions. Furthermore, the dihedral angle is large between a protrusion and the main cortical cell surface and thus serves as a soft stopping criteria for diffusion (Extended Fig. 4d) in addition to applying the binary protrusion segmentation from above. Lastly, we filter out protrusions that are too small and close any small holes using the Cartesian 3D surface area. The final segmentation result qualitatively and quantitatively agrees with that obtained by supervised u-Shape3D for lamellipodia (Fig. 3d) but yields more contiguous labels and is less prone to over-segmentation (Fig. 3e). Importantly, this segmentation strategy is applicable, even when not all protrusions are equiareally represented in $S(d, u, v)$, as shown by the segmentation of the majority of blebs and filopodia in exemplar cells (Extended Fig. 4d).

Individual segmented protrusions are genus-0 open-surface 3D submeshes that can be directly mapped to the 2D plane (Fig. 3f). This allows us to further refine the segmentation, for example, by detecting and splitting under-segmented blebs by a gradient watershed algorithm (Methods). Thanks to bijectivity, the refined segmentation labels can be transferred back onto the original surface mesh (Fig. 3f,g, c.f. before and after refine, black triangles). Both the before (adjusted normalized mutual information, NMI=0.57) and the after refinement (adjusted NMI=0.54) segmentations agree with u-Shape3D. However, u-Unwrap3D segmented blebs are more complete, with more blebs of larger surface area (150 blebs in total). In contrast, u-Shape3D over-segments small blebs (742 blebs) that were found to originate from erroneous meshing of internal structures in $S(x, y, z)$ (see Extended Fig.3e). This example illustrates the potential pitfalls of identifying motifs from local surface patches only with potentially imperfect input 3D meshes. In contrast, with u-Unwrap3D any

314 surfaces internal to the cell volume are readily removed when mapped into topography as these surfaces
315 have d -coordinates less than the reference surface, $S_{\text{ref}}(d_{\text{ref}} = f_{\text{smooth}}(u, v), u, v)$.

316
317 Finally, the representation $S(d, u, v)$ enables partitioning of the input cell volume into the sum of a reference
318 volume representing the underlying cortical cell body and the unique volume occupied by individual
319 protrusions (Fig. 3h). We do so by (u, v) -parameterizing the reference cortical surface submesh, $S_{\text{ref}}(d, u, v)$
320 after removing all individual protrusion submeshes as a grayscale image such that the pixel intensity value
321 at (u, v) is the respective d -coordinate, and inpainting the missing d -coordinates at (u, v) coordinates
322 corresponding to the subtracted protrusions to generate a full reference binary volume (Extended Fig. 4e,
323 Methods). For the protrusions, we first devised a marker-controlled lateral watershed depth propagation to
324 diffuse the surface-based protrusion segmentation labels uniquely throughout the full topographic (d, u, v)
325 space slice-by-slice, top-to-bottom (Extended Fig. 4f). Then, individual protrusion volumes were generated
326 by masking the propagated label volume with the reference binary volume (Extended Fig. 4g). We compared
327 our topography-guided decomposition strategy to a fully Cartesian 3D mesh processing approach whereby
328 individual protrusion submeshes were first closed by constructing a surface patch that minimized the local
329 bending (or harmonic) energy⁷² (Methods). The closed reference volume was then generated using all such
330 patches to impute the residual holes in the raw reference surface. Fig. 3i panels i-ii show that the computed
331 surface area (slope=0.90) and volume (slope=0.95) of individual protrusions are similar for both methods.
332 However, the 3D mesh processing protrusions consistently under-measure larger protrusions. Crucially, the
333 imputed reference volume appears artefactual. Where protrusions were located, the surface is overly smooth,
334 and even involuted. These regions contrast starkly with non-imputed surface areas between protrusions,
335 creating artificial 'peaks' and 'ridges' of high mean curvature (black arrows). In comparison, the topography-
336 guided reference volume is mechanically more plausible.

337
338 In summary, the ability to map freely between topographic and Cartesian 3D surfaces and their respective
339 volumetric representations enabled us to design simple and generalizable methods to detect and segment in
340 an unsupervised fashion individual morphological motifs from unconstrained surface geometries. To
341 bijectively map the topographically segmented surface protrusion labels onto the 2D plane, which is an
342 optimal representation for tracking the segmented motifs, we developed a topographic cMCF for u-Unwrap3D
343 (Fig. 3j, Suppl. Video 6, Methods).

345 **u-Unwrap3D enables tracking of 3D subcellular surface motifs and molecular activity in 2D**

346 A central goal of live cell imaging in 3D is to visualize the spatiotemporal relations between molecular activities
347 and cell behaviors, including morphodynamic outputs. Progress has been made on software developments
348 that allow unbiased and statistically meaningful analysis of cell morphology and molecular
349 distributions^{45,47,60,73,74}. However, to remain algorithmically and computationally tractable these pipelines have
350 been restricted to quasi-static representations of dynamic processes. Surface-guided computing with u-
351 Unwrap3D allows us now to remedy this limitation. Dynamic behaviours on complex 3D cell shapes, including
352 their morphological and molecular signal activity changes, can be mapped to 2D representations where
353 powerful analytical pipelines exist for spatiotemporally consistent tracking. Results can be statistically
354 evaluated and, if of interest, be visualized in 3D by leveraging the bijective properties of u-Unwrap3D
355 mappings. Fig. 4 and 5 demonstrate this capacity based on two examples.

357 **Individual blebs dynamically recruit Septins to local surface regions during retraction**

358 We first analysed potential relations between dynamic surface blebbing and the recruitment of Septins. Blebs
359 are globular membrane protrusions of 1-2 μm diameter that are thought to extend in areas of localized
360 membrane detachment from the actin cortex^{75,76}. Intracellular pressure expands the budding blebs outward,
361 followed by rapid assembly of a contractile actomyosin network that yields retraction. Cycles of protrusion
362 and retraction have been described to last a few tens of seconds. Associated with the cycles are molecular
363 activities both driving and responding to the morphological dynamics. One such process is the assembly of
364 Septin protein polymers at sites of negative curvature (from a cell-external perspective) emerging at the bleb
365 necks. Our previous work³⁸ has shown that disrupting the bleb cycle diminishes Septin assembly at the cell
366 surface. Here we now exploit the ability of u-Unwrap3D to track individual bleb cycles and quantify Septin
367 accumulation by remapping surface morphology and a fluorescent marker of Septins to an appropriate 2D
368 representation. We acquired 3D volumes of SEPT6-GFP-expressing MV3 melanoma cells every 1.2s for 200

369 timepoints. As the cortical cell body exhibits little temporal variation and blebs protrude normally to the surface,
370 the temporal mean cell surface, $\bar{S}(x, y, z)$ is a good proxy of the cell cortex. We apply u-Unwrap3D to $\bar{S}(x, y, z)$
371 to create a common static (d, u, v) coordinate space for computing topographic 3D $S(d, u, v)$ and 2D planar
372 $S(u, v)$ representations for each timepoint. $\bar{S}(x, y, z)$ was computed by meshing the mean binary volume
373 across individual binary voxelizations of the cell surface over all 200 timepoints (Methods). Note the
374 construction of a common topographic space from a single mesh for a timelapse is computationally efficient
375 but applicable only if cell shape changes lie within the Cartesian subvolume mapped by the topographic
376 space. For large shape changes u-Unwrap3D should be applied to individual timepoints and spatiotemporal
377 registration used to align surfaces to a common reference using $S_{\text{ref}}(x, y, z)$ or $S(u, v)$ representations. The
378 segmentation tools discussed above were used to detect all bleb instances from $S(d, u, v)$ and mapped to
379 $S(x, y, z)$ and $S(u, v)$ for each timepoint (Fig. 4a, Suppl. Video 7). Similarly, the computed mean curvature
380 and the normalized Septin intensity surface signals $F_i(S(x, y, z))$ from Cartesian 3D were mapped to
381 topographic 3D $F_i(S(d, u, v))$ and into 2D, $F_i(S(u, v))$, to enable simple bleb tracking and timeseries analysis.

382

383 To track blebs in 2D we computed the bounding box of individual bleb instances in every timepoint after
384 appropriate image padding to account for spherical periodicity (Fig. 4b left). In $S(u, v)$ bleb dynamics can
385 readily be followed by an established 2D multi-object bounding box tracker⁷⁷ with mean curvature optical
386 flow-guided bipartite matching (Fig. 4b middle, Methods). The bijective mapping allows us to map the
387 resulting trajectories from (u, v) coordinates (individually colored) to (x, y, z) coordinates to generate bleb
388 tracks in Cartesian 3D (Fig. 4b right, Suppl. Video 7). Due to the fast temporal acquisition rate, only a northern
389 portion of the cell can be maintained in-focus. Again, u-Unwrap3D's bijectivity between 3D and 2D
390 representation enabled us to easily map a manually annotated out-of-focus subvolume onto $S(x, y, z)$ and
391 into $S(u, v)$ to retain for analysis only the bleb tracks that remain within the in-focus surface regions (Fig. 4c).
392 The distribution of individual bleb track lifetimes showed a peak at 14s and a long tail up to 240s, suggestive
393 of a mixture of short- and long-lived blebs (Fig. 4d). The mean bleb lifetime of 27s corresponded well with a
394 30s periodicity given by the first peak of the temporal autocorrelation of mean curvature $H(S(x, y, z, t))$ in
395 Cartesian 3D (Fig. 4e). This validates at the population level the accuracy of single bleb tracking after
396 projection and segmentation of mean surface curvature in 2D.

397 The temporal autocorrelation curves of mean curvature and Septin intensity showed a high level of similarity,
398 suggesting co-fluctuation of the two surface signals. Indeed, we had previously shown that surface regions
399 of high Septin intensity with negative surface curvature for at least 30s display a correlation between negative
400 curvature value and Septin intensity³⁸. Whilst the majority of Septin pulses endured only one cycle of bleb
401 formation and retraction, *de novo* formation of stable Septin structures appeared to be driven by several
402 Septin pulses occurring in short succession. We thus hypothesized that these were formed by iterative bleb-
403 driven curvature generation events resulting in local levels of Septin oligomers surpassing a threshold
404 necessary for inter-oligomer polymerization and enabling stabilization through formation of higher-order
405 structures³⁸. The ability to spatiotemporally track individual blebs enabled us now to quantitatively test this
406 model. For the duration of each tracked bleb, we sampled within the 2D bounding box distortion-corrected
407 timeseries of bleb surface area, on-/off- bleb surface mean curvature and Septin intensity (Methods). We
408 used the 2D $S(u, v)$ bounding box to define a bleb's spatial area-of-influence and its surface area. The
409 Cartesian 3D $S(x, y, z)$ box area was taken as the bleb's 3D surface area in each tracked frame. Within the
410 2D bleb bounding box, 'on-bleb' is the largest spatially contiguous region of high mean curvature. The
411 remainder area is 'off-bleb'. A single curvature threshold was computed by 3-class Otsu thresholding over all
412 $H(S(u, v, t))$ to define the regions of low/high mean curvature in $S(u, v, t)$. Using the extracted timeseries we
413 reconstructed the temporal profile of bleb area, on-/off- mean curvature and Septin intensity of a single mean
414 bleb event in a window of 35s centered on the timepoint of maximum bleb area averaged over 545 single
415 bleb events from 480 bleb tracks. We sample ± 17.5 s before and after the timepoint of maximum bleb area
416 to exceed the 30s periodicity inferred from temporal autocorrelation by 5s and capture the full dynamics. We
417 then broke the mean timeseries into four distinct temporal phases of bleb-mediated Septin recruitment, each
418 ≈ 5 s long (Fig. 4f labels A-D). In phase A, the bleb begins to expand, increasing its surface area, accompanied
419 by a sharp increase in on-bleb H and a decrease in Septin intensity as the plasma membrane detaches from
420 the actin cortex. The expansion also reduces off-bleb H , causing a decrease in Septin intensity off-bleb,
421 presumably due to disrupting Septin structures. In phase B, the bleb reaches maximum size and then begins
422 to retract with decreasing surface area. Interestingly, unlike mean curvature, which begins to decrease before
423 the maximum bleb area, the change in area is symmetrical, occurring ± 2.5 s relative to the time of maximum
424 bleb area. Coincident with the bleb increasing to a maximum area, off-bleb H decreases to a minimum and

Septin intensity both on/off bleb stabilizes at a minimum. As the bleb retracts and the actin cytoskeleton reassembles, off-bleb H increases and Septin intensity begins to increase both on/off bleb. In phase C (+2.5s to +8.0s after peak bleb area), the bleb area continues to decrease but at a slower rate. Unexpectedly, the off-bleb negative curvature H plateaus at a value lower than its starting value (before phase A) instead of continuing to increase. Concurrently, Septin intensity undergoes the greatest rate of increase on both on-bleb and off-bleb surfaces such that at the end of phase C, the Septin intensity is at the levels before phase A (c.f. -15s to -10s). In phase D (+8.0s to +14.0s), bleb area and on/off-bleb H recover to pre-expansion levels while Septin intensity continues to increase before plateauing on both on/off-bleb surfaces. Beyond phase D, the next bleb cycle begins, with similar temporal characteristics to phase A. Altogether these results indicate that blebs generate optimal curvature dynamics during retraction to recruit Septin polymers to the surface regions around blebs. Moreover, the data support our model of Septins being recruited to negative curvature patches in a cyclic fashion, where each bleb formation-retraction drives the local accumulation of a few more oligomers until a threshold concentration is reached to trigger inter-oligomer polymerization of a stable Septin assembly. Notably, none of these observations could have been made without u-Unwrap3D.

Ruffles are driven by locally enriched filamentous actin and migrate actively on the cell surface

We also applied the capacity of u-Unwrap3D to examine putative relations between the dynamics of membrane ruffles, filamentous actin and surface actin retrograde flow. Membrane ruffles are thin, rapidly-moving, actin-rich protrusions^{78,79}. They are thought to play a role in cell migration, and it has been proposed that ruffles arise as a consequence of inefficient adhesion in cellular lamellipodia⁸⁰. Yet, it is unclear whether they have a specific function in migration or elsewhere, and the precise molecular and mechanical mechanisms of ruffle formation remain poorly understood. Although membrane ruffles have been the showcase for many of the recent advances in volumetric light sheet microscopy, there are no tools for quantitative assessment of membrane ruffling^{78,81}. The thin, lamellar appearance make ruffles extremely challenging to segment in 3D live-cell images⁴⁶. Moreover, ruffles are transient and they exhibit significant heterogeneity in nature and distribution across the cell surface. These characteristics make ruffles difficult if not impossible to directly track in Cartesian 3D.

There are many unanswered questions about cell membrane ruffles. Here, we focus on defining a membrane ruffle by a set of objective criteria and then on measuring their speed. We acquired 3D volumes of SU.86.86 pancreatic ductal adenocarcinoma cells plated on fibronectin-coated cover glasses and co-expressing Tractin-mEmerald and myristoylated CyOFP1. Tractin is a marker for actin⁸², while myristoylated CyOFP1 served as a diffuse cell membrane marker. We acquired images every 2.27s for 30 timepoints, and used u-Unwrap3D to map the Cartesian 3D $S(x, y, z)$ surface of every timepoint into topographic 3D, $S(d, u, v)$ and into 2D, $S(u, v)$ for tracking (Fig. 5a, Suppl. Video 8). The cortical shape change was relatively small but ruffles travel on the surface. Like for bleb tracking we constructed a common static topographic coordinate space (d, u, v) for all time points. Here, we used the reference surface, $S_{\text{ref}}(x, y, z, t = 0)$ for this purpose (Extended Fig.5a). We then sought to track the spatial location of ruffles as individual 'ridge' objects. To do so, we projected $S(d, u, v)$ onto the 2D plane, i.e. the (u, v) coordinate was the same as setting $d = 0$, ($d = 0, u, v$) instead of applying topographic cMCF. We computed the local enrichment of the actin signal as the ratio of Tractin-mEmerald to CyOFP1 intensity. Kymograph visualization of $F_i(S(u, v, t))$ for mean curvature, H and Tractin-mEmerald/CyOFP1 (TC) showed strong co-fluctuation of curvature and local actin intensity. It also highlighted the transient, 'ripple-like' nature of ruffles and their merging and dissipation with a delay between successive ruffles of ≈ 20 s (Fig. 5b). To avoid complex image processing operations such as merging and splitting we applied optical flow-based region-of-interest (ROI) tracking^{83,84} to the TC intensity to track simultaneously the protrusive membrane ruffling and retrograde surface actin flow (Fig. 5c, left). The (u, v) image grid size was 1025 x 512 pixels (not 1024 x 512 as ruffles required active contour cMCF to be used to generate $S(d, u, v)$, see Methods) and the average dimensions of the tracked (u, v) ROI size was 23 x 23 pixels (approximately 0.06 x 0.11 μm pixel size in physical space). The resulting 2D ROI tracks exhibit unidirectional motion towards the cell center as shown by coloring directionality and remapping of (u, v) ROI tracks to polar (r, ϕ) (Fig. 5c, middle, Extended Fig. 5b) and Cartesian 3D (x, y, z) coordinates (Fig. 5c, right) (Suppl. Video 8). The optical flow tracks measure the geodesic cellular surface speed. To measure specifically the component corresponding to mean lateral ruffle travel speed we must project the 3D optical flow velocities along the same plane as the flat cell bottom. The volumetric imaging of cells is acquired on a cover glass tilted at $\approx 45^\circ$ (Extended Fig. 5c, left). Direct 3D plane-fitting to $S(x, y, z)$ to determine a precise angle is sensitive to outlier points and shapes deviating from an elongated ellipsoid. Thanks to the $S(u, v)$

480 representation of u-Unwrap3D mapping the curved proximal cell surface and the planar cell bottom to the
481 upper and lower half of the unwrapped 2D image respectively, we could readily annotate in 2D (u, v) the cell
482 bottom and fit a 3D plane to only this surface patch in (x, y, z) (Extended Fig. 5c, middle, right). Similarly, we
483 could gate ROI tracks in (u, v) and compute the lateral speed only for those associated the lamellipodia and
484 lamella surface. Doing so we found two populations in the speed histogram (Fig. 5d). Visualizing the speed
485 on $S(x, y, z)$, the faster population corresponds to higher curvature ruffles with speeds ranging from 2-10
486 $\mu\text{m}/\text{min}$, and an average speed of 4.2 $\mu\text{m}/\text{min}$ (Suppl. Video 8). This is at least two times faster than the
487 slower population surface retrograde actin flow ranging from 0-1 $\mu\text{m}/\text{min}$, which are consistent with the flow
488 speeds we used to measure by 2D fluorescent speckle microscopy in the lamella of epithelial cells⁸⁵. This
489 result suggests ruffles are actively produced and transported across the cell surface. To assess the
490 synchronicity of actin and ruffles we extracted distortion-corrected timeseries of TC and mean curvature, H
491 by sampling and averaging the respective values within a spatial window of 23 x 23 centered around the
492 (u, v) coordinates of all ROI tracks on the lamellipodia and lamella surface. Averaging the temporal cross-
493 correlation curves (mean \pm 95% confidence interval) of individual ROI tracks we find a significant positive
494 instantaneous (lag=0) correlation of 0.2 (Fig. 5e, left). Plotting the instantaneous (lag=0) correlation values
495 of individual ROI tracks as a function of the mean H value of the same ROI track and visualizing the
496 instantaneous correlation on $S(x, y, z)$, we found that ruffles with higher positive surface curvature are more
497 temporally correlated with TC intensity (Fig. 5e, middle, right). Altogether our results show that ruffles are
498 highly dynamic, transient protrusions that actively migrate on the cell surface and driven by locally enriched
499 filamentous actin. Our u-Unwrap3D framework provides now the platform for systematic investigation of the
500 mechanisms that drive and regulate these dynamics.

501

502 Discussion

503 Analyzing the spatiotemporal organization of molecular distributions and signaling activities on cell surfaces
504 in 3D has been limited by the lack of methods to represent, track and process these dynamics. Here we
505 introduce a surface-guided computing framework, referred to as u-Unwrap3D, to bijectively map a genus- X
506 Cartesian 3D surface to equivalent surface and volume representations that are optimally suited for a distinct
507 analytical task. The mappings rely on two critical insights: i) the engineered surface deformation of $S(x, y, z)$
508 to generate a genus-0 $S_{\text{ref}}(x, y, z)$ for which a 3D spherical parameterization exists; ii) a novel, efficient
509 algorithm to relax geometric distortion on the 3D sphere in a bijective and tunable manner. Insight i) is
510 fundamental to allowing $S_{\text{ref}}(x, y, z)$ to serve as a representative proxy that captures all the salient surface
511 features of the genus- X $S(x, y, z)$ surface and insight ii) to preserving this property when $S_{\text{ref}}(x, y, z)$ is
512 unwrapped to the 2D plane. Using diverse cell examples we validated that u-Unwrap3D could be widely
513 applied (>90% of cases) in a manner robust to the input surface mesh quality and that it accurately captures
514 the cell geometry to transfer salient surface features, morphological or molecular, between all representations.
515 We note that this 90% is an underestimation of the applicability. The validation dataset was assembled to be
516 deliberately heterogeneous and was not segmented with the downstream aim of surface mapping. In practice,
517 segmentation algorithms continue to improve and postprocessing techniques can be used to create improved
518 surface meshes. Moreover we can leverage surface meshing algorithms that are more sophisticated than
519 marching cubes, such as dual contouring⁸⁶ and shrink-wrapping⁸⁷, to guarantee watertight mesh creation.
520 For timelapse acquisitions, as we showed in Fig. 4,5, the situation is even simpler. Only one timepoint or
521 average surface is needed to generate a single common $S_{\text{ref}}(x, y, z)$ to unwrap all timepoints. u-Unwrap3D
522 puts in place a generic platform for the spatiotemporal processing of unconstrained cell geometries.

523 u-Unwrap3D is applicable for arbitrary genus- X 3D surfaces, $S(x, y, z)$ wherever a genus-0 reference surface,
524 $S_{\text{ref}}(x, y, z)$ can be found from conformalized curvature flow (cMCF). It works best when $S_{\text{ref}}(x, y, z)$ is close
525 to the $S(x, y, z)$. In our current implementation, the generation of $S_{\text{ref}}(x, y, z)$ may be suboptimal or fail when
526 either small handles in the mesh pinch together, causing early termination of the cMCF, or if the binary
527 voxelization and morphological hole closing fails to infill large handles and holes in the cMCF $S_{\text{ref}}(x, y, z)$.
528 Whilst we can increase the range of morphological hole closing in the latter case, we restrict dilation to a
529 maximum 3-5 voxels to minimise smoothing out protrusion features in $S_{\text{ref}}(x, y, z)$. Mesh surgery methods
530 have been developed in computer graphics to make non-watertight 3D meshes watertight^{88,89}, and fix
531 imperfections like holes and handles to reduce genus^{90,91} to generate higher quality 3D meshes. These have
532 yet to be applied and fully tested for complex cell surfaces. Future development will investigate how to apply
533 such procedures to allow u-Unwrap3D to be applied to input meshes of any quality. In our data we have paid
534 attention during the acquisition to generating sufficient foreground-to-background contrast for reliable surface
535 segmentation, thus minimizing mesh defects.

536 The concept of geometrical reduction of 3D into 2D geometry through the choice of an optimal coordinate
537 transformation has long existed in mathematics and physics to simplify mathematical manipulation and
538 plotting. For example, parametric coordinates describe the sphere, the cylinder, Mobius strip and helicoids
539 amongst others⁹². In computer graphics this is realised in the common practice of mapping between surfaces
540 through simpler intermediaries: for example, the texture mapping of arbitrary surfaces by optimal surface
541 cutting and mapping of the cuts into individual 2D shapes⁵⁷ and (u, v) surface parameterization by cutting
542 and gluing individually mapped 2D planar patches⁹³ or mapping to canonical shapes such as the triangle⁹⁴,
543 plane³⁹ or polyhedra⁹⁵ to minimize distortion. u-Unwrap3D draws inspiration from this thinking. Through the
544 availability and development of rationalized multiple 3D-to-2D representations, u-Unwrap3D projects
545 analyses that would otherwise require specialised mathematical operations into a sequence of simpler,
546 computationally tractable procedures for 3D mesh processing, image processing and machine learning with
547 specific consideration for single cell biology. Unlike computer graphics benchmarks, surface protrusions are
548 irregular, high curvature and dense. First, we specifically chose representations that map the whole cell
549 surface with well-behaved topologies such as the sphere and plane and designed a relaxation scheme to
550 guarantee interpolation between the minimal conformal and area distortion. This bypasses the numerical
551 instabilities of stitching multiple surface maps and only quasi-conformal mappings for the majority of literature
552 methods. Second, although $S_{\text{ref}}(x, y, z)$ was conceived as a mathematical trick to enable spherical
553 parameterization, because it is derived explicitly from $S(x, y, z)$ and not as a canonical shape, it serves
554 biologically to decompose $S(x, y, z)$ as the ‘sum’ of a smooth cell cortex and surface protrusions. Our results
555 suggest the introduced $S_{\text{ref}}(x, y, z)$ and $S_{\text{topo}}(x, y, z)$ could open up new opportunities to model and quantify
556 the interplay of dynamic membrane morphology and associated signals with more volumetric
557 nuclear/cytoplasmic signalling. Lastly, we designed mappings to underlying representations, including
558 Cartesian 3D, 3D sphere and 2D plane that are standard inputs in computer vision and machine learning.

559 With u-Unwrap3D standard computer vision, machine learning methods become directly applicable to
560 computing tasks on rugged complex surfaces. More recently, research into combining different geometric
561 representations are state-of-the-art in addressing complex computational problems such as multiple 2D
562 image views to inform 3D mesh reconstruction^{96,97}, or 3D mesh vertex coordinates with 2D unwrapped images
563 for feature extraction^{98,99}. u-Unwrap3D is fully complementary to these research developments - unifying the
564 different representations into a single surface-guided computing framework for downstream analysis. The u-
565 Unwrap3D framework is made available as a Python library. The resources and validation provided by this
566 work will aid the cell biology community to generate testable hypotheses of the spatiotemporal organization
567 and regulation of subcellular geometry and molecular activity.

568

569 **Acknowledgments**

570 We thank Hanieh Mazloom Farsibaf and Zach Marin for discussions on mesh processing. We also thank
571 Qiongjing Zou for putting the Python library into a continuous integration coding framework. Funding for this
572 work in the Danuser lab was provided by the grant R35 GM136428 (NIH). AW is a fellow of the Jane Coffin
573 Childs Memorial Fund. GMG is a Damon Runyon Fellow (DRG 2422-21).

574

575 **Author Contributions**

576 FYZ conceived and developed u-Unwrap3D and conducted the analyses. MD generated the uShape3D
577 protrusion instance segmentations and surfaces used in validation. AW acquired timelapse of the blebbing
578 MV3 cell. GMG, BJC and BC acquired timelapse of the ruffling SU.86.86 cell. FYZ and GD wrote the
579 manuscript with input from all authors. GD provided supervision and obtained funding.

580

581 **Competing Interests**

582 The authors declare no competing interests.

583

584 **Data Availability**

585 All data presented herein are available from the corresponding author upon request.

586

587 **Code Availability**

588 u-Unwrap3D is open source, developed as a Python library and is available at:
589 <https://github.com/DanuserLab/u-unwrap3D>.

590

591

592 **Methods**

593 u-Unwrap3D framework

594 Following we describe the algorithms underpinning each step of u-Unwrap3D depicted in Fig.1.

595 Step 1: $S(x, y, z)$ to $S_{\text{ref}}(x, y, z)$

596 *Conformalized mean curvature flow (cMCF)*. cMCF⁴⁹ modifies the mean curvature flow (MCF) to avoid the
 597 formation of pinches and collapsed vertices that compromise bijectivity and cause early flow termination for
 598 watertight meshes with high curvature features. We find cMCF also reduces the size of holes and handles in
 599 $S(x, y, z)$. MCF evolves Φ_t , the mesh at time t according to $\frac{\partial \Phi_t}{\partial t} = \Delta \Phi_t$, where Δ is the Laplace-Beltrami
 600 operator induced by the metric g_t and $\Phi_t(p) = \sum_{i=1}^N v_i(t) B_i(p)$ is the discrete mesh parameterization with N
 601 vertex positions $v_i(t) = \{v_1(t), \dots, v_N(t)\} \subset \mathbb{R}^3$, each $v_i(t)$ a 3D $(x_i(t), y_i(t), z_i(t))$ coordinate tuple and
 602 $\{B_1, \dots, B_N\}$ the local function basis, which for a triangle mesh is the linear hat basis spanned by the edge
 603 vectors. Galerkin's method¹⁰⁰ is used to find a weak, least-squares solution to the MCF equation within the
 604 span of $\{B_i\}$, by solving $\int_S \left(\frac{\partial \Phi_t}{\partial t} \cdot B_i \right) d\mu_t = \int_S (\Delta_t \Phi_t \cdot B_i) d\mu_t$, $\forall 1 \leq i \leq N$. S is the surface spanned by $\{B_i\}$
 605 and $d\mu_t$ the volume form. The equation is solved to obtain the vertex position, $v(t + \delta t)$ at the next iteration,
 606 $t + \delta t$ using backwards Euler integration; $\frac{\partial \Phi_t}{\partial t} \approx (\Phi_{t+\delta t} - \Phi_t) / \delta t$, $\Delta \Phi_t \approx \Delta \Phi_{t+\delta t}$ and noting the Laplace-
 607 Beltrami is the divergence of the gradient, $\Delta = \nabla \cdot \nabla$ with respect to the local mesh metric g_t to get
 608 $\int_S (\sum_{i=1}^N v_i(t + \delta t) B_i \cdot B_j - \sum_{i=1}^N v_i(t) B_i \cdot B_j) d\mu_t = \delta t \int_S \sum_{i=1}^N v_i(t + \delta t) g_t(\nabla_t B_i, \nabla_t B_j) d\mu_t$. The integrals, $M_{ij}^t =$
 609 $\int_S B_i \cdot B_j d\mu_t$ and $L_{ij}^t = \int_S g_t(\nabla_t B_i, \nabla_t B_j) d\mu_t$ are called the mass (\mathbf{M}_t) and Laplacian (\mathbf{L}_t) matrices at time, t .
 610 Substituting this notation and rearranging, the linear algebra MCF equation is

$$611 \quad \text{MCF} := (\mathbf{M}_t - \delta_t \mathbf{L}_t) v(t + \delta t) = \mathbf{M}_t v(t)$$

612 $v(t + \delta t)$ is then computed from $v(t)$ by direct matrix inversion. cMCF modifies the MCF equation above by
 613 using the Laplacian matrix at time $t = 0$, \mathbf{L}_0 for all timepoints. The Laplacian matrix is a measure of stiffness
 614 between local mesh faces, see active contour cMCF below. Using \mathbf{L}_0 for all timepoints instead of recomputing
 615 implicitly constrains mesh faces to retain the same aspect ratio and this conformalizes the flow.

$$616 \quad \text{cMCF} := (\mathbf{M}_t - \delta_t \mathbf{L}_0) v(t + \delta t) = \mathbf{M}_t v(t)$$

617 We use the *libigl* library¹⁰¹ with the cotangent Laplacian and barycentric mass matrix as the default
 618 implementations of \mathbf{M}_t , \mathbf{L}_t respectively. We improve the numerics of solving cMCF by normalization of the
 619 surface area and recentering of vertex coordinates at the origin after each iteration as recommended in Alec
 620 Jacobson's blog post (<https://www.alecjacobson.com/weblog/?tag=mean-curvature-flow>). u-Unwrap3D
 621 implements for optional usage the robust Laplacian of Sharp et al.¹⁰² instead of the cotangent Laplacian,
 622 which can improve numerical stability.

623

624 *Automatic stopping criterion for cMCF*. The ideal reference surface $S_{\text{ref}}(x, y, z)$ for topographic representation
 625 is the cortical cell shape without protrusions. We find that this corresponds to finding the 'elbow point' in the
 626 mean absolute Gaussian curvature (Fig. 1a) and not the convergence limit of cMCF which is the sphere⁴⁹.
 627 The difference in the mean absolute Gaussian curvature over vertices, $\Delta |K_t| = |K_t| - |K_{t-1}|$ between
 628 successive iterations $t - 1$ and t is used as an automatic stopping criterion for cMCF, $\text{stop}_t = \max(t_{\text{min}}, t_K)$.
 629 t_{min} is a user-specified minimum iteration number and t_K is the first iteration for which $\Delta |K_t|$ exceeds a user-
 630 specified threshold, $\Delta |K_t| > \Delta_{\text{thresh}}$. We compute the discrete Gaussian curvature, K_{v_i} at a vertex v_i , given
 631 by the vertex's angular deficit¹⁰³, $K_{v_i} = 2\pi - \sum_{j \in N(i)} \theta_{ij}$ where $N(i)$ are the triangles incident on v_i and θ_{ij} is
 632 the angle at vertex i in triangle j .

633

634 **Mesh voxelization and remeshing.** Mesh voxelization converts a surface mesh $S(x, y, z)$ to a binary volume
 635 image β where individual voxels are either 1 if they are interior to the surface or 0 if exterior. To do this we
 636 create a $X \times Y \times Z$ voxel volume image larger than the surface with voxels initialised to 0. We then set the
 637 intensities of all voxels indexed by the mesh (x, y, z) barycenters to 1, i.e. $B(x, y, z) = 1$. To ensure a closed
 638 binary volume with all interior voxel intensities = 1, $S(x, y, z)$ was iteratively subdivided by replacing each
 639 triangle face by four new faces formed from adding new vertices at the midpoint of every edge until the mean
 640 triangle edge length is < 1 voxel. We use the barycenter coordinates of the final mesh $S_{\text{final}}(x, y, z)$ to set the
 641 binary voxel values. In case of small holes in $S(x, y, z)$ that would prevent a closed binary volume by binary
 642 filling only, β was first dilated with a ball kernel, then binary infilled, and lastly binary eroded with a ball kernel.
 643 The postprocessed B was meshed using marching cubes¹⁰⁴ followed by construction of an approximated
 644 centroidal voronoi diagram (ACVD)¹⁰⁵ to produce a lower genus remeshing of $S(x, y, z)$ with approximately
 645 equilateral triangle faces. If the input $S(x, y, z)$ is a smooth shape with only small holes or handles such as
 646 the cMCF intermediary $S_{\text{ref}}(x, y, z)$ the proposed voxelization and remesh yields a genus-0 mesh.

647
 648 **Step 2: $S_{\text{ref}}(x, y, z)$ to $S_Q^2(x, y, z)$**

649 **Quasi-conformal spherical parametrization of genus-0 closed surfaces.** For genus-0 closed surfaces the
 650 uniformization theorem⁵² guarantees the existence of a conformal map onto the unit sphere, S^2 . For a closed
 651 orientable surface such as $S_{\text{ref}}(x, y, z)$ we can compute the genus, g from the Euler characteristic, $\chi = 2 -$
 652 $2g = \#V - \#E + \#F$. If $g = 0$ we applied the method of Choi et al.^{39,51} which uses the theory of quasi-
 653 conformal composition to ensure a bijective spherical parametrization with bounded conformal error (i.e.
 654 quasi-conformal). In practice, we found conformal errors = 0 (Extended Fig. 3).

655
 656 **Step 3: $S_Q^2(x, y, z)$ to $S_\Omega^2(x, y, z)$**

657 **Equiareal spherical parameterization by mesh relaxation.** We iteratively advect the vertex coordinates of
 658 $S_Q^2(x, y, z)$, whilst preserving face connectivity and the spherical shape to minimise the per face area distortion
 659 factor, λ . The magnitude and direction to advect each vertex, the vector field \vec{V} was found as the solution to
 660 the linear heat equation²⁷, $\frac{d\lambda}{dt} = -\Delta\lambda$, where Δ denotes the Laplacian. This is because an infinitesimal change
 661 in λ in the direction of \vec{V} is the Lie-derivative on 2-forms, $\mathcal{L}_{\vec{V}}\lambda = -\nabla \cdot (\lambda\vec{V})$ such that we can set $\Delta\lambda = -\nabla \cdot$
 662 $(\lambda\vec{V})$. As the Laplacian is the divergence of the gradient, $\Delta\lambda = \nabla \cdot (\nabla\lambda)$ we have $\vec{V} = -\frac{\nabla\lambda}{\lambda} = -\nabla\log\lambda$. To ensure
 663 vertices are displaced geodesically on the surface of a sphere according to \vec{V} , instead of unwrapping the
 664 sphere to the 2D (u, v) plane as in Lee et al²⁷, we developed a direct 3D advection scheme that displaces
 665 vertices in small constant step sizes ϵ using active contour cMCF (see below), and reprojecting to the sphere.
 666 λ and \vec{V} are recalculated for the new vertex positions and advection is repeated until an equiareal
 667 parameterization was achieved or the maximum number of iterations was reached. Details of our advection
 668 scheme is given algorithmically.

Input: Conformal spherical parameterization mesh, $S_Q^2(x, y, z)$ with vertices, v_{sphere} and faces, f_{sphere} , matching genus-0 mesh,
 $S_{\text{ref}}(x, y, z)$ with vertices, v_{ref} and faces, f_{ref} with identical number of vertices, $|v_{\text{sphere}}| = |v_{\text{ref}}|$, and faces, $f_{\text{sphere}} = f_{\text{ref}}$; vertex
 step size, ϵ ; total number of iterations, T ; mesh stiffness factor, δ (also known as the time step, δ in cMCF)

For iterations $t = 1, 2, \dots, T$... do :

$a_{\text{ref}}^{f_i} \leftarrow a_{\text{ref}}^{f_i} / \Sigma_i a_{\text{ref}}^{f_i}$	(normalised area per face f_i of S_{ref})
$a_{\text{sphere}}^{f_i}(t) \leftarrow a_{\text{sphere}}^{f_i}(t) / \Sigma_{f_i} a_{\text{sphere}}^{f_i}(t)$	(normalised area per face f_i of S_Q^2)
$\lambda^{f_i}(t) \leftarrow a_{\text{ref}}^{f_i} / a_{\text{sphere}}^{f_i}(t)$	(area distortion factor per face f_i of S_Q^2)
$\vec{V}^{f_i}(t) = -\nabla \log \lambda^{f_i}(t)$	(compute ∇ using the mesh grad operator ¹⁰⁶ , per face f_i)
$\vec{V}^{f_i}(t) \leftarrow \left(\frac{\vec{V}^{f_i}(t)}{\text{median}(\ \vec{V}^{f_i}(t)\)} \right) \vec{V}^{f_i}(t)$	(normalize the displacement vector with respect to the average triangle edge length, \bar{l})
$\lambda^{v_i}(t) \leftarrow \text{average}(\lambda^{f_i}(t))$,	(average the per face f_i vector field and area distortion
$\vec{V}^{v_i}(t) \leftarrow \text{average}(\vec{V}^{f_i}(t))$	factor onto vertices, v_i)

$\vec{V}_{tangent}^{v_i}(t) \leftarrow \vec{V}^{f_i}(t) - (\vec{V}^{f_i}(t) \cdot \vec{N}^{v_i}(t)) \vec{N}^{v_i}(t)$	(compute the surface tangential component of $\vec{V}^{v_i}(t)$ using per vertex normal, $\vec{N}^{v_i}(t)$)
$v_{sphere}(t+1) = (\mathbf{M}(t) - \delta_t \mathbf{L}(t))^{-1} \mathbf{M}(t) (v_{sphere}(t) + \epsilon \vec{V}_{tangent}^{v_i}(t))$	(perform active contour cMCF to advect v_{sphere} in direction of $\vec{V}_{tangent}^{v_i}(t)$ and compute the new v_{sphere})
$v_{sphere}(t+1) \leftarrow v_{sphere}(t+1) / \ v_{sphere}(t+1)\ $	(Ensure v_{sphere} lies on a sphere by centroid distance normalization)

This mesh relaxation bijectively diffuses the area distortion scalar factor on the sphere surface in a stable manner until a triangle face collapses, that is when an interior angle = 0. The extent of area relaxation is determined by the input mesh quality. We find that if $S_{ref}(x, y, z)$ is regular, with near-equilateral faces and has a minimal number of vertices ($> 40k$ for a pixel resolution of $0.104\mu\text{m}$), $S_{\Omega}^2(x, y, z)$ could be stably relaxed to an equiareal spherical parameterization, $S_{\Omega}^2(x, y, z)$, without triangle collapse.

Step 4: $S_{\Omega}^2(x, y, z)$ to $S(u, v)$

Automatic determination of unwrapping axis using weighted principal components analysis (PCA). Mapping surface features of interest with minimal geometrical distortion into $S(u, v)$ is equivalent to finding an optimal north-south unwrapping axis for $S_{\Omega}^2(x, y, z)$. This optimization is solved by weighted PCA. Let $v_i = (x_i, y_i, z_i)$ denote the coordinate of vertex i on $S_{\Omega}^2(x, y, z)$ and w_i the vertex weight, a score of the importance of mapping this vertex with minimum geometrical distortion. The 3×3 weighted covariance matrix, $\mathbf{A} = (\mathbf{w}^T \mathbf{v})(\mathbf{w}^T \mathbf{v})^T$ over all vertices captures the spread of the weight over the sphere. Eigendecomposition applied to the symmetric matrix \mathbf{A} finds the principal orthogonal directions of variance given by eigenvalues $\lambda = [\lambda_1, \lambda_2, \lambda_3]$, $\lambda_1 \geq \lambda_2 \geq \lambda_3$ and eigenvectors $\mathbf{e} = [\mathbf{e}_1, \mathbf{e}_2, \mathbf{e}_3]$. The eigenvalue captures the concentration of the weight w in the direction of the corresponding eigenvector. The optimal north-south unwrapping axis is the smallest eigenvector, \mathbf{e}_3 . To unwrap with respect to \mathbf{e}_3 we rotate the vertex coordinates v_i so that \mathbf{e}_3 is the new z-axis. As the eigenvector matrix \mathbf{e} is orthonormal and thus a 3D rotation matrix, \mathbf{e} is the rotation

matrix \mathbf{R} that maps the x-axis, $\begin{pmatrix} 1 \\ 0 \\ 0 \end{pmatrix} \mapsto \mathbf{e}_1$, y-axis, $\begin{pmatrix} 0 \\ 1 \\ 0 \end{pmatrix} \mapsto \mathbf{e}_2$, z-axis, $\begin{pmatrix} 0 \\ 0 \\ 1 \end{pmatrix} \mapsto \mathbf{e}_3$. For a 'pure' or proper rotation

matrix without reflection the determinant of \mathbf{R} must be $+1$, $\det(\mathbf{R}) = +1$. We derive a proper rotation, $\mathbf{R}' = [\mathbf{e}'_1, \mathbf{e}'_2, \mathbf{e}'_3]$ from \mathbf{R} by flipping the sign of $\mathbf{e}_1, \mathbf{e}_2$ to have positive x- and y- components respectively; $\mathbf{e}'_1 \leftarrow \text{sgn}(v_{1x})\mathbf{e}_1$, $\mathbf{e}'_2 \leftarrow \text{sgn}(v_{2y})\mathbf{e}_2$ (sgn is the sign function) and constructing $\mathbf{e}'_3 = \mathbf{e}'_1 \times \mathbf{e}'_2$ as the cross product of \mathbf{e}'_1 and \mathbf{e}'_2 . The matrix inverse of \mathbf{R}' (also the matrix transpose, \mathbf{R}'^T) is the desired rotation of $S_{\Omega}^2(x, y, z)$ such

that \mathbf{e}'_3 is the new z-axis. \mathbf{R}'^T maps the eigenvectors, $\mathbf{e}'_1 \mapsto \begin{pmatrix} 1 \\ 0 \\ 0 \end{pmatrix}$, $\mathbf{e}'_2 \mapsto \begin{pmatrix} 0 \\ 1 \\ 0 \end{pmatrix}$, $\mathbf{e}'_3 \mapsto \begin{pmatrix} 0 \\ 0 \\ 1 \end{pmatrix}$.

UV-mapping the unit sphere. We construct an equidistant UV unwrap of the unit sphere where u , the column coordinate equidistantly samples the circumference of the sphere, a total length 2π and v , the row coordinate equidistantly samples the arc from north to south pole, a total length π . This specifies a $N \times 2N$ pixel UV image with N as a user-defined size. By default $N = 256$ pixels. The UV mapping is constructed by pullback. Let $u = \theta$ be the azimuthal and $v = \varphi$ be the inclination angles of the sphere and setup the $N \times 2N$ grid of v vs u over the parameter space $[-\pi, 0] \times [-\pi, \pi]$. Convert the spherical coordinates, $(1, \theta, \varphi)$ to cartesian coordinates, $(x, y, z) = (\sin\theta \cos\varphi, \sin\theta \sin\varphi, \cos\theta)$. Each (x, y, z) coordinate is matched by nearest distance to a triangle face, ABC of $S_{\Omega}^2(x, y, z)$ to compute barycentric coordinates giving (x, y, z) as a convex combination of the vertices A, B, C ; $\mu_A A + \mu_B B + \mu_C C$, $\mu_A, \mu_B, \mu_C \geq 0$ and $\mu_A + \mu_B + \mu_C = 1$. By bijectivity of $S_{ref}(x, y, z)$ and $S_{\Omega}^2(x, y, z)$, we set A, B, C to the respective $S_{ref}(x, y, z)$ vertex coordinates to produce the respective uv- coordinate mapping, $(u, v) \leftrightarrow \mu_A A + \mu_B B + \mu_C C$. Note, setting A, B, C to be the vertex coordinates of any mesh bijective to $S_{\Omega}^2(x, y, z)$ e.g. $S(x, y, z)$ in the direct unwrapping case produces similarly the corresponding uv- coordinate mapping for that mesh. The weights μ_A, μ_B, μ_C is also used to map any other vertex associated quantities, $I_i(S_{\Omega}^2(x, y, z))$ such as curvature to $I_i(S(u, v))$, with vector-valued vertices A, B, C replaced now by scalar values. The construction of the UV map as described above replicates the first and last column of the resulting UV image. For applications such as texture mapping and active contour cMCF (see analysis of ruffles in Datasets section) where the UV image grid needs to be converted to a triangular mesh and the image boundaries 'stitched' together we instead use a $N \times 2N + 1$ pixel UV image.

713 Step 5: $V(x, y, z)$ to $V(d, u, v)$

714 *Topographic coordinate space (d, u, v) construction.* UV-unwrapping establishes bijection between a 2D uv
 715 plane and a 3D Cartesian surface, $(u, v) \leftrightarrow S_{\text{ref}}(x, y, z)$. We construct a topographic (d, u, v) coordinate
 716 space, $V(d, u, v)$ corresponding to a volume space normal to $S_{\text{ref}}(x, y, z)$ by propagating the (u, v)
 717 parameterized $S_{\text{ref}}(x, y, z)$ in Cartesian 3D at equidistant steps of α voxels, referred to as α -steps, along the
 718 steepest gradient of the signed distance function, $\nabla\Phi(x, y, z)$ for a total of D steps, $d \in -D_{\text{in}}, \dots, D_{\text{out}}$. $D =$
 719 $D_{\text{out}} + D_{\text{in}}$ is the total number of α -steps outwards and inwards relative to $S_{\text{ref}}(x, y, z)$ (which is $d = 0$)
 720 respectively. D_{out} is automatically determined to ensure $V(d, u, v)$ fully encapsulates $S(x, y, z)$. D_{in} is user-
 721 defined for computational efficiency or automatically determined as a fraction of the maximum internal
 722 distance transform. The signed distance function $\Phi(x, y, z)$ of $S_{\text{ref}}(x, y, z)$ is computed from the binary volume
 723 after voxelization. We voxelize the (u, v) parameterized $S_{\text{ref}}(x, y, z)$ directly using the same procedure as for
 724 meshes but employ image upscaling instead of mesh subdivision to ensure that the distance of 1 pixel in the
 725 (u, v) space is < 1 voxel in Cartesian (x, y, z) space. Using active contour cMCF (see below) to propagate
 726 the (u, v) parameterized $S_{\text{ref}}(x, y, z)$ for large D is slow; a 256x512 UV unwrap is 131,072 vertices. Moreover
 727 for a large D_{out} as the intra-spacing of 3D (x, y, z) positions increases, numerical instabilities arise that
 728 require implicit Laplacian smoothing¹⁰⁷ to suppress, which is also slow. Instead we use explicit Euler
 729 integration for propagation; $S_{\text{ref}}(x, y, z)_{d+\alpha} = S_{\text{ref}}(x, y, z)_d + \alpha \frac{\nabla\Phi_{S_{\text{ref}}(x, y, z)_d}}{|\nabla\Phi_{S_{\text{ref}}(x, y, z)_d}|}$ at α voxels from $S_{\text{ref}}(x, y, z)_d$ and
 730 $\frac{\nabla\Phi_{S_{\text{ref}}(x, y, z)_d}}{|\nabla\Phi_{S_{\text{ref}}(x, y, z)_d}|}$ is the unit gradient of $\Phi(x, y, z)$. Computationally efficient image-based filtering is then applied to
 731 smooth $S_{\text{ref}}(x, y, z)_{d+\alpha}$ per iteration to maintain bijectivity and suppress instabilities. Tilinear interpolation of
 732 the respective Cartesian volumetric signal intensities, $I_i(V(x, y, z))$ at the (x, y, z) coordinates indexed by
 733 $V(d, u, v)$ generates the topographic 3D equivalents, $I_i(V(d, u, v))$.

734
 735 Step 6: $I_i(V(d, u, v))$ to $S(d, u, v)$

736 *Topographic mesh $S(d, u, v)$ construction.* $S(x, y, z)$ was voxelized to a binary volume, $I_i(V(x, y, z))$ as above
 737 and transformed to $I_i(V(d, u, v))$. Marching cubes were applied at isovalue = 0.5 to create an initial $S(d, u, v)$
 738 which was remeshed with ACVD to construct the final low-genus $S(d, u, v)$ with near-equilateral triangle faces.
 739 The Cartesian 3D mesh, $S_{\text{topo}}(x, y, z)$ of $S(d, u, v)$ was constructed by interpolation of the (x, y, z) coordinates
 740 indexed by the corresponding (d, u, v) coordinates. To transform surface signals, $F_i(S(x, y, z))$ to
 741 $F_i(S(d, u, v))$, nearest neighbors was used to match $S(x, y, z)$ and $S_{\text{topo}}(x, y, z)$.

742 Mesh displacement by active contour cMCF

743 Active contours, or 'snakes'¹⁰⁸, define the boundary of an image region by minimizing its contour energy, E .
 744 The contour energy is the sum of an internal, E_{int} and an external energy, E_{image} , $E(v, I) = E_{\text{image}}(v, I) +$
 745 $E_{\text{int}}(v)$. The internal energy is set by $E_{\text{int}} = \int \alpha |v'|^2 + \beta |v''|^2 ds$, where the number of ' denotes the order of
 746 the spatial derivative. Here, the first term is the tension and α the elasticity of the contour. The second term
 747 is the stiffness and β the rigidity of the contour. The external energy is set by $E_{\text{image}} = -\int p ds$, where p is
 748 an attractor image for the contour. Minimizing E is equivalent to solving the Euler-Lagrange equation, $\alpha v'' -$
 749 $\beta v'''' = -\nabla p$ or in matrix form, $\mathbf{A}v + \nabla p = 0$, where \mathbf{A} prescribes the constant coefficients for computing the
 750 second and fourth order derivatives by finite differences. Given a vertex position $v(t)$, the next position, $v(t +$
 751 $1)$ is computed that minimises the residual error $\mathbf{A}v + \nabla p$ using gradient descent and backwards Euler is
 752 $v(t + 1) = v(t) - (\mathbf{A}_t v(t + 1) + \nabla p)$ and the linear system is $(\mathbf{I} + \mathbf{A}_t)v(t + 1) = v(t) + \nabla p$, where \mathbf{I} is the
 753 identity matrix. If $\beta = 0$, \mathbf{A}_t only comprises the second order coefficients associated with v'' , and we have
 754 $(\mathbf{I} + \alpha_t \mathbf{M}_t^{-1} \mathbf{L}_t)v(t + 1) = v(t) + \nabla p$ or equivalently, $(\mathbf{M}_t - \alpha_t \mathbf{L}_t)v(t + 1) = \mathbf{M}_t(v(t) + \nabla p)$ which is identical to
 755 the cMCF equation with \mathbf{M}_t the mass matrix, \mathbf{L}_t , the Laplacian matrix, $\alpha_t = \delta_t$ and $\mathbf{L}_t = \mathbf{L}_0$ in response to an
 756 external force, ∇p . This general equation can be solved by direct matrix inversion to move surface meshes
 757 diffeomorphically. We refer to this as *active contour cMCF* in this paper. To evolve mesh vertices, $v(t)$ normal
 758 to the surface in equal α -steps, we set $p = \Phi$, the signed distance function, and solve $(\mathbf{M}_t - \alpha_t \mathbf{L}_t)v(t + 1) =$
 759 $\mathbf{M}_t(v(t) + \alpha \nabla \Phi)$ iteratively, with $\nabla \Phi$ evaluated at $v(t)$ for each iteration. A positive α moves a cell surface
 760 mesh normally outwards from the cell and a negative α moves the mesh normally into the cell.

761 Quantification of geometric deformation errors for meshes

762 Surface mappings do not conserve local geometrical measures like angles, edge lengths and face area.
 763 Quantification of the distortion in these measures enables a task-specific optimization of the mapping and
 764 correction of statistical measurements made on the mapped surface. There are two primary geometric
 765 distortions to quantify; conformal and area distortion error (Extended Fig. 1). An isometric deformation is one
 766 with no error; both conformal and area distortion errors are 0.

769

770 **Conformal error.** The conformal or quasi-conformal error, Q_i measures the extent the shape of a mesh
 771 element i , e.g. a triangle face, is stretched. It is 0 if the relative distances between vertices and the angles
 772 between edges are preserved after the mapping. We compute Q of mapping triangle ΔABC to ΔDEF in 3D by
 773 first isometrically projecting all triangles into 2D. Let $A = (x_1, y_1, z_1)$, $B = (x_2, y_2, z_2)$, $C = (x_3, y_3, z_3)$ with
 774 edge vectors, $\overrightarrow{AB} = B - A$, $\overrightarrow{AC} = C - A$, then an identical 2D triangle $\Delta A'B'C'$ is given by $A' = (0,0)$, $B' =$
 775 $(|\overrightarrow{AB}|, 0)$, $C' = (\overrightarrow{AB} \cdot |\overrightarrow{AB} \times \overrightarrow{AC}|)$, $A', B', C' \in \mathbb{R}^2$. Let $\mathbf{X} = \begin{bmatrix} A' & B' & C' \\ 1 & 1 & 1 \end{bmatrix}$, be the 3x3 homogeneous vertex
 776 coordinates of $\Delta A'B'C'$ and $\mathbf{Y} = \begin{bmatrix} D' & E' & F' \\ 1 & 1 & 1 \end{bmatrix}$, the 3x3 homogeneous vertex coordinates of $\Delta D'E'F'$ then we
 777 solve for the 3x3 matrix, \mathbf{A} that maps \mathbf{X} to $\mathbf{Y} = \mathbf{A}\mathbf{X}$. \mathbf{A} is affine and of the form $\begin{bmatrix} \mathbf{J} & | & \mathbf{T} \\ \hline 0 & | & 1 \end{bmatrix}$ where \mathbf{J} is a 2x2
 778 transformation matrix and \mathbf{T} a translation matrix. Eigenvector decomposition of $[\mathbf{J}^T \mathbf{J}]$ gives 2 eigenvalues λ_1, λ_2 ,
 779 $\lambda_1 < \lambda_2$ and the singular values of \mathbf{J} , $\sigma_1 = \sqrt{\lambda_1}, \sigma_2 = \sqrt{\lambda_2}$. The ratio $\frac{\sigma_2}{\sigma_1}$ is the conformal error⁶². The global
 780 conformal error, Q of deforming a surface mesh S_1 to a mesh S_2 is the area weighted average of individual
 781 conformal errors Q_{f_i} of each triangle face f_i in S_1 ; $Q = \frac{\sum_{f_i \in S_1} a_{f_i} Q_{f_i}}{\sum_{f_i \in S_1} a_{f_i}}$ where a_{f_i} is the area of face f_i of S_1 .

782

783 **Area distortion error.** The area distortion error, λ measures the extent the surface area fraction of a mesh
 784 face is preserved during a surface mapping. One measure of λ is $\sigma_1 \sigma_2$, the product of the singular values of

785 \mathbf{J} and the area of the distortion ellipse⁶³. Here we use the surface area fraction ratio, $\lambda_{\Delta ABC} = \frac{\text{area}(\Delta ABC)}{\frac{\text{surface area of } S_1}{\text{area}(\Delta DEF)}} \frac{\text{area}(\Delta DEF)}{\text{surface area of } S_2}$

786 as a direct measurement of the area distortion in mapping ΔABC to ΔDEF in 3D. The global area distortion
 787 error, $\lambda = \frac{1}{|f_i|} \sum_{f_i \in M_1} \lambda_{f_i}$ for mapping a mesh S_1 to a mesh S_2 is the mean over all individual area distortion λ_{f_i}

788 of each triangle face f_i in S_1 , with $|f_i|$ the number of faces in S_1 and $\lambda_{f_i} = \frac{a_{f_i}^{S_1} / \sum_{f_i \in S_1} a_{f_i}^{S_1}}{a_{f_i}^{S_2} / \sum_{f_i \in S_2} a_{f_i}^{S_2}}$ is the area distortion of
 789 face f_i . The normalization of face area by total surface area is crucial to enable the computation of λ
 790 independent of scale.

791

792 Quantification of geometric deformation error for UV images

793 UV mapping defines a bijective relation between the 2D (u, v) rectilinear grid and a 3D surface, $S(u, v) \leftrightarrow$
 794 $S = S(x(u, v), y(u, v), z(u, v))$. Differentials can be used to compute geometric quantities when the (u, v)
 795 spacing is comparable to the (x, y, z) spacing. The differential area of a (u, v) pixel is $dA = \left| \frac{\partial S}{\partial u} \times \frac{\partial S}{\partial v} \right| du dv$,

796 where $\frac{\partial S}{\partial u} = \left(\frac{\partial S_x}{\partial u}, \frac{\partial S_y}{\partial u}, \frac{\partial S_z}{\partial u} \right)$ and $\frac{\partial S}{\partial v} = \left(\frac{\partial S_x}{\partial v}, \frac{\partial S_y}{\partial v}, \frac{\partial S_z}{\partial v} \right)$ are the image gradients of the x, y, z surface coordinates
 797 in u, v directions. The topographic space construction establishes bijection of the 3D (d, u, v) volumetric grid
 798 to a 3D volume, $V, (u, v, d) \leftrightarrow V = V(x(u, v, d), y(u, v, d), z(u, v, d))$. The differential volume of a (d, u, v) voxel
 799 is $dV = \left| \left(\frac{\partial V}{\partial u} \times \frac{\partial V}{\partial v} \right) \cdot \frac{\partial V}{\partial d} \right| du dv dd$. The matrix $\begin{bmatrix} \frac{\partial S}{\partial u} & \frac{\partial S}{\partial v} \end{bmatrix}$ is the 2x3 Jacobian matrix, \mathbf{J} and the conformal error per
 800 pixel is $\frac{\sigma_2}{\sigma_1}$, $\sigma_1 = \sqrt{\lambda_1}, \sigma_2 = \sqrt{\lambda_2}$ where $\lambda_1, \lambda_2, \lambda_1 < \lambda_2$ are the two eigenvalues of $[\mathbf{J}^T \mathbf{J}]$. The global conformal error

801 Q of uv -mapping the surface mesh S is the differential area weighted average of individual conformal errors
 802 Q_{uv} of each uv pixel; $Q = \frac{\sum_{uv} dA_{uv} Q_{uv}}{\sum_{uv} dA_{uv}}$ where dA_{uv} is the area element of the uv pixel. The area distortion error
 803 per uv pixel is the ratio between the surface area fraction of a uv pixel and the corresponding surface element

804 on S , $\lambda_{uv} = \frac{\frac{dudv}{\sum_{uv} dudv}}{\frac{dA_{uv}}{\sum_{uv} dA_{uv}}}$. Note $dudv = 1$ and $\sum_{uv} dudv = \text{total number of } uv \text{ pixels}$. The global area distortion error,

805 $\lambda = \frac{1}{|uv|} \sum_{uv} \lambda_{uv}$ for uv mapping a surface S is the mean over all individual area distortion λ_{uv} of each uv pixel.

806

807 Stopping criteria for area distortion relaxation of $S_Q^2(x, y, z)$

808 We used three additional stopping criteria to demonstrate intermediate area distortion relaxation between
 809 fully conformal, $S_Q^2(x, y, z)$ and fully equiareal, $S_\Omega^2(x, y, z)$ parameterization. We use the same nomenclature
 810 as for the above discussed geometric deformation error for meshes.

811

812 **Most isometric parametrization (MIPS) error.** The MIPS⁶² error is defined $\frac{\sigma_2}{\sigma_1} + \frac{\sigma_1}{\sigma_2}$ and is minimal when $\sigma_1 =$
 813 σ_2 . This error is trivially minimal for a conformal spherical parametrization $\left(\frac{\sigma_1}{\sigma_2} = 1 \right)$ (Extended Fig. 3b).

814

815 **Area-preserving MIPS.** The area-preserving MIPS⁶³ is defined $\left(\frac{\sigma_1}{\sigma_2} + \frac{\sigma_2}{\sigma_1}\right) \left(\sigma_1\sigma_2 + \frac{1}{\sigma_1\sigma_2}\right)^\theta$. We use this metric
 816 with $\theta = 1$, which measures the uniformity of stretch distortion over a surface. This error yields near-equiareal
 817 spherical parametrization (Extended Fig. 3b).
 818

819 **Isometric error.** We observed tradeoff of conformal error, \mathcal{Q} and log area distortion, $\log \lambda$ on a similar
 820 magnitude scale such that their summation has a unique global minima (Extended Fig. 1e). We thus define
 821 an isometric error metric, $(1 - \theta) \frac{\sigma_1}{\sigma_2} + (\theta) \log \lambda$ with a constant $\theta \in [0,1]$ to weight the relative importance of
 822 jointly minimizing conformal and area distortion error. We use $\theta = 0.5$ in Extended Fig. 3b.
 823

824 Assessment of geometrical difference between two meshes

825
 826 Four metrics were used to assess the difference between two meshes S_1 and S_2 possessing different number
 827 of vertices and faces; chamfer distance (CD), Wasserstein-1 distance (W_1), the difference in surface area
 828 (ΔA) and the difference in volume (ΔV). CD is the mean Euclidean distance between all vertices of S_1 when
 829 matched to the nearest vertex of S_2 and vice versa, $CD = \frac{1}{|S_1|} \sum_{x \in S_1} \min_{y \in S_2} \|x - y\|_2 + \frac{1}{|S_2|} \sum_{y \in S_2} \min_{x \in S_1} \|x - y\|_2$. The
 830 Wasserstein-1 distance (W_1) or Earth-mover's distance (EMD) is the minimum total area weighted distance
 831 of 1-to-1 matching vertices on S_1 and S_2 . W_1 accounts for the area of triangle faces and is minimal if the
 832 vertices of S_1 is a uniform sampling of S_2 or vice versa. Exact computation of W_1 is impractical, even for small
 833 meshes. We compute W_1 using the sliced-Wasserstein, SW_1 approximation, which uses random spherical
 834 projections to sum multiple 1D EMD distances⁶⁴. Specifically we use the
 835 `ot.sliced.max_sliced_wasserstein_distance` function from the Python `POT` library with 50 projections and
 836 average the result from 10 evaluations to report an estimate. The difference in total surface area is $\Delta A =$
 837 $A_{S_1} - A_{S_2}$ and is $\Delta A(\%) = \frac{A_{S_1} - A_{S_2}}{A_{S_2}}$ when given as a percentage. Total surface area was computed as the sum
 838 of individual triangle areas. The difference in total volume is $\Delta V = V_{S_1} - V_{S_2}$ and is $\Delta V(\%) = \frac{V_{S_1} - V_{S_2}}{V_{S_2}}$ when
 839 given as a percentage. The volume of a mesh was computed as the number of voxels in its binary voxelization
 840 computed as described above. We used the minimal possible dilation ball kernel size to ensure a correct
 841 volume computation - visual checking of binary voxelization and value at least 3x surface area. We use $S_1 =$
 842 $S_{\text{topo}}(x, y, z)$ and $S_2 = S(x, y, z)$ to compute the metrics of Extended Fig. 2,3.
 843

844 Reference surface inference for measurement of protrusion height

845 An optimal reference surface for protrusion segmentation must be a (u, v) parameterized surface i.e.
 846 $S_{\text{ref}}(d_{\text{ref}} = f(u, v), u, v)$ where $f(\cdot)$ is injective such that every surface point is defined by a unique (d, u, v) -
 847 tuple. We prove this by contradiction. Suppose a surface, $S(d, u, v)$ has points with the same (u, v) but
 848 different d coordinates. The points with higher d must therefore be part of a surface protrusion and thus
 849 $S(d, u, v)$ cannot be a $S_{\text{ref}}(d_{\text{ref}}, u, v)$. A suitable $S_{\text{ref}}(d_{\text{ref}}, u, v)$ can thus be found as the (u, v) parametrized
 850 2D 'baseline' surface, $d_{\text{ref}} = f_{\text{smooth}}(u, v)$ to a 2D adaptation of the asymmetric least squares problem
 851 (ALS)¹⁰⁹; $d_{\text{ref}} = \arg \min_z \left\{ \sum (w_{uv} (d_{uv}^{S'(d,u,v)} - d_{uv})^2 + \lambda \sum_{uv} (\Delta d_{uv})^2) \right\}$ with asymmetric weights, w_{uv} : $w_{uv} = p$ if
 852 $d_{uv}^{S'(d,u,v)} > d_{uv}$ and $w_{uv} = 1 - p$ otherwise. The regularization parameter, λ controls the contribution of the
 853 Laplacian $\Delta d_{uv} = \nabla^2 d_{uv}$. The solution is a surface intermediate between a (u, v) -parameterization
 854 approximation, $d_{uv}^{S'(d,u,v)} = f(u, v)$ of the topographic surface $S(d \approx f(u, v), u, v)$ and the flat 2D-plane ($d =$
 855 0) (Extended Fig. 3a). The input 1024x512 pixels approximation ($d_{uv}^{S'(d,u,v)}$) was computed as an image by
 856 extending a vertical ray upwards at each (u, v) pixel and setting the image pixel value as the longest
 857 contiguous stretch of the topographic binary. We downsample $d_{uv}^{S'(d,u,v)}$ 8x to 128x64 pixels for computational
 858 efficiency and additional smoothness regularization and solve for d_{ref} by running 10 iterations of ALS¹⁰⁹ using
 859 $p = 0.25$, $\lambda = 1$. The solution, d_{ref} is resized back to 1024x512 pixels. The height, h of $S(d, u, v)$ relative to
 860 the inferred reference surface is the difference, $h = d - d_{\text{ref}}$ between a vertex's d coordinate and d_{ref} of the
 861 matching point on $S_{\text{ref}}(d_{\text{ref}} = f_{\text{smooth}}(u, v), u, v)$ as found by interpolation.
 862

863 Topography guided binary segmentation of protrusions

864

865 For cMCF binary segmentation of $S(d, u, v)$, the reference surface used is the 2d (u, v) plane,
 866 $S_{\text{ref}}(d_{\text{ref}}, u, v) = S(d = 0, u, v)$ and the height is $h = d$. For more optimal segmentation, the reference surface,
 867 $S_{\text{ref}}(d_{\text{ref}}, u, v)$ was inferred as above and the height is $h = d - d_{\text{ref}}$, relative to the matching point on
 868 $S_{\text{ref}}(d_{\text{ref}}, u, v)$ with identical (u, v) coordinate. For both, the mean height, \bar{h} is the threshold to give the initial
 869 binary segmentation, $F_i(S(d, u, v)) = h \geq \bar{h}$. We postprocess by applying graph connected component
 870 analysis to remove small segmented regions with surface area < 200 voxels²; diffusing the result using two-
 871 class labelsreading¹¹⁰ with an affinity matrix, A , for 20 iterations, clamping ratio 0.99, and binarizing the label
 872 probability with threshold of 0.25 at the start of each iteration. Lastly, any remaining small regions with surface
 873 area < 500 voxels² was removed. The affinity matrix⁶⁹, A is a weighted sum ($\gamma = 0.9$) of an affinity matrix
 874 based on geodesic distance, A_{dist} and one based on surface convexity, A_{convex} ; $A = \gamma A_{\text{dist}} + (1 - \gamma) A_{\text{convex}}$
 875 of $S(d, u, v)$. $A_{\text{dist}} = \begin{cases} e^{-D_{\text{dist}}^2 / (2\mu(D_{\text{dist}})^2)} & i \neq j \\ 1 & i = j \end{cases}$ where D_{dist} is the pairwise Euclidean distance matrix between
 876 two vertices i and j . $A_{\text{convex}} = \begin{cases} e^{-D_{\text{convex}}^2 / (2\mu(D_{\text{convex}})^2)} & i \neq j \\ 1 & i = j \end{cases}$ where D_{convex} is the pairwise Cosine distance,
 877 $\frac{(1 - \cos(\theta_{ij}))}{2}$ matrix of the dihedral angle, θ_{ij} between the normal vectors at two vertices i and j . $\mu(D)$ denotes
 878 the mean value of the entries of matrix D .

879 Topography guided instance segmentation of protrusions

880 Individual protrusions are segmented by identifying high curvature protrusive features and applying
 881 connected components analysis. We compute the topographic mean curvature $H(S(d, u, v)) = -\frac{1}{2} \nabla \cdot \hat{n}$ with
 882 the normal, \hat{n} given by the unit gradient of the signed distance transform of the binary topographic volume of
 883 the cell, $I_{\text{binary}}(V(d, u, v))$. We compute a binary subvolume restricted to the surface, $I_{\text{surf}}(V(d, u, v))$, the
 884 intersection of the morphological dilation of $I_{\text{binary}}(V(d, u, v))$ with ball kernel size 2, and the morphological
 885 erosion of $I_{\text{binary}}(V(d, u, v))$ with ball kernel size 2. To identify high curvature surface regions, $H_{\text{high}}(d, u, v)$
 886 for lamellipodia, we concatenate $H(S(d, u, v))$ Gaussian smoothed with $\sigma = 1, 3, 5$ as a 3-dimensional feature
 887 for all voxels in $I_{\text{surf}}(V(d, u, v))$ and apply Gaussian mixture model (GMM) clustering (# classes = 3), keeping
 888 the class with the highest mean H . To identify $H_{\text{high}}(V(d, u, v))$ for blebs and filopodia which are circular and
 889 smaller, we use $H(S(d, u, v))$ Gaussian smoothed with $\sigma = 1$ as a 1-dimensional feature for all voxels in
 890 $I_{\text{surf}}(V(d, u, v))$ and apply kmeans clustering (# classes = 3), keeping the class with the highest mean H . For
 891 efficiency, both GMM and kmeans clusterers are fitted on a random sampling of 10,000 surface voxels. Small
 892 regions with < 500 connected voxels are removed. Connected component analysis labels each disconnected
 893 region in $H_{\text{high}}(V(d, u, v))$ as individual protrusions, $I_{\text{protrusions}}(V(d, u, v))$. We expand labels by 3 voxels
 894 and transfer the segmentation to the surface mesh, $S(d, u, v)$ by interpolation at the vertex coordinates,
 895 $F_{\text{protrusions}}(S(d, u, v))$ for further surface-based processing. We first apply the binary protrusion
 896 segmentation above, $B_{\text{protrusion}}(S(d, u, v))$ to $F_{\text{protrusions}}(S(d, u, v))$, taking the intersection and keeping
 897 segmentations with size > 100 voxel² Cartesian 3D surface area. We diffuse segmentation labels with
 898 labelsreading, clamping ratio 0.99 for 10 iterations, with affinity matrix A , $\gamma = 0.9$ as above. We do not
 899 rebinarize the label probability at the start of each iteration. Finally, we apply $B_{\text{protrusion}}(S(d, u, v))$ to the
 900 diffused segmentations to get the final instance segmentation labels, $F_{\text{protrusions}}(S(d, u, v))$.

901 Direct 2D unwrapping of protrusion submeshes

902 Segmented individual protrusions are open 3D surfaces with disk topology and can be directly unwrapped
 903 into 2D if they possess no holes or handles and have one boundary. The genus, g of an open orientable
 904 surface with b boundaries is computed from the Euler characteristic, $\chi = 2 - 2g - b = \#V - \#E + \#F$. Similar
 905 to the spherical parameterization of closed 3D surfaces, the open 3D surface is first mapped conformally to
 906 the unit disk then relaxed to get an equiareal disk parameterization.

907 Quasi-conformal disk parametrization of genus-0 open surfaces. We obtain a quasi-conformal map of an
 908 open 3D surface to the unit disk by harmonic parametrization¹¹¹. The boundary vertices are first mapped to
 909 the boundary of the unit circle, whilst preserving edge length fractions. Interior vertices are then mapped to
 910 the disk interior by solving Laplace's equation, $\nabla^2 \phi = 0$.

917 *Equiareal disk parameterization by mesh relaxation.* We relax the conformal disk parametrization whilst
918 preserving the boundary topology using the area-preserving flow method¹¹². We solve Poisson's equation to
919 compute the smooth vector field for diffusing the area distortion and explicit Euler integration to advect vertex
920 points iteratively with Delaunay triangle flips. The extent of area relaxation achieved is determined by the
921 mesh quality and number of vertices with respect to the extremity of local area distortion. In general, relaxation
922 was less stable compared to our relaxation for spherical surfaces above. For thin and long protrusions, prior
923 downsampling and uniform remeshing of the protrusion submesh was necessary to enable full area distortion
924 relaxation.

925
926 To convert a unit disk parameterization to an $N \times N$ pixel image, we 'square' the disk using the elliptical grid
927 mapping formula¹¹³, multiply the resulting vertex coordinates by $N/2$ and interpolate the coordinates and
928 associated vertex quantities onto a $N \times N$ pixel integer grid. This gives similar results to but is significantly
929 faster than solving the Beltrami equation⁹⁴.

931 Refinement of undersegmented blebs

932 Given $S(x, y, z)$ and the vertex ids corresponding to protrusion i , (v_i) we first impute any small holes in the
933 segmentation; inner vertices not assigned to protrusion i but should be in order to ensure the protrusion
934 submesh, $S_{\text{protrusion}}(x, y, z)$ is a genus-0 open surface. We do this by applying graph connected component
935 analysis on the submesh formed by all vertex ids not part of protrusion i , $\{v\} \setminus \{v\}^i$. Any component with
936 number of vertices $< 10\%$ the total surface area of $S(x, y, z)$ is assigned to protrusion i to form $\{v\}_{\text{impute}}^i$. The
937 submesh $S_{\text{protrusion}}(x, y, z)$ is formed from $\{v\}_{\text{impute}}^i$. We downsample $S_{\text{protrusion}}(x, y, z)$ by $1/4$ the number of
938 vertex points and remesh using ACVD as described above both for computational efficiency and to get a
939 higher quality mesh, $S_{\text{protrusion}}^{ds}(x, y, z)$ required for computing the intermediate equiareal disk
940 parameterization for a final square parameterization. $S_{\text{protrusion}}^{ds}(x, y, z)$ is directly unwrapped to a 2D 128 x
941 128 pixel square image as described above. Positive curvature 'seed' regions are identified by thresholding
942 the mean curvature mapped to 2D, $H(S_{\text{protrusion}}^{ds}(x, y, z)) > H_{\text{thresh}}$ with a global threshold and then applying
943 morphological closing, disk kernel radius 1 pixel. To classify regions as having negative, flat and positive
944 mean curvature, 3-class Otsu thresholding was applied to $H(S(x, y, z))$ to give two thresholds. All regions
945 with mean curvature greater than the higher threshold H_{thresh} were positive curvature. Undersegmented
946 blebs correspond to a binary composed of conjoined pseudo-circular regions. We use the gradient
947 watershed^{114,115} on the Euclidean distance transform of the high curvature region binary to automatically
948 separate conjoined blebs without seed markers. Mesh matching and interpolation was used to map H and
949 segmentation labels between $S_{\text{protrusion}}(x, y, z)$ and $S_{\text{protrusion}}^{ds}(x, y, z)$. The refined segmentation were
950 mapped as seed labels from $S_{\text{protrusion}}(x, y, z)$ for every protrusion back to $S(x, y, z)$. The revised seed labels
951 were then diffused across $S(x, y, z)$ using the combined geometrical and convexity affinity matrix from above
952 for 10 iterations with $\alpha = 0.99$. The binary protrusion segmentation from above is applied, and any
953 segmentation with Cartesian 3D surface area < 10 voxels² removed to give the final refined protrusion
954 segmentation instances.

956 Topography guided decomposition of cell surface

957
958 The instance protrusion segmentation $F_{\text{protrusions}}(S(d, u, v))$ above assigns a unique protrusion label ID to
959 each vertex of the surface mesh, $S(d, u, v)$. We use this surface-based $F_{\text{protrusions}}(S(d, u, v))$ as seed labels
960 to partition the total internal cell volume into the volume space unique to each protrusion i , $V_{\text{protrusion}}^i(d, u, v)$
961 and the reference cortical cell volume, $V_{\text{ref}}(d, u, v)$. This is done in three parts; the construction of $V_{\text{ref}}(d, u, v)$,
962 volume propagation of $F_{\text{protrusions}}(S(d, u, v))$, and using the previous two parts to volumize individual
963 protrusions to obtain $V_{\text{protrusion}}^i(d, u, v)$ (Extended Fig. 4e-g).

964
965 *Construction of reference surface by imputation.* The reference surface with segmented protrusions removed,
966 $S_{\text{ref}}(d, u, v)$ is of the functional form $S_{\text{ref}}(d = f(u, v), u, v)$ with $f(\cdot)$ injective and thus can be described by
967 $d_{\text{ref}} = d = f(u, v)$ only. This is a 2D image with d_{ref} as the pixel value. We impute the subset of pixels with
968 missing values corresponding to the removed surface protrusions from pixels with known d_{ref} using the fast
969 marching image inpainting¹¹⁶ implemented in the Python OpenCV library with an inpaint radius = 1 (Extended

970 Fig. 4e). The inpainted surface, $S_{\text{ref}}(d_{\text{ref}} = f_{\text{inpaint}}(u, v), u, v)$ is used to construct the binary reference cortical
 971 volume, $I_{\text{binary}}(V_{\text{ref}}(d, u, v))$ which is 1 for all voxels whose $d < d_{\text{ref}} = f_{\text{inpaint}}(u, v)$.

972
 973 *Volume propagation of surface-based instance protrusion segmentation.* The surface-based protrusion
 974 segmentation, $F_{\text{protrusions}}(S(d, u, v))$ is converted to voxel-based by setting the value of the voxels
 975 corresponding to the integer discretized $S(d, u, v)$ coordinates to the matching protrusion label ID. We expand
 976 the labels by 3 voxels using the Python Scikit-Image *skimage.segmentation.expand_labels* function and
 977 mask with the topographic binary cell volume $I_{\text{binary}}(V(d, u, v))$ to get the initial topographic volume
 978 protrusion segmentation, $I_{\text{protrusions}}(V(d, u, v))$ with only the surface of protrusions labelled. We apply
 979 marker watershed segmentation slice-by-slice to propagate labels laterally into the protrusion volume within
 980 a slice and labels from previous slices, from the top, $d = +D_{\text{out}}$ to the bottom, $d = -D_{\text{in}}$ of the topographic
 981 volume. At a slice $d = d_0$, we use the Euclidean distance transform of $I_{\text{binary}}(V(d = d_0, u, v))$ for watershed
 982 with the seed markers given by the labels of the previous slice, $d = d_0 + 1$ combined with the current labels
 983 of $I_{\text{protrusions}}(V(d = d_0, u, v))$ at slice $d = d_0$. In combining labels, the labels of the previous slice $d = d_0 + 1$
 984 takes precedence and overwrites the label of $I_{\text{protrusions}}(V(d = d_0, u, v))$. The result, $I_{\text{protrusions}}(V(d, u, v))$
 985 assigns a protrusion ID to all voxels in the entire cell volume $I_{\text{binary}}(V(d, u, v))$ (Extended Fig. 4f).

986
 987 *Volumization of individual protrusions.* The binary reference cortical volume, $I_{\text{binary}}(V_{\text{ref}}(d, u, v))$ is applied
 988 to exclude all cortical volume voxels in the watershed depth propagated $I_{\text{protrusions}}(V(d, u, v))$. We then apply
 989 connected component analysis to each unique protrusion label in $I_{\text{protrusions}}(V(d, u, v))$ and keep for each
 990 label, the largest contiguous volume region. The resulting $I_{\text{protrusions}}(V(d, u, v))$ is the final volume
 991 segmentation of all individual protrusions. For each unique protrusion, we generate a closed surface mesh
 992 by marching cubes. If the marching cubes mesh has > 1000 vertices, we downsample the mesh by a factor
 993 of 4 and remesh with ACVD. This last step is to keep the combined number of vertices across all protrusions
 994 and the reference surface reasonable for rendering and processing.

995 Direct Cartesian 3D decomposition of cell surface

996
 997 For each segmented protrusion i , we construct the Cartesian 3D submesh, $S_{\text{protrusion}}^i(x, y, z)$. We find the
 998 set of vertices on the open boundary, $\{v\}_{\text{boundary}}$ using the Python libigl library function, *igl.boundary_loop*,
 999 compute the mean of these points, $\bar{v}_{\text{boundary}}$ and form a submesh, $S_{\text{cap}}(x, y, z)$ with $\{v\}_{\text{boundary}}$ and
 000 $\bar{v}_{\text{boundary}}$. We upsample S_{cap} by successive mesh subdivision 3 times, each time replacing a triangle face by
 001 the four new faces formed by adding vertices at the midpoint of every edge, giving a mesh with $\approx 4^3 = 64$
 002 times more vertices. Finally we solve the Poisson problem⁷² to find the vertex coordinates of S_{cap}
 003 corresponding to the least bending energy. $S_{\text{protrusion}}^i(x, y, z)$ and $S_{\text{cap}}(x, y, z)$ are merged to form a closed
 004 surface mesh of protrusion i . Similarly $S_{\text{cap}}(x, y, z)$ is merged with the residual reference surface with
 005 segmented protrusions removed, $S_{\text{ref}}(x, y, z)$ to impute and close the hole left by protrusion i .

006 Conformalized mean curvature flow (cMCF) for flattening topographic surfaces, $S(d, u, v)$

007
 008 $S(d, u, v)$ are open surfaces. Application of cMCF⁴⁹, which is designed for closed surfaces, maps
 009 $S(d, u, v)$ onto the 2D plane as an elliptical disk and in the limit to a point. We want the flow to converge to
 010 the planar (u, v) rectangle. To do so, we impose additional no-flux constraints in the u -, v - directions on the
 011 boundary, ∂S but allow flow in the depth, d direction by adding to the right hand side of the cMCF equation
 012 an external force term that applies only in the u -, v - directions. In interior vertices, the flow follows the
 013 standard cMCF.

$$014 \quad cMCF_{\text{topo}} := \begin{cases} \left(\mathbf{M}_t^{\text{boundary}} - \delta \mathbf{L}_0^{\text{boundary}} \right) v(t + \delta t) = \mathbf{M}_t^{\text{boundary}} v(t) + \underbrace{\left[\mathbf{0}_d | \left(-\delta \mathbf{L}_0^{\text{boundary}} v(t) \right)_{uv} \right]}_{\text{to ensure no flux in } u, v \text{ direction}}, & \text{on } \partial S \\ \left(\mathbf{M}_t^{\text{mesh}} - \delta \mathbf{L}_0^{\text{mesh}} \right) v(t + \delta t) = \mathbf{M}_t^{\text{mesh}} v(t), & \text{on } S \setminus \partial S \end{cases}$$

015 where on the boundary, ∂S we use the mass, $\mathbf{M}_t^{\text{boundary}}$ and Laplacian, $\mathbf{L}_0^{\text{boundary}}$ matrix defined for a 2D line
 016 and $\mathbf{M}_t^{\text{mesh}}$, $\mathbf{L}_0^{\text{mesh}}$ is the mass and Laplacian matrices defined for a 3D triangle mesh. $[\mathbf{A}|\mathbf{B}]$ is used to denote
 017 the augmented matrix formed by appending the columns of matrix \mathbf{A} and \mathbf{B} . We solve for the vertex position
 018 at the next timepoint $v(t + \delta t)$ as with cMCF by direct matrix inversion.

019

020 Surface curvature measurement

021 The mean curvature, H of a 3D surface was measured as the divergence of \hat{n} , the unit surface normal¹⁰³,
022 $H = -\frac{1}{2}\nabla \cdot \hat{n}$. The surface mesh is voxelized to a binary volume, B and \hat{n} is computed as the gradient of the
023 signed distance transform of B with the Euclidean distance metric. H computed in this manner as opposed
024 to from the mesh directly using discrete differential geometry¹⁰³ or quadric plane fitting¹¹⁷ which is less
025 affected by the number of mesh vertices or the mesh quality.

026

027 Mesh quality measurement

028 The radius ratio = $2\frac{r_{in}}{r_{circ}}$, defined as twice the ratio between inradius and circumradius was used to measure
029 the face quality for a triangle mesh in Extended. Fig. 2,3. It is a mesh quality measure in the sense that the
030 radius ratio obtains its maximum value of 1 for an equilateral triangle; the shape which jointly maximizes all
031 internal angles and gives the best conditioning number for the mesh Laplacian matrix¹¹⁸.

032

033 Surface rendering

034 Triangle meshes were exported from Python using the Python Trimesh library into .obj mesh files and
035 visualized in MeshLab¹¹⁹. Volumetric images were rendered in Fiji ImageJ through the volume viewer plugin,
036 and intensities were contrast enhanced for inclusion in the figures using Microsoft PowerPoint. The local
037 surface maximum intensity projection image of Fig. 4c was produced by extending z-axis (depth) rays at
038 every xy pixel, and taking the maximum intensity of voxels within ± 9 voxels ($\pm 1\mu\text{m}$) of the cell surface.

039

040 **Datasets**

041 Cell morphology validation dataset

042 To validate u-Unwrap3D (Fig. 2,3 and Extended Fig. 2-4), we used 66 cell surfaces segmented and surface
043 protrusions classified using u-Shape3D and acquired from high resolution light sheet microscopy^{4,120} as
044 previously described⁴⁵. The surfaces include 19 MV3 melanoma cells expressing Lifeact-GFP showing blebs,
045 38 dendritic cells expressing Lifeact-GFP showing lamellipodia, and 9 human bronchial epithelial (HBEc)
046 cells expressing Tractin-GFP. We applied u-Unwrap 3D to these datasets with the following parameters for
047 each step: for Step 1, cMCF with maximum iterations = 50, $\delta_t = 5 \times 10^{-4}$, stopping threshold, $\Delta_{thresh} = 1 \times$
048 10^{-5} for blebs, $= 1 \times 10^{-5}$ for lamellipodia, $= 1 \times 10^{-4}$ for filopodia, $S_{ref}(x, y, z)$ mesh voxelization with
049 morphological dilation and erosion with ball kernel radius 5 voxels, Gaussian smoothing $\sigma = 1$ of binary
050 volume and initial $S_{ref}(x, y, z)$ meshing with marching cubes at isovalue 0.5, ACVD remeshing with number
051 of clusters = 90% the number of vertices in the marching cubes mesh; for Step 3, area distortion relaxation
052 with maximum iterations = 100, $\delta_t = 0.1$, stepsize $\varepsilon = 1$ and if equiareal was not achieved, repeat relaxation
053 with a slower $\delta = 5 \times 10^{-3}$; for Step 4, the mean curvature of $S_{ref}(x, y, z)$ was used as the weight for
054 determining the unwrapping axis, and a 1024×512 pixel (u, v) grid; for Step 5, an upsampling factor of 3 for
055 binary voxelization, $\alpha = 0.5$ voxel steps, a specified $D_{in} = 40$ steps and 2D robust smoothing¹²¹ with
056 smoothing factor = 50 for each iteration; for Step 6, binarization of the topographic 3D mapped binary cell
057 segmentation with a threshold of 0.5, then Gaussian smoothing $\sigma = 1$ and initial marching cubes meshing at
058 isovalue 0.5, ACVD remeshing with number of clusters = 50% the number of vertices in the marching cubes
059 mesh.

060

061 3D timelapse lightsheet imaging and analysis of blebs

062

063 *Cell culture and timelapse imaging.* All details of the cell line creation, culture and imaging of the MV3 GFP-
064 expressing melanoma cell movie in Fig. 4 were previously published³⁸. The movie is a total of 200 frames
065 acquired at a frequency of 1.21 s per frame. Each frame is a $104 \times 512 \times 512$ size 3D volume with a voxel
066 resolution of $0.300 \times 0.104 \times 0.104 \mu\text{m}$.

067

068

069

070

071

072

073

074

075

076

077

078

079

080

081

082

083

084

085

086

087

088

089

090

091

092

093

094

095

096

097

098

099

100

101

102

103

104

105

106

107

108

109

110

111

112

113

114

115

116

117

118

119

120

121

122

123

124

125

Cell segmentation and surface meshing. The 200 timepoints were spatiotemporally registered volumetrically to the first timepoint, $t = 0$ as previously described³⁸. The cell surface at $t = 0$ was segmented using a multi-level method¹²² involving local contrast enhancement, deconvolution and edge enhancement and surface meshed as described above to obtain $S^{t=0}(x, y, z)$. Images were deconvolved using the Wiener-Hunt deconvolution approach¹²³ with our previously published point-spread function⁴⁵. The surface mesh at all subsequent timepoints, $S^t(x, y, z)$ were reconstructed using the non-rigid registration deformation field from volumetric registration³⁸. The vertex Septin intensity was calculated by extending from the surface a trajectory to an absolute depth of 1 μm along the steepest gradient of the distance transform to the mesh surface, and assigning the 95th percentile of intensity sampled along that trajectory to the originating vertex to capture the systematically brightest accumulation of Septin signal in the cortical shell. The raw Septin intensity suffers decay from bleaching. We simultaneously normalized and corrected the vertex Septin intensity by computing a normalized Septin intensity as the raw intensity divided by the mean Septin intensity in the whole cell volume at each timepoint.

u-Unwrap3D analysis. We computed a mean surface mesh, $\bar{S}(x, y, z)$ from all $S^t(x, y, z)$ as the input surface to u-Unwrap3D. This was done by surface meshing the mean binary volume over all binary voxelizations of individual $S^t(x, y, z)$ at an isovalue of 0.5. u-Unwrap3D was applied to $\bar{S}(x, y, z)$ to create a common static (d, u, v) coordinate space that all $S^t(x, y, z)$ is mapped to in Step 5 of u-Unwrap3D to generate $S^t(d, u, v)$. u-Unwrap3D was run with the same parameters for all steps as for blebs in the validation dataset, except for the following modifications: step 1, the same automatic stopping iteration number but +5 steps, and ACVD with 10% of the marching cubes mesh to get a smoother $S_{\text{ref}}(x, y, z)$; step 4, a smaller 512 x 256 pixel size (u, v) grid and not using the unwrapping axis inferred by curvature-weighted PCA - this axis passed through a large bleb and affected tracking; step 5, $D_{\text{in}} = 96$ steps - a total of 5 μm . Topographic cMCF with the robust mesh Laplacian¹⁰², mollify factor = 1×10^{-5} , $\delta_t = 5 \times 10^4$ was applied to each $S^t(d, u, v)$ for 10 iterations to compute the corresponding $S^t(u, v)$.

Bleb segmentation and tracking. Blebs were segmented from $S(d, u, v)$ at every timepoint using the instance segmentation algorithm with refinement for undersegmented blebs as described above. In computing the binary protrusion segmentation we use a downsampling factor of 4 due to the smaller 512 x 256 pixel (u, v) grid and diffuse the segmentation for 5 iterations as the blebs were smaller than the validation dataset. The segmented 512 x 256 (u, v) bleb images, $F_{\text{bleb}}(S(u, v))$ were padded 50 pixels on all four sides respecting spherical topology. This is done by periodic padding along the u - axis. For the v - axis, we pad the top of the image by reflecting the pixels with respect to the first image row (i.e. all pixels in row 2 to row 51) and then flipping in the u - axis. Similarly, the bottom is padded by reflecting the pixels with respect to the last image row (i.e. all pixels in row 2 to row 511) and then flipping in the u - axis. For each unique bleb in every timepoint, we computed the bounding box of the bleb given by top left, $(u_{\text{min}}, v_{\text{min}})$ and bottom right $(u_{\text{max}}, v_{\text{max}})$ coordinates. The bleb bounding boxes were tracked using an optical flow assisted bounding box tracker⁷⁷. Boxes were linked over time into tracks using bipartite matching and the intersection over union (IoU>0.25 for valid match) of bounding boxes as the distance function between pairs. To handle large changes in box size, the matching between the current and next frame was carried out on the predicted bounding box coordinates by local optical flow¹²⁴. Optical flow was computed using the mean curvature, $H(S(u, v))$ after rescaling $H(S(u, v))$ to be an 8-bit grayscale image using the global minimum and maximum curvature values over time. In case of temporary occlusion or missed segmentation, any non-matched blebs were propagated for up to 5 frames (6s) using the estimated optical flow before track termination. Tracks with > 5 frames (6s) and a mean positive curvature, $H > 0.1 \mu\text{m}^{-1}$ were retained as bleb tracks. The coordinates of retained tracks was corrected to account for the initial padding of 50 pixels. To remove erroneous and duplicated tracks, we uniquely match every segmented bleb in each timepoint to a track by IoU. For each track, we then computed the fraction of its lifetime that could be matched to a bleb and removed all tracks for which this proportion was < 50%. Lastly for each track we checked for sudden changes in the bounding box area, which was indicative of an erroneous bounding box in need of substitution by an inferred corrected bounding box. We applied this procedure to each track in order to construct the timeseries of the bounding box area over the track lifetime and compute a smooth reference timeseries using the central moving average with a window of 3 frames. The bounding box at a timepoint is erroneous if the instantaneous difference between the raw and smooth bounding box area > 500 pixel² (the mean (u, v) bleb box area is 361 pixel²). The coordinates of a corrected bounding box is inferred from non-erroneous bounding boxes by interpolation using a linear spline. The tracks that remained fully in-focus over its lifetime were retained for analysis.

Bleb timeseries extraction.

We detected (u, v) pixels on blebs by labelling spatially contiguous areas of positive mean curvature based on 3-class Otsu thresholding defining positive, flat or negative curvature. The largest connected component within a bleb bounding box was defined as on-bleb and the remainder area within the bounding box as off-bleb. We extracted distortion-corrected average timeseries of bleb area, mean curvature and septin intensity, that is of a scalar quantity, F by observing that the mean of F over a Cartesian 3D surface area is equivalent to computing a weighted mean over the equivalent (u, v) area, $\frac{\iint_S F(S(x,y,z)) dS}{\iint_S dS} = \frac{\iint_S F(S(u,v)) dA dudv}{\iint_S dA dudv}$. The weight, dA is the magnitude of the differential area element, $dA = \left| \frac{\partial S}{\partial u} \times \frac{\partial S}{\partial v} \right|$ described above.

Bleb event alignment.

Individual blebbing events were detected within a track by applying peak finding after central moving averaging of bleb area timeseries with a window of 3 timepoints. A peak was defined as having a prominence > 0.5 and separated from a neighboring peak by at least 3 timepoints. Individual bleb event timeseries were constructed and temporally aligned using the detected timepoint of maximal bleb area as timepoint 0 and taking a window of 14 timepoints on either side (a total 29 timepoints, 35 s).

3D timelapse lightsheet imaging and analysis of ruffles

Cell culture and timelapse lightsheet imaging. SU.86.86 cells were purchased from American Type Culture Collection (CRL-1837). The cells were transfected with integrating lentiviral plasmids carrying genes for myristoylated CyOFP1 and Tractin-mEmerald. The cells were cultured in RPMI medium supplemented with 10% fetal bovine serum and 1% anti-anti (Gibco 15240062), at 37°C in a humidified incubator and 5% CO₂. SU.86.86 cells were imaged on fibronectin-coated coverslips on a custom axially swept light sheet microscope¹²⁵. The microscope detection system comprises a 25X NA1.1 water immersion objective (Nikon, CFI75 Apo, MRD77220) and a 500mm tube lens. The illumination was done through a 28.6X NA0.66 water immersion objective (Special Optics, 54-10-7). The movie analysed in Fig.5 is a total of 30 frames acquired at a frequency of 2.27 s per frame. Each frame is a two-channel 151 x 1024 x 1024 size 3D volume with a voxel resolution of 0.300 x 0.104 x 0.104 μm .

Cell segmentation and surface meshing. All timepoints were rigid registered volumetrically to the first timepoint, $t = 0$ to compensate for drift. The CyOFP1 image was also rigid registered to the Tractin-mEmerald in each timepoint. For every timepoint, the volumetric image was segmented using a multi-level method¹²² involving local contrast enhancement, deconvolution and edge enhancement and surface meshed as described above to obtain the surface mesh, $S(x, y, z)$. The vertex Tractin-mEmerald and CyOFP1 intensities were calculated by extending a trajectory to an absolute depth of 1 μm along the steepest gradient of the distance transform to the mesh surface, and taking the mean intensity along the trajectory.

u-Unwrap3D analysis. The first timepoint surface mesh was used as the input $S(x, y, z)$ to u-Unwrap3D to create a common static (d, u, v) coordinate space that the surface meshes from all timepoints is mapped to in Step 5 of u-Unwrap3D to generate $S^t(d, u, v)$. We use Unwrap-3D with the following parameters for each step: Step 1, cMCF with maximum iterations = 50, $\delta_t = 1 \times 10^{-5}$, automatic stopping threshold, $\Delta_{thresh} = 5 \times 10^{-5}$, $S_{ref}(x, y, z)$ mesh voxelization with morphological dilation and erosion with ball kernel radius 5 voxels, Gaussian smoothing $\sigma = 1$ of the binary volume and initial marching cubes meshing at isovalue 0.5, ACVD remeshing with number of clusters = 10% the number of vertices in the marchin cubes mesh, and further volume constrained Laplacian mesh smoothing¹²⁶ with implicit time integration, time step 0.5 for 15 iterations; for Step 3 area distortion relaxation with maximum iterations = 100, $\delta_t = 0.1$, stepsize $\varepsilon = 1$; for Step 4 we use the binary positive curvature region of $S_{ref}(x, y, z)$ given by 3-class Otsu thresholding as the weight for determining the unwrapping axis, and use a 1025 x 512 pixel (u, v) grid; for Step 5, for outwards propagation, an upsampling factor of 3 for binary voxelization, $\alpha = \text{minimum of } 0.5 \text{ and } \frac{1}{2}(\Delta u + \Delta v)$ voxel -steps where $\Delta u, \Delta v$ is the mean Cartesian 3D distance of traversing one pixel in u, v directions and a separable 1D uniform box filter smoother with a window 5 pixels; for inwards propagation, we use active contour cMCF with $\delta_t = 5 \times 10^{-4}$, and robust mesh Laplacian¹⁰², mollify factor 1×10^{-5} for better numerical stability with the (u, v) parameterized $S_{ref}(x, y, z)$ converted into a triangle mesh by triangulating the quadrilateral pixel connectivity and inserting additional triangles to 'stitch' the image boundaries into a spherical topology, (note the latter stitching requires an even number of columns after discounting that the last column is the same as

180 the first column, hence a 1025 x 512 grid) and $D_{in} = (\text{maximum internal distance transform value}) / \alpha$ steps;
181 for Step 6, marching cubes meshing of the topographic 3D mapped binary cell segmentation at isovalue 0.5
182 following Gaussian smoothing $\sigma = 1$, ACVD remesh with number of clusters = 50% the number of vertices in
183 the marching cubes mesh and retaining the largest connected component mesh. Topographic cMCF with
184 robust mesh Laplacian¹⁰², mollify factor = 1×10^{-5} , $\delta = 5 \times 10^4$ was applied to each $S(d, u, v)$ for 10
185 iterations to compute the corresponding $S(u, v)$.
186

187 *Optical flow ROI tracking.* We used motion sensing superpixels (MOSES)^{83,84} in dense tracking mode which
188 automatically monitors the spatial coverage of ROIs and introduces new ROIs dynamically to ensure uniform
189 spatial tracking at every timepoint. We partitioned the image with an initial user-specified 1000 non-
190 overlapping rectangular regions-of-interest (ROI). Each ROI was tracked over time by subsequently updating
191 its centroid by the median optical flow¹²⁴ within the ROI. Optical flow was computed from the Traction/CyOFP1
192 (TC) signal after rescaling $TC(S(u, v))$ to be an 8-bit grayscale image using the video minimum and maximum
193 TC values.

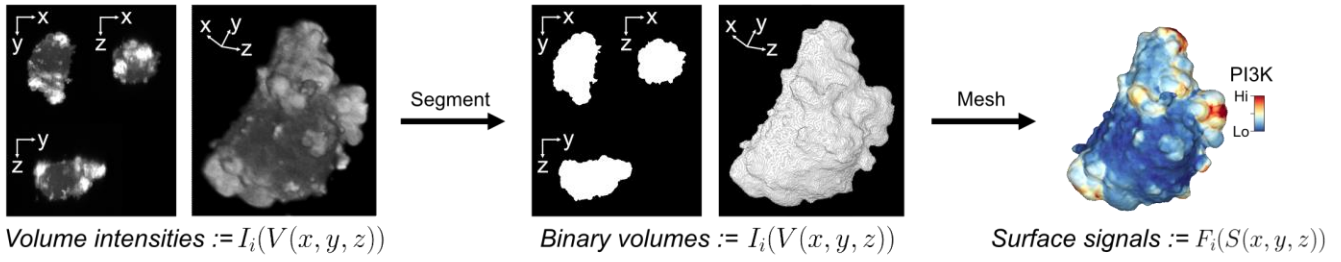
194 *ROI timeseries extraction and cross-correlation.* Distortion-corrected average timeseries of mean
195 Traction/CyOFP1 (TC) and H were computed for a track using the same weighted mean as for blebs. A square
196 bounding box of the mean MOSES ROI width centered at the track (u, v) coordinate was used to sample the
197 scalar values at each timepoint. The distortion-corrected timeseries can be treated as standard 1D timeseries.
198 The 1D normalized cross-correlation was thus computed between the distortion-corrected TC and H
199 timeseries for individual tracks without modification. ROI cross-correlation curves were averaged at all time-
200 lags to derive the mean and 95% confidence interval ROI cross-correlation curve. A deviation of the curve
201 greater than the 95% confidence interval at a time lag of 0 indicated significant instantaneous correlation.
202

203
204 *Retrograde actin flow and mean ruffle travel speed.* Computing the speed histogram with 25 bins and speed
205 range 0-10 $\mu\text{m}/\text{min}$ showed a slow and fast population (Fig. 5d). We inferred the mean speed of the two
206 populations as the two thresholds generated by 3-class Otsu thresholding. The lower and faster of the
207 thresholds are the mean speed of retrograde actin flow and ruffles respectively.

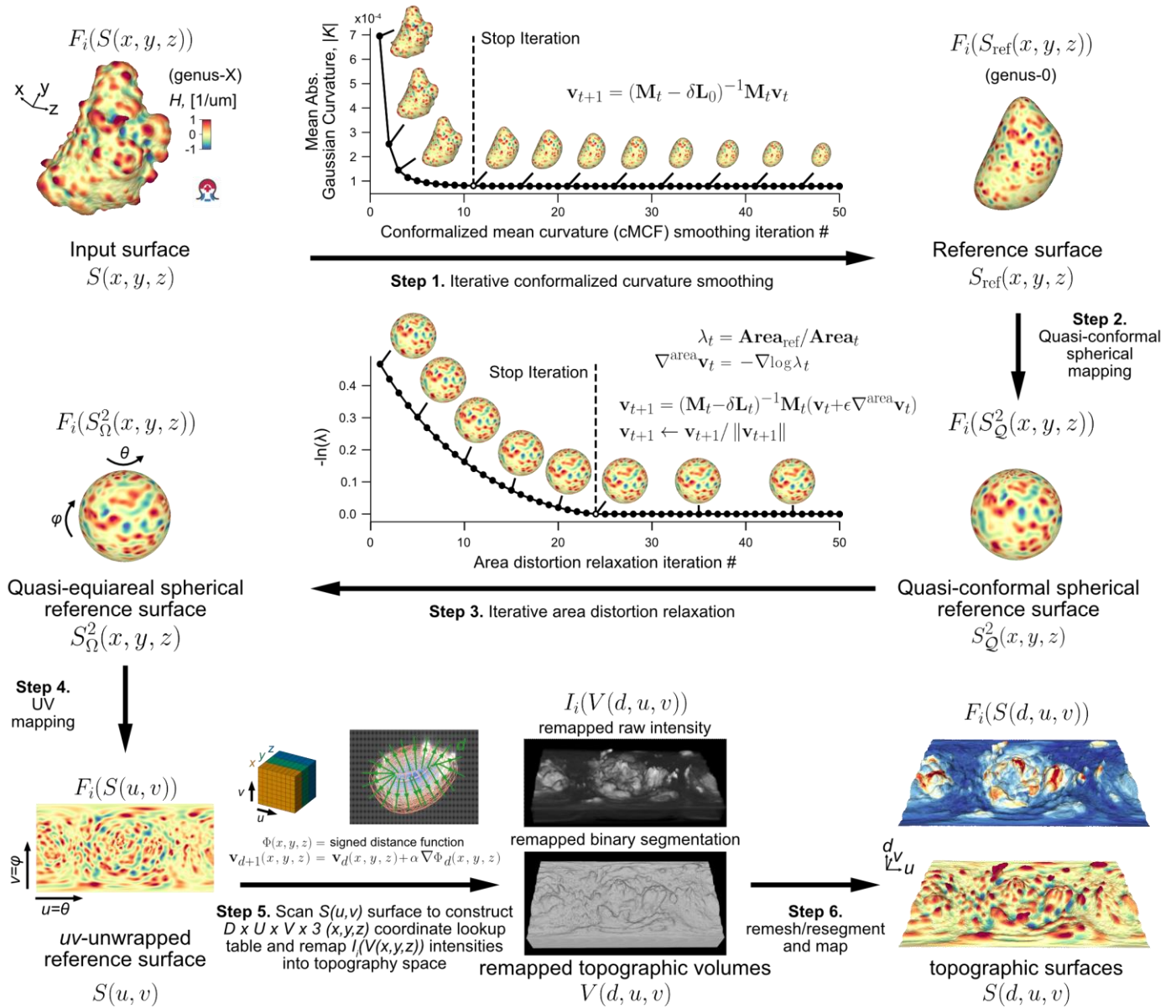
208
209 *Cross-correlation and curvature relationship.* We computed the continuous relationship of mean curvature,
210 H and the lag 0 cross-correlation of TC and H (Fig. 5e) over ROI tracks using kernel density. Gaussian kernel
211 density with a bandwidth set by Scott's rule was used to derive the joint density distribution of H and cross-
212 correlation i.e. $p(X, Y)$, with $X: H$, Y : cross-correlation over the closed intervals $X \in [-0.2, 0.6]$ and $Y \in$
213 $[-1, 1]$. The continuous relationship is then given by the marginal expectation with capital denoting the
214 random variable and $\mathbb{E}[\cdot]$ the expectation operator, $\mathbb{E}[Y|X = x] = \int Y p(Y|X = x) dY = \int Y \frac{p(X, Y)}{p(X)} dY =$
215 $\frac{\int Y p(X, Y) dY}{\int p(X, Y) dY}$ with standard deviation equivalently defined as the square root of the variance,
216 $\mathbb{E}[(Y - \bar{Y})^2|X = x] = \mathbb{E}[Y^2|X = x] - \mathbb{E}[Y|X = x]^2$. The evaluation of the integrals uses 100 bins for both H and
217 cross-correlation.
218

a Overview of u-Unwrap3D

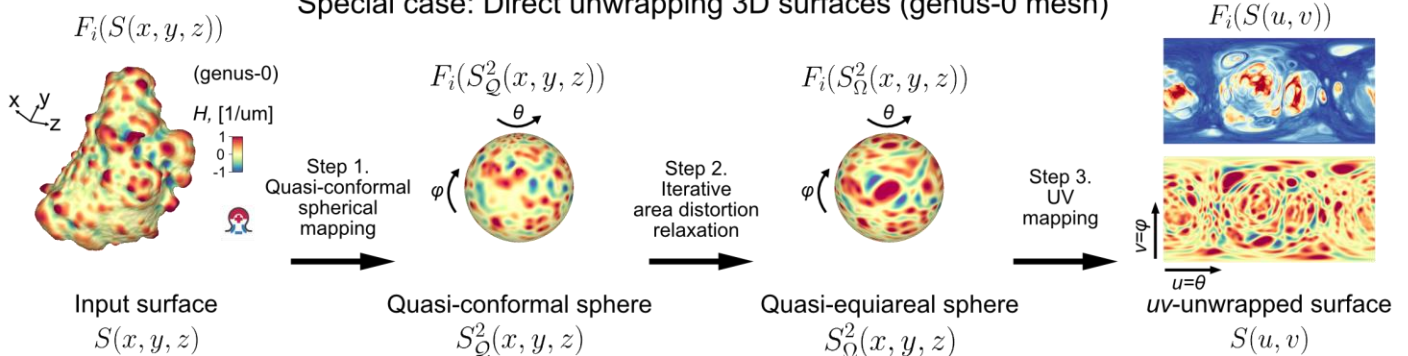
u-Unwrap3D operates on surface meshes



Key algorithmic steps



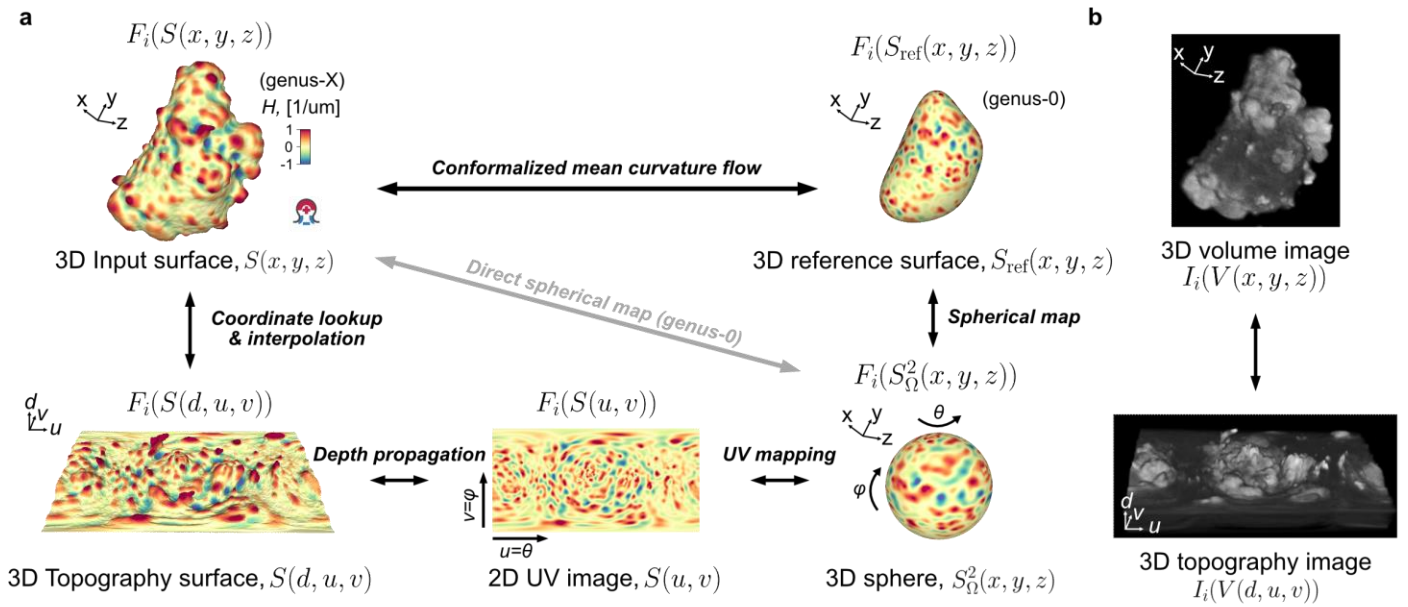
b Special case: Direct unwrapping 3D surfaces (genus-0 mesh)



220 **Figure 1. Overview of the surface-guided computing framework u-Unwrap3D.** a) Overview of the 6 key
221 steps to map an input genus-X Cartesian 3D surface, $S(x, y, z)$ such as that obtained from surface meshing
222 the binary segmentation of an input 3D volume image, I_i , and associated scalar measurements, $F_i(S(x, y, z))$,
223 via a smooth genus-0 reference surface, $S_{\text{ref}}(x, y, z)$, into any of three additional representations; topographic
224 3D surface, $S(d, u, v)$, 3D sphere, $S^2(x, y, z)$ and 2D plane, $S(u, v)$. \mathbf{v} denotes mesh vertex coordinates, \mathbf{M} is
225 the mesh mass matrix, \mathbf{L} is the mesh Laplacian matrix, ϵ the step size of area-distortion relaxation, α the step
226 size (in pixels) of the propagation distance, d the topographic depth (in pixels) and t the iteration number. c)
227 Steps to directly remap input genus-0 surfaces without need for a reference surface. In the figure, $S(\cdot), V(\cdot)$
228 denote surface and volume geometries, respectively, in either Cartesian 3D, topographic 3D, or radius-
229 standardized 3D spherical coordinates; $F_i(S(\cdot))$ and $I_i(V(\cdot))$ denote surface or volumetric signals as a
230 function of a particular surface or volume geometry. H and K denote mean and Gaussian curvatures
231 respectively.

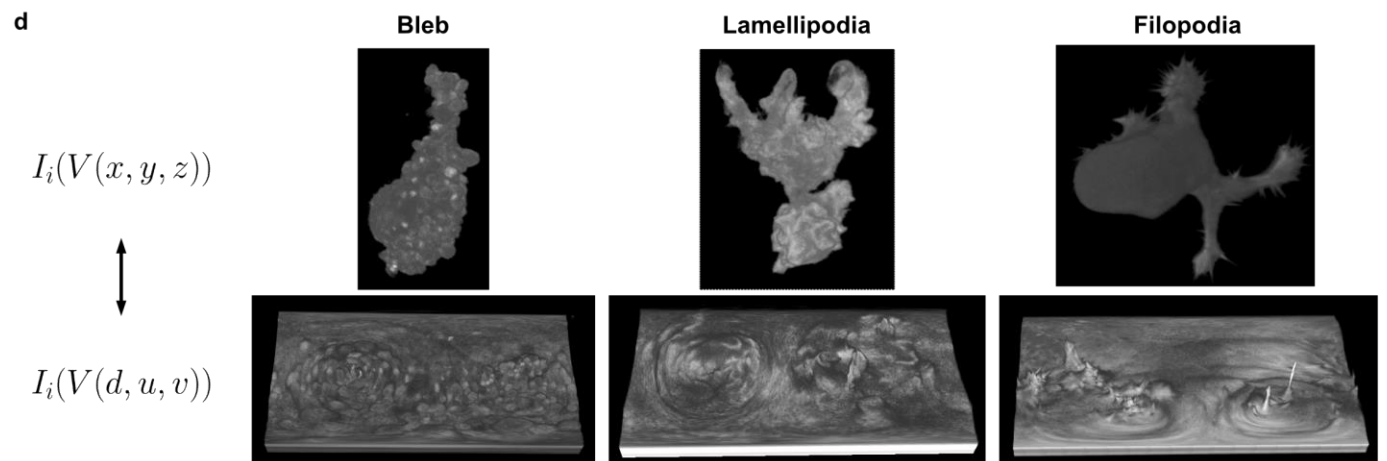
232

233



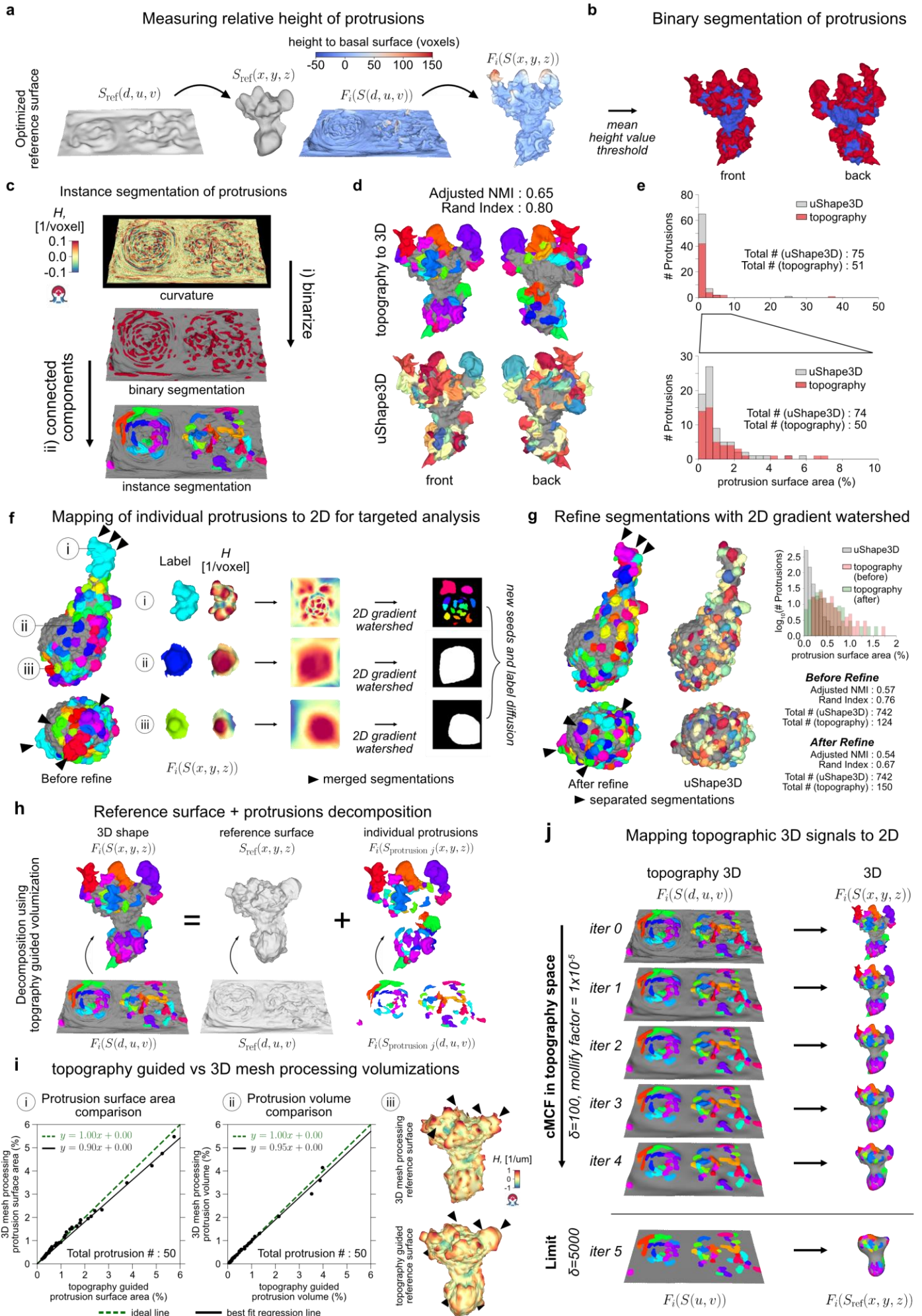
c

$F_i(S(x, y, z))$	$F_i(S_{\text{ref}}(x, y, z))$	$F_i(S_{\Omega}^2(x, y, z))$	$F_i(S(u, v))$	$F_i(S(d, u, v))$
<p>Bleb</p> <p>(genus-577) #V: 324,130 #F: 650,588</p>	<p>(genus-0)</p>			
<p>Lamellipodia</p> <p>(genus-7) #V: 163,646 #F: 327,316</p>	<p>(genus-0)</p>			
<p>Filopodia</p> <p>(genus-2694) #V: 380,922 #F: 772,900</p>	<p>(genus-0)</p>			

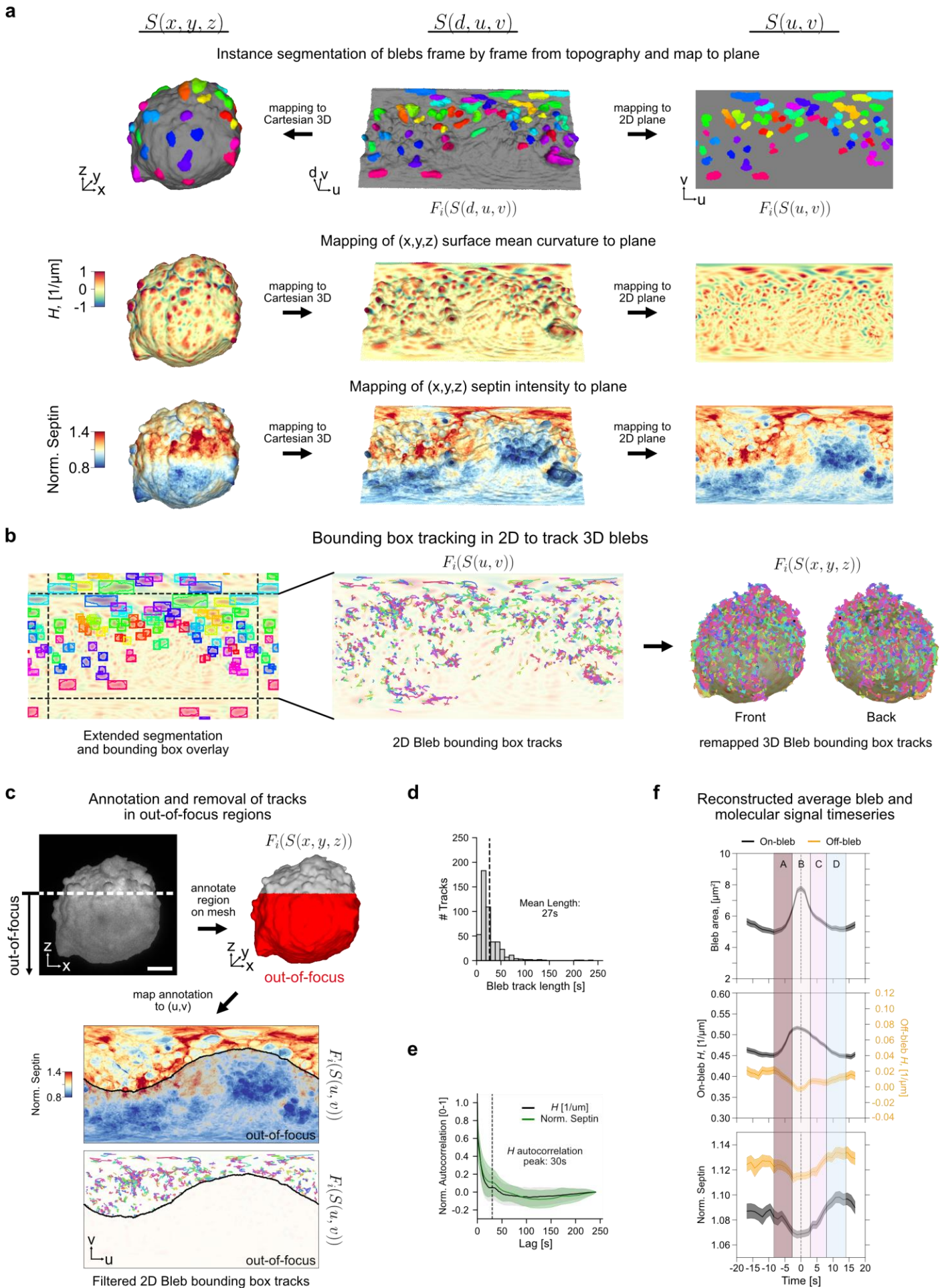


235 **Figure 2. u-Unwrap3D generates a spectrum of equivalent data representations for surface-guided**
236 **computing. a)** Summary of the bijective mappings between the 5 equivalent surface mesh representations
237 generated by u-Unwrap3D. Black bidirectional arrows indicate the mapping algorithms between
238 representations discussed in the text. Grey arrow indicates the direct spherical mapping applicable when the
239 input mesh is genus-0. **b)** u-Unwrap3D also enables bidirectional mapping of volumetric information between
240 a Cartesian and topographic space relative to a genus-0 reference surface. **c)** Gallery of equivalent surface
241 representations generated on examples of cell surfaces with blebs, lamellipodia and filopodia. For
242 visualization of the mappings, individual instances of morphological motifs detected by the software
243 uShape3D are color-coded on surface representations. **d)** Gallery of equivalent volume representations for
244 the same cells shown in c). Volume image intensities were visualized using ImageJ volume viewer and
245 contrast-enhanced to better visualize fine protrusions (see Methods).

246



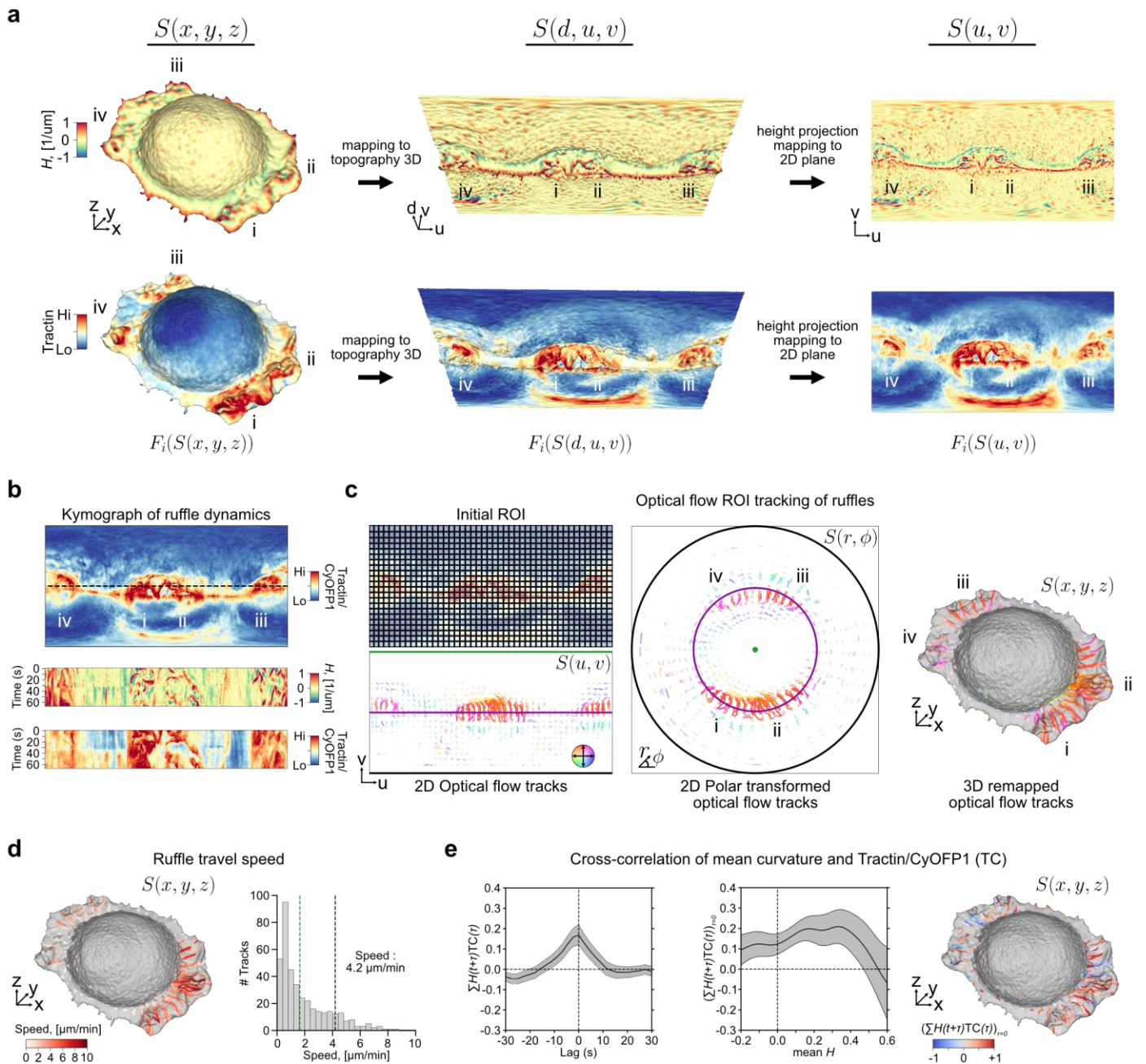
248 **Figure 3. u-Unwrap3D enables segmentation and characterization of complex 3D surface**
249 **morphologies. a)** The d -coordinate of the topographic 3D surface directly measures the protrusion height
250 $S(x, y, z)$ of the input surface relative to the reference surface $S_{\text{ref}}(x, y, z)$. Here, $S_{\text{ref}}(x, y, z)$ was optimized for
251 delineating surface protrusions (see Extended Fig. 4a,b). **b)** Surface segmentation obtained by binary
252 thresholding of the height measured relative to the optimized (blue) reference surface (see Extended Fig. 4c).
253 Surface protrusions above the threshold are in red. **c)** Overview of an unsupervised pipeline to detect and
254 segment protrusion instances by thresholding the topographic curvature and connected component labeling
255 (see Extended Fig. 4d). Individual protrusions are uniquely colored. **d)** Comparison of the topography-guided
256 protrusion segmentation with supervised uShape3D morphological motif detection. Individual protrusions are
257 uniquely colored. Quantitative concordance was measured by adjusted normalized mutual information (NMI,
258 0-1) and Rand index (0-1). **e)** Comparison of the surface area of topography-guided (red bars) and
259 uShape3D-based (grey bars) segmented protrusions plotted relative to the full reference surface (top)
260 including the grey colored cortical surface and zoomed-in (indicated by the polygon) comparing only the
261 surface area of segmented protrusions (bottom). **f)** Selective 2D unwrapping of 3 individual segmented
262 protrusions labelled i-iii) into corresponding 2D disk and square representations for fine-grained segmentation
263 of under-segmented protrusions **g)** Application of a watershed algorithm to the 2D representations refines
264 under-segmented protrusions. The bijectivity of all intermediary mappings permits the representation of
265 coarse- and fine-grained segmentations back on the 3D surface. Comparison of the final protrusion
266 segmentation to the segmentation before refinement (see f)) and to the motifs detected by uShape3D.
267 Quantitative concordance was measured by adjusted normalized mutual information (NMI, 0-1) and Rand
268 index (0-1). **h)** Decomposition of an input Cartesian 3D surface (left) into reference cortical surface (grey
269 colored) (middle) and individual meshes (uniquely colored) per segmented protrusion (right). The
270 decompositions were guided by the topographic representations (bottom) (see Extended Fig. 4e-g). The
271 decomposed surface meshes are closed and define individual volumes (i.e. volumized). **i)** Comparison of the
272 surface area (left, labelled i) and volumes (middle, labelled ii) of individual protrusions computed from u-
273 Unwrap3D topography guided from h) (x-axis) or standard 3D mesh processing (see Methods) volumized
274 surface meshes (y-axis). Reconstructed reference cortical surface meshes without protrusions and colored
275 by mean curvature using from u-Unwrap3D topography guidance (bottom) or standard 3D mesh processing
276 (top) (right, labelled iii). Black triangles highlight mechanically implausible surface features left by standard
277 3D mesh processing. **j)** Illustration of the modified conformalized mean curvature flow (cMCF) to directly map
278 topographic 3D surfaces and associated signals (here, segmented protrusions marked by unique colors) to
279 the 2D plane, an optimal representation for tracking individual protrusions.



282 **Figure 4. u-Unwrap3D enables tracking and characterization of blebs and associated signals. a)**
283 Individual blebs segmented in topographic 3D representation are mapped to Cartesian 3D for visualization
284 and to the 2D plane for tracking (top). Individual blebs are uniquely colored. Mean curvature, H (middle) and
285 normalized Septin intensities (bottom) are jointly mapped from Cartesian 3D to topographic 3D to the 2D
286 plane. The Septin intensity is normalized at each time to the mean Septin intensity in the whole cell volume
287 to correct for expression variation and photobleaching. **b)** Tracking of individual blebs using an optical flow-
288 guided 2D bounding box tracker. The unwrapped (u, v) -map is padded on all four sides to capture the
289 continuation of the spherical surface (dashed black lines). Because of the bijectivity between representations
290 individual bleb bounding box tracks in 2D (middle) can be mapped to 3D (right). **c)** Bijective mappings enable
291 the transfer of manually annotated out-of-focus in Cartesian 3D to the unwrapped (u, v) 2D plane to restrict
292 intensity timeseries analyses to only the bleb tracks within the in-focus surface regions. The decay in image
293 contrast with sample depth is shown in a maximum projection image of the first timepoint restricted to the
294 segmented surface $\pm 1 \mu\text{m}$ (Methods). Scalebar: $10 \mu\text{m}$. **d)** Histogram of the in-focus bleb track lengths
295 (dashed line, mean length). **e)** Autocorrelation curves (mean \pm standard deviation) of mean curvature, H and
296 Septin computed from Cartesian 3D meshes. Dashed black line depicts the lag time of the first autocorrelation
297 side lobe of mean curvature, H . **f)** Average (mean \pm s.e.m) time course of bleb surface area (top), mean
298 curvature (on bleb, black; off bleb, orange, and Septin intensity (bottom) over a window 17.5s before to 17.5s
299 after the timepoint of maximum bleb size used for alignment ($n=545$ bleb events from $m=1$ cell). A-D labels
300 distinct phases of bleb-mediated curvature Septin recruitment.

301

302



303

304

305 **Figure 5. u-Unwrap3D enables tracking and characterization of morphological and molecular**

306 **dynamics. a)** Unwrapping of a ruffling SU.86.86 pancreatic adenocarcinoma cell visualized in Cartesian 3D

307 (left), topographic 3D (middle) and unwrapped 2D plane (right) representations for the first frame of a

308 timelapse 3D image sequence sampled every 2.27s for 30 frames. Top row: mean curvature; bottom row:

309 Tractin-mEmerald intensity sampled 1 μm from the cell surface. Labels i-iv indicate corresponding landmarks

310 in all three representations. **b)** Cross-section (dashed black line, top) to generate kymographs (bottom) of

311 mean curvature and Tractin-mEmerald intensity normalized to myristolated CyOFFP1 as a diffuse volumetric

312 marker. **c)** Optical flow tracking on equipartitioned regions of interest (ROI) in the (u, v) -plane of ruffles based

313 on the Tractin/CyOFFP1 (TC) ratiometric intensity (left). The resultant optical flow ROI tracks are colored by

314 the mean track direction. Color saturation indicates mean track speed. ROI tracks remapped to 2D polar

315 (r, ϕ) view (middle) and to Cartesian 3D (x, y, z) surface representation overlaid on the first time point (right).

316 The polar transform maps the green (top), purple (middle) and black (bottom) horizontal line in the (u, v) -

317 plane to the central green point, purple and black rings in the (r, ϕ) -view, respectively. **d)** Mean temporal

318 planar travel speed of the ruffle-associated ROI tracks from c) plotted onto the Cartesian 3D surface

319 representation of the first time point (left) and histogram (right). We infer a mean ruffle travel speed of 4.2

320 $\mu\text{m}/\text{min}$ corresponding to the faster of the two histogram populations (black vertical dashed lines) using 3-

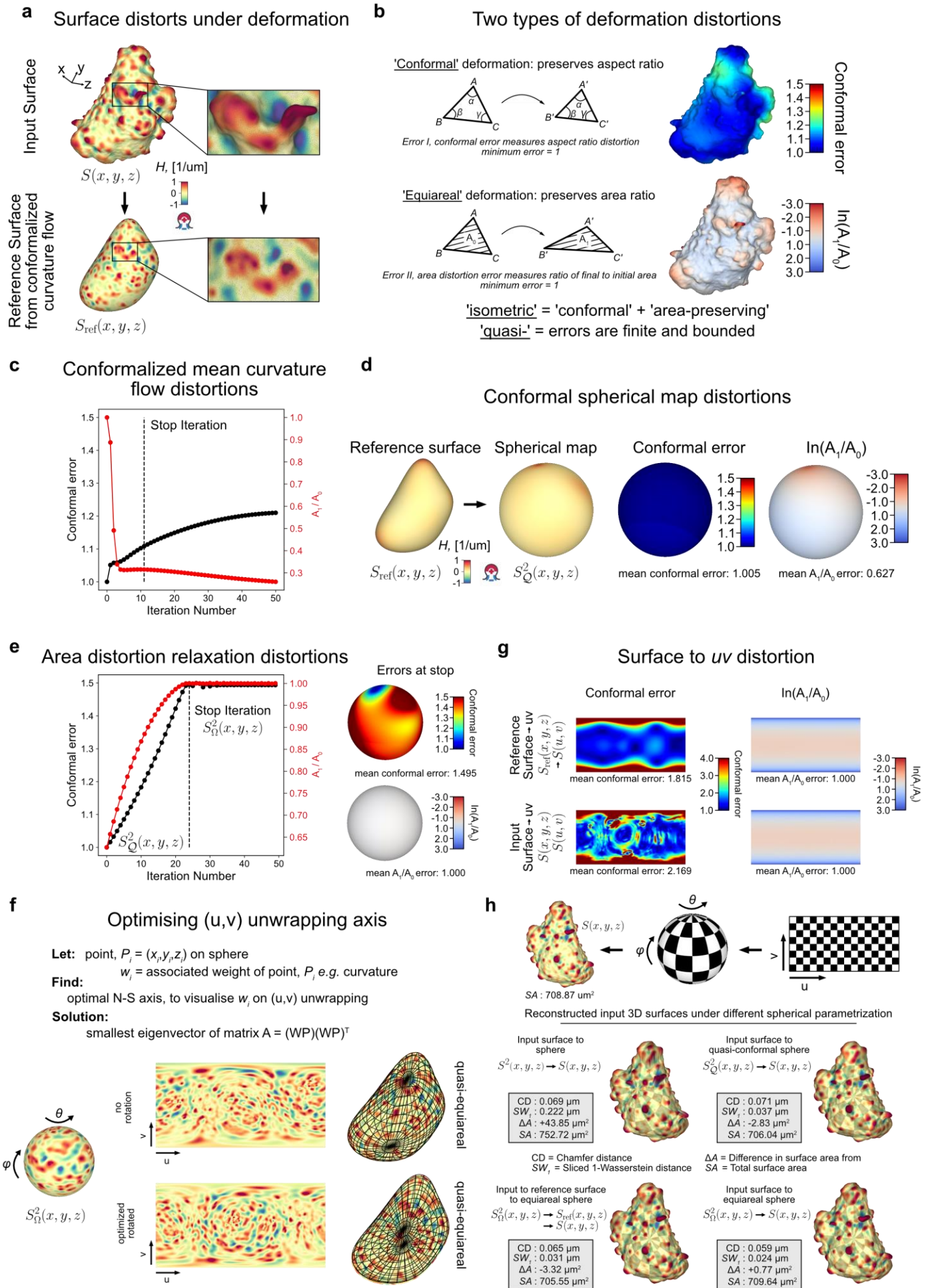
321 class Otsu thresholding (see Methods). **e)** Cross-correlation curve (mean \pm 95% confidence interval) between

mean curvature and TC timeseries per ROI track (left). Lag 0 cross-correlation of mean curvature and TC as

322 a function of mean curvature, H (middle); ROI tracks color-coded by cross-correlation magnitude plotted onto
323 the Cartesian 3D surface representation of the first time point (right).

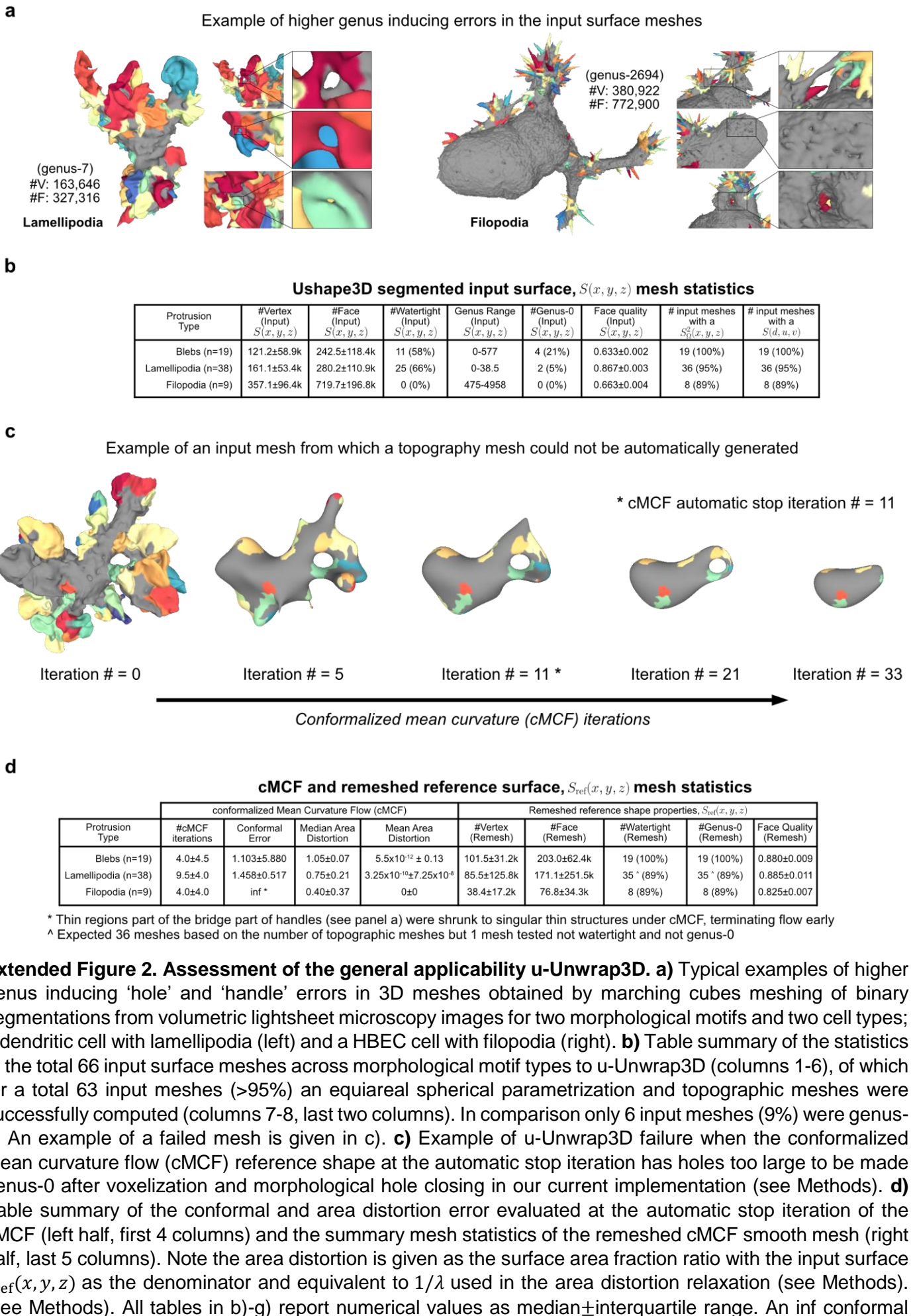
324

325



327 **Extended Figure 1. Measuring and optimizing mesh distortion under surface deformation.** **a)** Any
328 deformation of a closed 3D surface mesh (top) such as by conformalized mean curvature flow (cMCF)
329 (bottom) distorts local geometrical distances and areas as illustrated by zoom-ins. **b)** Illustration of the two
330 types of metric distortion incurred by mesh deformation; conformal and equiareal. In general, lower conformal
331 error is at the expense of equiareal and vice versa. **c)** Plot of the conformal error (black dotted line, black left
332 y-axis) and area ratio (red dotted line, red right y-axis) for each iteration of cMCF (Step 1, Fig. 1b) for the
333 example mesh in a) and Fig. 1 with stop iteration indicated by a black vertical dashed line. **d)** Rendering of
334 the conformal error and area ratio error at each triangle face for quasi-conformal spherical parametrization
335 of the smooth shape to the sphere (Step 2, Fig. 1b). **e)** Plot of the conformal error (black dotted line, black
336 left y-axis) and area ratio (red dotted line, red right y-axis) for each iteration of the spherical area distortion
337 relaxation with stop iteration indicated by a black vertical dashed line (Step 3, Fig. 1b), (left). Rendering of
338 the conformal and area ratio error of individual triangle faces at the stop iteration, (right). **f)** Illustration of not
339 optimising (upper row) and optimising the unwrapping north-south axis using weighted principal component
340 analysis to maximally display protrusive surface features with minimal distortion using the absolute value of
341 mean curvature of the smooth 3D shape as weights, w (lower row). **g)** Comparison of the per pixel conformal
342 error (left column) and area distortion (right column) of the 2D (u, v) unwrapping of the cMCF smooth shape,
343 $S_{\text{ref}}(x, y, z)$ (upper row) or direct unwrapping of the input shape, $S(x, y, z)$ (lower row). **h)** Quantitative
344 assessment of four different options of 2D (u, v) unwrapping an input surface, $S(x, y, z)$ via different spherical
345 parameterizations, $S^2(x, y, z)$ by measuring the difference between the Cartesian 3D reconstructed mesh
346 from $S(u, v)$ and $S(x, y, z)$. CD = Chamfer distance, SW_1 = sliced 1-Wasserstein distance between vertices of
347 the input and reconstructed mesh. SA = the total surface. ΔA = difference in total surface area between the
348 input and reconstructed mesh. Qualitative assessment by uv-remapping the chessboard pattern and blending
349 with the mean curvature, H colors.

350



351

352

353

354

355

356

357

358

359

360

361

362

363

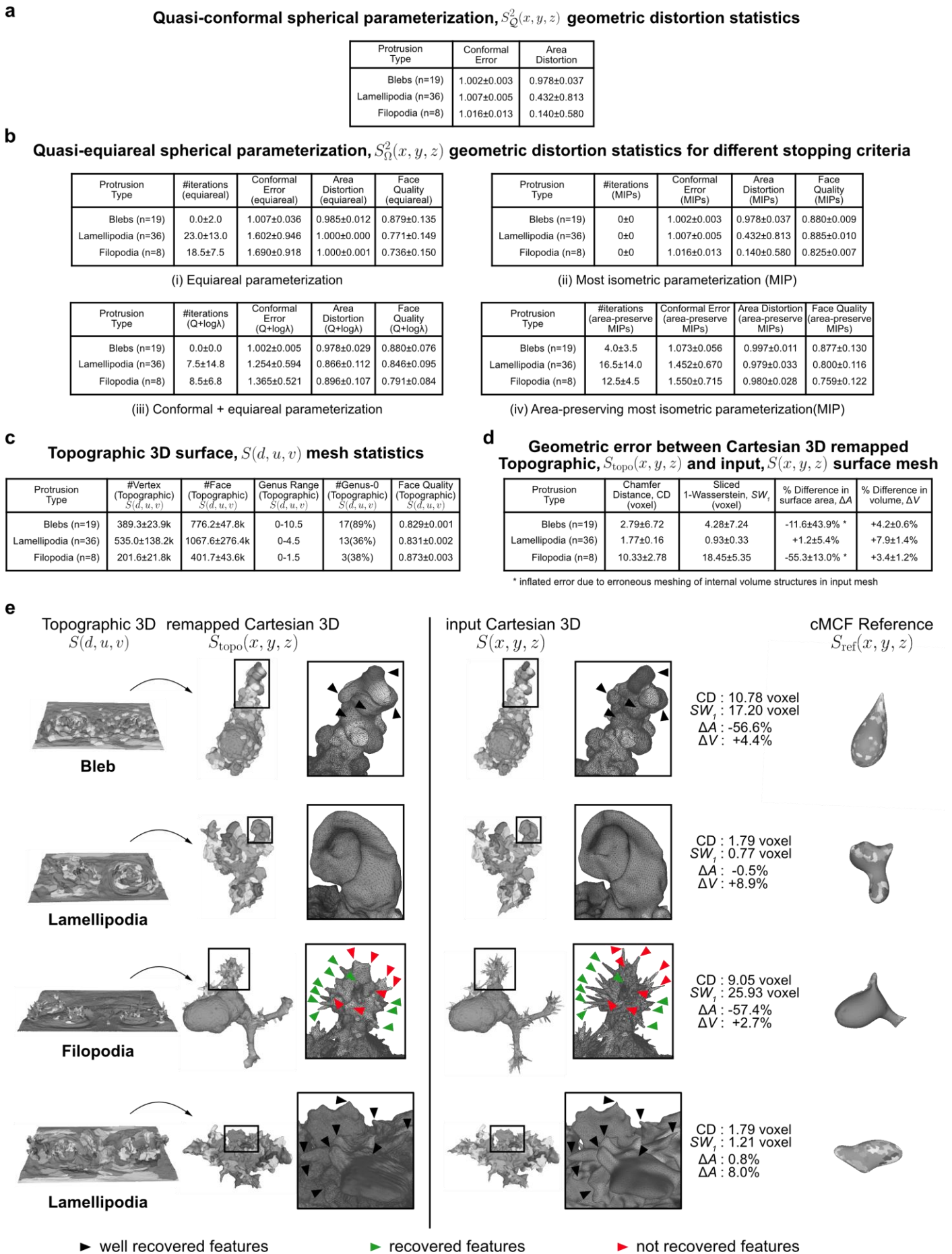
364

365

366

Extended Figure 2. Assessment of the general applicability u-Unwrap3D. **a)** Typical examples of higher genus inducing ‘hole’ and ‘handle’ errors in 3D meshes obtained by marching cubes meshing of binary segmentations from volumetric lightsheet microscopy images for two morphological motifs and two cell types; a dendritic cell with lamellipodia (left) and a HBEC cell with filopodia (right). **b)** Table summary of the statistics of the total 66 input surface meshes across morphological motif types to u-Unwrap3D (columns 1-6), of which for a total 63 input meshes (>95%) an equiareal spherical parametrization and topographic meshes were successfully computed (columns 7-8, last two columns). In comparison only 6 input meshes (9%) were genus-0. An example of a failed mesh is given in c). **c)** Example of u-Unwrap3D failure when the conformalized mean curvature flow (cMCF) reference shape at the automatic stop iteration has holes too large to be made genus-0 after voxelization and morphological hole closing in our current implementation (see Methods). **d)** Table summary of the conformal and area distortion error evaluated at the automatic stop iteration of the cMCF (left half, first 4 columns) and the summary mesh statistics of the remeshed cMCF smooth mesh (right half, last 5 columns). Note the area distortion is given as the surface area fraction ratio with the input surface $S_{ref}(x, y, z)$ as the denominator and equivalent to $1/\lambda$ used in the area distortion relaxation (see Methods). (see Methods). All tables in b)-g) report numerical values as median±interquartile range. An inf conformal

367 error indicates local breakdown of flow for a mesh. When this occurs, cMCF cannot continue and the
368 automatic stop iteration is the iteration # just prior to breakdown.



369

370

371

372

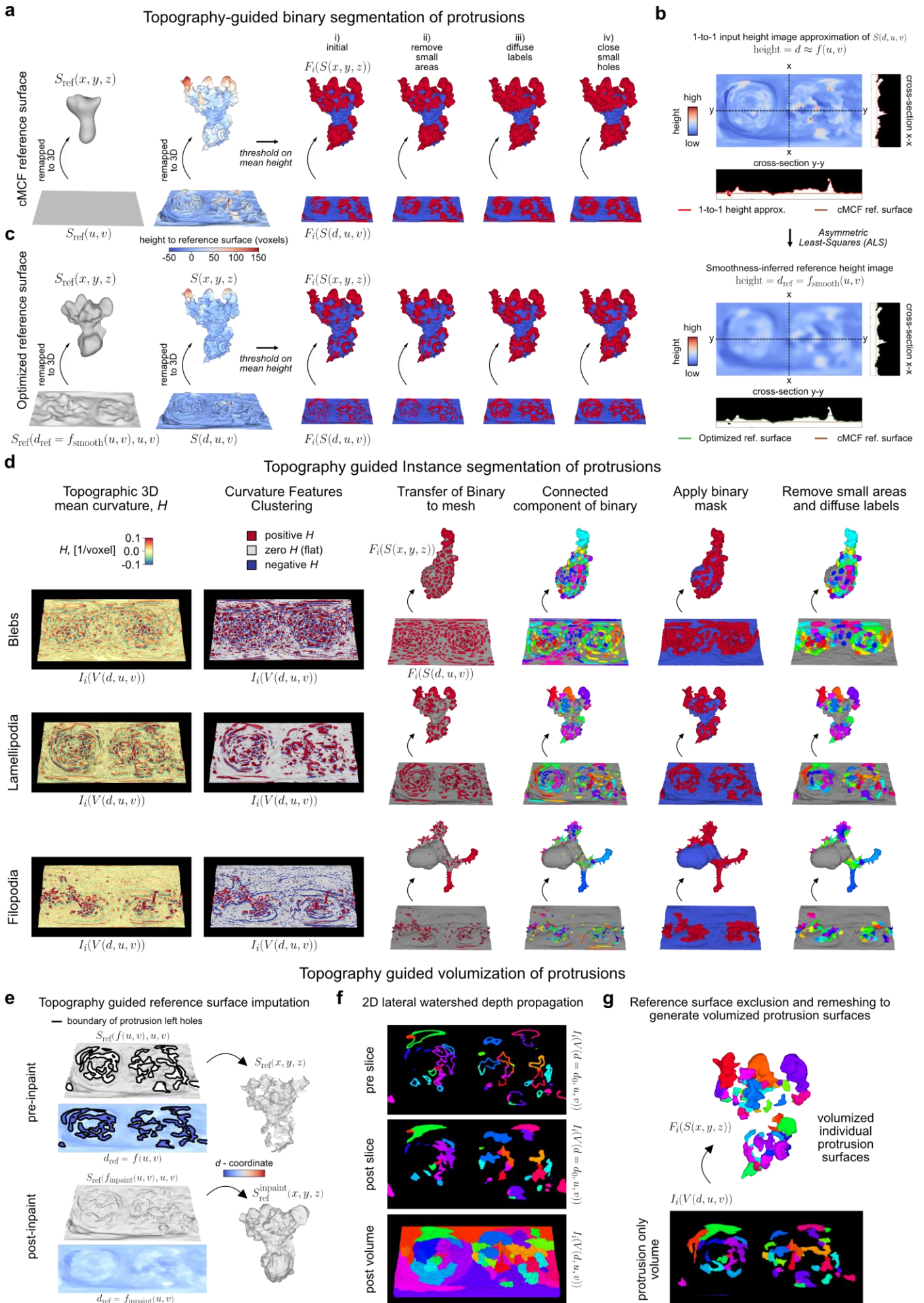
373

Extended Figure 3. Quantitative performance assessment of the geometric deformation steps in Unwrap3D. **a)** Table summary of the conformal and area distortion error of quasi-conformal spherical parameterization of the cMCF reference surface, $S_{\text{ref}}(x, y, z) \rightarrow S_Q^2(x, y, z)$, (Step 2 Fig. 1b). The target and optimal minimum conformal error is 1.0 and is achieved. **b)** Table summary of the number of iterations,

374 conformal and area distortion error and mesh quality for four different stopping criteria (labelled i-iv, see
375 Methods) for area-distortion relaxation of $S_Q^2(x, y, z) \rightarrow S_\Omega^2(x, y, z)$. The target and optimal minimum area
376 distortion is 1.0. The implemented spherical area-distortion relaxation scheme in this paper achieves the
377 optimal area distortion, an equiareal parametrization in $t_\Omega < a$ maximum allowed 50 iterations by minimising
378 directly the area-distortion factor, λ (equiareal) criterion (Methods) (top left, i). The scheme further allows
379 relaxations between conformal and equiareal parametrizations as demonstrated by three additional stopping
380 criteria: with no relaxation, (i.e. iteration 0) the parameterization is conformal and the most isometric
381 parametrization (MIPS) (top right, ii); for iteration numbers $t \approx \frac{1}{2}t_\Omega$, the parameterization minimises jointly
382 the combined conformal and area distortion as measured by $Q + \log \lambda$, the sum of the quasi-conformal
383 error, Q and the natural logarithm of the area distortion factor, λ (bottom left, iii); and for iteration numbers
384 $t \lesssim t_\Omega$, the parameterization is the area-preserving MIPS (bottom right, iv). **c)** Table summary of the statistics
385 for computed topographic meshes, $S(d, u, v)$ using a 1024×512 pixel (u, v) grid for the subset of $n = 63$
386 meshes with successful equiareal spherical parametrizations, $S_\Omega^2(x, y, z)$ (Extended Fig. 2b). **d)** Table
387 summary of the quantitative measurement of geometric error between the Cartesian 3D remapping,
388 $S_{\text{topo}}(x, y, z)$ of the topographic mesh, $S(d, u, v)$ and the original input mesh $S(x, y, z)$ for four metrics; (*CD*)
389 chamfer distance (1st column), (SW_1) sliced 1-Wasserstein (2nd column), ΔA , the percentage difference in total
390 surface area (3rd column) and ΔV , the percentage difference in total volume (4th column). For a perfect
391 reconstruction, all measures should be 0. Units are given as voxels due to heterogeneous pixel resolution
392 amongst input meshes. A large ΔA , but small ΔV for blebs and filopodia were due to a subset of non-
393 watertight input meshes found to have erroneously meshed what should be the internal cell volume. These
394 meshes were typically characterised by very high-genus (>50) (Extended Fig. 2c). Note in a)-d) the area
395 distortion is given as the surface area fraction ratio with the input surface $S_{\text{ref}}(x, y, z)$ as the denominator and
396 equivalent to $1/\lambda$ used in the area distortion relaxation (see Methods). All tables in a)-d) report numerical
397 values as median \pm interquartile range. **e)** Quantitative and qualitative comparison of the Cartesian 3D
398 remapping, $S_{\text{topo}}(x, y, z)$ of the topographic mesh, $S(d, u, v)$ (left) and the original input mesh $S(x, y, z)$
399 (middle) for 4 cell examples with different morphological motifs from d) in relation to the cMCF reference
400 surface, $S_{\text{ref}}(x, y, z)$ (right). Box shows a zoom-in of the local surface region for each example. Black triangles
401 highlight exemplar salient surface that are well captured but may be slightly smoothed and blurred in
402 $S_{\text{topo}}(x, y, z)$ due to being underrepresented surface regions in $S(d, u, v)$, being distant from $S_{\text{ref}}(x, y, z)$.
403 Green triangles highlight exemplar salient filopodia captured in $S_{\text{topo}}(x, y, z)$. Red triangles highlight exemplar
404 salient filopodia not or poorly captured in $S_{\text{topo}}(x, y, z)$, due to being in a region of dense filopodia and is
405 distant from $S_{\text{ref}}(x, y, z)$.

406

407



409

410

Extended Figure 4. Overview of an unsupervised pipeline to segment complex surface morphologies guided by topographic 3D representations.

411

412

413

414

415

416

417

418

419

420

421

422

423

424

425

426

427

428

429

430

431

432

433

434

435

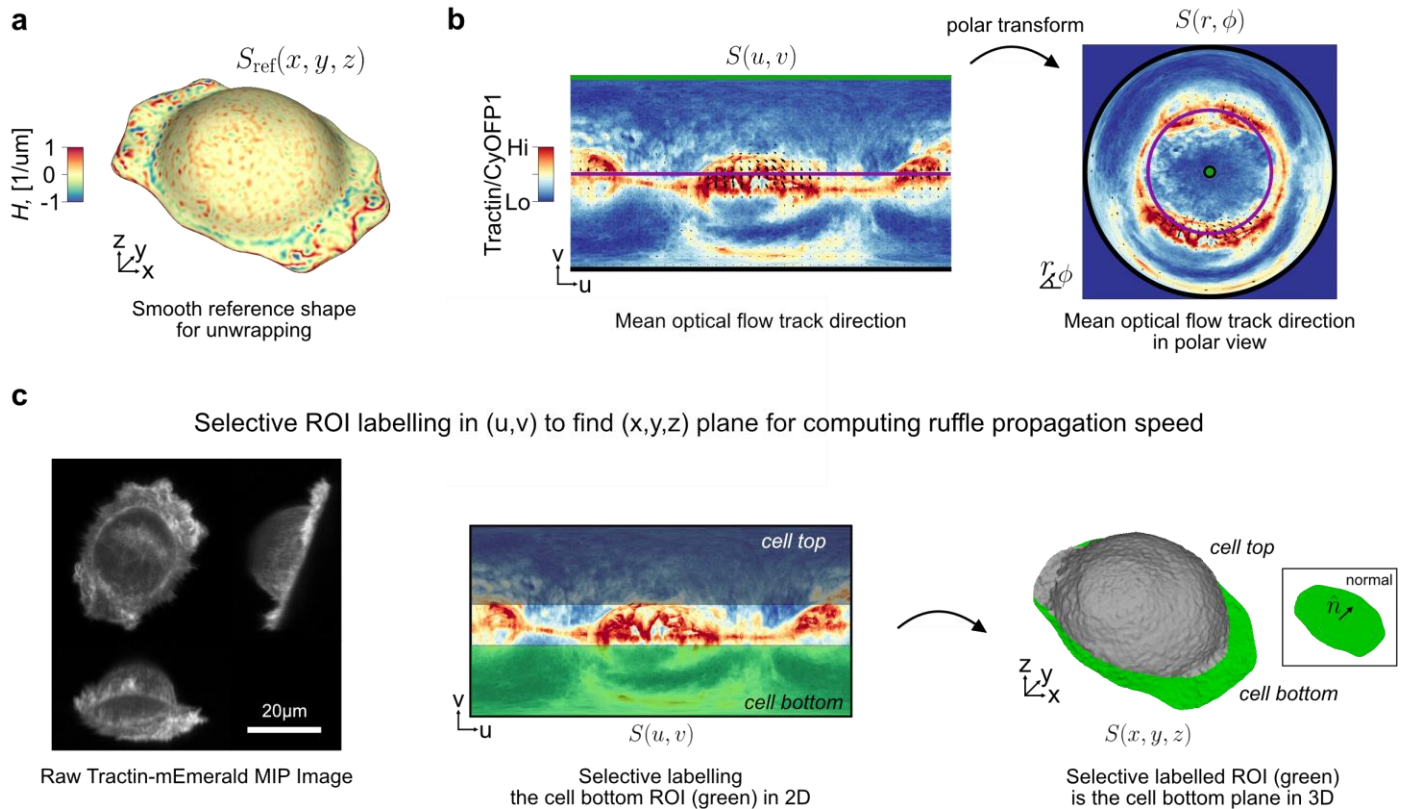
436

437

438

439

a) Overview of the four key steps (i-iv) to binary segment protrusions by thresholding on the mean height measured relative to the cMCF reference surface. **b)** Learning an optimal reference surface for segmenting surface protrusions using asymmetric least mean squares (ALS) (Methods). The topographic surface, $S(d, u, v)$ is approximated by a surface, $S(d = f(u, v), u, v)$ that is in 1-to-1 correspondence to every (u, v) pixel and can be represented as a height image using ray-propagation (top, see Methods). The height function, f is depicted additionally in cross-section cuts x-x and y-y by a red line. A flat brown line in cross-section depicts the cMCF reference, $S_{\text{ref}}(d, u, v)$. ALS with smoothness regularization is applied to $d = f(u, v)$ to derive an optimal smooth reference surface with height, $d = f_{\text{smooth}}(u, v)$ (bottom). The height function, f_{smooth} are depicted additionally in cross-section cuts x-x and y-y by a green line. **c)** Binary segmented protrusions by thresholding on the mean height measured relative to the ALS-derived reference surface from b). **d)** Overview of the sequential steps, left-to-right to segment individual protrusions by binarization and connected components analysis of topographic volume signals, $I_i(V(d, u, v))$. The steps are illustrated for 3 different cell types and 3 different surface motifs; MV3 melanoma cell with blebs (top row), dendritic cell with lamellipodia (middle row) and HBEC cell with filopodia (bottom row). Initial binarization uses 3-class k-means clustering (blebs and filopodia) and 3-class Gaussian mixture model clustering (lamellipodia) of volumetric mean curvature to identify all positive curvature regions. **e)** The hole-ridden ($d = 0$, black outline, and dark blue colored) reference surface, $S_{\text{ref}}(d_{\text{ref}} = f(u, v), u, v)$ (left) and corresponding remapped Cartesian 3D surface (right) after removal of all protrusion mesh faces (top). The inpainted topographic 3D reference surface, $S_{\text{ref}}(d_{\text{ref}} = f_{\text{inpaint}}(u, v), u, v)$ (left) and corresponding remapped Cartesian 3D surface (right) after image inpainting the missing d coordinates (bottom). **f)** Marker-seeded 2D watershed to laterally propagate surface segmentation labels into the topographic volume shown pre- (top) and post- (middle) for a single given slice at depth, $d = d_0$. The resulting labelled topographic volume after propagating all surface protrusion labels fully from the top to the bottom (bottom). Unique colors denote unique regions with the same surface label. **g)** The protrusion-only topographic volume labels (bottom) and resultant composition of individual volumized protrusion meshes (top) after using the inpainted basal surface from e) to mask out all non-protrusion voxels in f) and meshing. Individual protrusions are uniquely colored.



440

441

442

443

444

445

446

447

448

449

450

451

452

453

454

Extended Figure 5. u-Unwrap3D enabled measurement of ruffle in-plane travel speed. **a)** Cortical reference shape, $S_{\text{ref}}(x, y, z)$ found by applying conformalized mean curvature flow to the first timepoint of the ruffling SU.86.86 cell in Fig. 5a and used to unwrap all timepoints into a common static (d, u, v) space. **b)** The mean track velocity of the optical flow region-of-interest (ROI) tracks, plotted as black arrows at the initial track coordinate overlaid on the unwrapped Tractin-mEmerald/CyOFP1 intensity image of Fig. 5b (left) and its corresponding polar transformed equivalent (right). The polar transform maps the green (top), purple (middle) and black (bottom) horizontal line on the left to the central green point, second purple and third black rings in the polar image. **c)** Orthogonal cross-section maximum intensity projection (MIP) image of the raw Tractin-mEmerald intensity channel showing the tilted lightsheet acquisition (left). Selective ROI isolation of the top and bottom surface of the cell by grey and green bounding box selection in unwrapped view (middle) and visualized in 3D with grey and green surfaces respectively (right). The normal vector, \hat{n} describing the best fit plane through only the cell bottom vertices found by principal components analysis (inset rectangle).

455 **Supplementary Videos**

456

457 **Supplementary Video 1.** Overview of the six key steps of u-Unwrap3D.

458 **Supplementary Video 2.** Application of u-Unwrap3D to directly unwrap a genus-0 cell surface mesh in
459 conjunction with the spatial activation pattern of PI3K signaling products.

460 **Supplementary Video 3.** Application of u-Unwrap3D to an MV3 melanoma cell with bleb surface motifs
461 segmented by the u-shape3D software. Each bleb is labelled with a random color to demonstrate the local
462 surface mappings and their distortions.

463 **Supplementary Video 4.** Application of u-Unwrap3D to a dendritic cell with lamellipodia surface motifs
464 segmented by the u-shape3D software. Each lamellipodium is labelled with a random color to demonstrate
465 the local surface mappings and their distortions.

466 **Supplementary Video 5.** Application of u-Unwrap3D to an HBEC cell with filopodia surface motifs
467 segmented by the u-shape3D software. Each filopodium is labelled with a random color to demonstrate the
468 local surface mappings and their distortions.

469 **Supplementary Video 6.** Application of topographic conformalized mean curvature flow to directly map the
470 topographic surface $S(d, u, v)$ of a dendritic cell with segmented lamellipodia surface motifs to the 2D plane,
471 $S(u, v)$ for two different time steps, $\delta = 100$ and $\delta = 5000$. The smaller δ enables gradual relaxation and the
472 ability to sample and use intermediate shapes during the flow. However smooth low curvature folds remain
473 such that we do not fully converge to the plane even if continued to 100 iterations. For direct mapping to the
474 plane we always use the large δ to ensure convergence within 50 iterations.

475 **Supplementary Video 7.** Application of u-Unwrap3D to enable segmentation and tracking of blebs on a MV3
476 melanoma cell in topographic representation. View 1: Projections of cell surface, mean curvature and
477 normalized SEPT6-GFP into topographic surface and (u, v) unwrapped reference surface representations.
478 Individual blebs are segmented by thresholding in the topographic surface representation. Leveraging the
479 bijectivity of u-Unwrap3D mappings bleb labels are projected back to the 3D surface. View 2: The 2D
480 segmented blebs are tracked and trajectories projected back to the original 3D surface. The timelapse
481 volumes were acquired every 1.21s for 200 frames. Scalebar: 10 μ m.

482 **Supplementary Video 8.** Application of u-Unwrap3D to track the surface ruffling and actin flows of a
483 SU.86.86 pancreatic adenocarcinoma. View 1: Projections of cell surface, mean curvature and Tractin-
484 mEmerald into topographic surface and (u, v) unwrapped reference surface representations. View 2:
485 Regional ruffling and actin flows are tracked in 2D with optical flow and trajectories projected into a 2D
486 polar representation and back to the original 3D surface. View 3: Select measurement of instantaneous
487 ruffle and actin flow speeds and cross-correlation of actin and curvature within the lamella and lamellipodia
488 taking advantage of the unwrapped (u, v) representation is projected back to the original 3D surface. The
489 timelapse volumes were acquired every 2.27s for 30 frames. Scalebar: 20 μ m.

490

491

492

493

494

References

495
496

- 1 Mitra, A. *et al.* Cell geometry dictates TNF α -induced genome response. *Proceedings of the National Academy of Sciences* **114**, E3882-E3891 (2017).
- 2 Wang, Y., Nagarajan, M., Uhler, C. & Shivashankar, G. Orientation and repositioning of chromosomes correlate with cell geometry–dependent gene expression. *Molecular biology of the cell* **28**, 1997-2009 (2017).
- 3 McBeath, R., Pirone, D. M., Nelson, C. M., Bhadriraju, K. & Chen, C. S. Cell shape, cytoskeletal tension, and RhoA regulate stem cell lineage commitment. *Developmental cell* **6**, 483-495 (2004).
- 4 Welf, E. S. *et al.* Quantitative Multiscale Cell Imaging in Controlled 3D Microenvironments. *Dev Cell* **36**, 462-475, doi:10.1016/j.devcel.2016.01.022 (2016).
- 5 Castor, L. N. Flattening, movement and control of division of epithelial - like cells. *Journal of Cellular Physiology* **75**, 57-64 (1970).
- 6 De Belly, H., Paluch, E. K. & Chalut, K. J. Interplay between mechanics and signalling in regulating cell fate. *Nature Reviews Molecular Cell Biology*, 1-16 (2022).
- 7 Vitriol, E. A. & Zheng, J. Q. Growth cone travel in space and time: the cellular ensemble of cytoskeleton, adhesion, and membrane. *Neuron* **73**, 1068-1081 (2012).
- 8 Shirao, T. & González - Billault, C. Actin filaments and microtubules in dendritic spines. *Journal of neurochemistry* **126**, 155-164 (2013).
- 9 Prasad, A. & Alizadeh, E. Cell form and function: interpreting and controlling the shape of adherent cells. *Trends in biotechnology* **37**, 347-357 (2019).
- 10 Alberts, B. *et al.* Molecular biology of the cell. *Scandinavian Journal of Rheumatology* **32**, 125-125 (2003).
- 11 Osumi-Sutherland, D. *et al.* Cell type ontologies of the Human Cell Atlas. *Nature Cell Biology* **23**, 1129-1135 (2021).
- 12 Watt, F. M., Jordan, P. W. & O'Neill, C. H. Cell shape controls terminal differentiation of human epidermal keratinocytes. *Proceedings of the National Academy of Sciences* **85**, 5576-5580 (1988).
- 13 Le Roux, A.-L., Quiroga, X., Walani, N., Arroyo, M. & Roca-Cusachs, P. The plasma membrane as a mechanochemical transducer. *Philosophical Transactions of the Royal Society B* **374**, 20180221 (2019).
- 14 Lomakin, A. *et al.* The nucleus acts as a ruler tailoring cell responses to spatial constraints. *Science* **370**, eaba2894 (2020).
- 15 Bronner, F. *Cell shape: determinants, regulation, and regulatory role.* (Elsevier, 2012).
- 16 Kholodenko, B. N. Cell-signalling dynamics in time and space. *Nature reviews Molecular cell biology* **7**, 165-176 (2006).
- 17 Axelrod, D. & Wang, M. Reduction-of-dimensionality kinetics at reaction-limited cell surface receptors. *Biophysical journal* **66**, 588-600 (1994).
- 18 Schmick, M. & Bastiaens, P. I. The interdependence of membrane shape and cellular signal processing. *Cell* **156**, 1132-1138 (2014).
- 19 Kholodenko, B. N., Hoek, J. B. & Westerhoff, H. V. Why cytoplasmic signalling proteins should be recruited to cell membranes. *Trends in cell biology* **10**, 173-178 (2000).
- 20 Adam, G. & Delbrück, M. Reduction of dimensionality in biological diffusion processes. *Structural chemistry and molecular biology* **198**, 198-215 (1968).
- 21 Neves, S. R. *et al.* Cell shape and negative links in regulatory motifs together control spatial information flow in signaling networks. *Cell* **133**, 666-680 (2008).
- 22 Rangamani, P. *et al.* Decoding information in cell shape. *Cell* **154**, 1356-1369, doi:10.1016/j.cell.2013.08.026 (2013).
- 23 Jaqaman, K. & Ditlev, J. A. Biomolecular condensates in membrane receptor signaling. *Current Opinion in Cell Biology* **69**, 48-54 (2021).
- 24 Edidin, M. Patches, posts and fences: proteins and plasma membrane domains. *Trends in cell biology* **2**, 376-380 (1992).
- 25 Sharp, N., Attaiki, S., Crane, K. & Ovsjanikov, M. Diffusionnet: Discretization agnostic learning on surfaces. *ACM Transactions on Graphics (TOG)* **41**, 1-16 (2022).
- 26 Klatzow, J., Dalmaso, G., Martínez-Abadías, N., Sharpe, J. & Uhlmann, V. μ Match: 3D Shape Correspondence for Biological Image Data. *Frontiers in Computer Science*, 7 (2022).
- 27 Lee, S. C. & Kazhdan, M. in *Computer Graphics Forum*. 27-37 (Wiley Online Library).
- 28 Van Kaick, O., Zhang, H., Hamarneh, G. & Cohen - Or, D. in *Computer graphics forum*. 1681-1707 (Wiley Online Library).

- 551 29 Cagniart, C., Boyer, E. & Ilic, S. in *2010 IEEE Computer Society Conference on Computer Vision and Pattern*
552 *Recognition*. 1339-1346 (IEEE).
- 553 30 Zeng, Y. *et al.* in *CVPR 2011*. 1225-1232 (IEEE).
- 554 31 Smith, B. *et al.* Constraining dense hand surface tracking with elasticity. *ACM Transactions on Graphics (TOG)*
555 **39**, 1-14 (2020).
- 556 32 Ovsjanikov, M., Ben-Chen, M., Solomon, J., Butscher, A. & Guibas, L. Functional maps: a flexible
557 representation of maps between shapes. *ACM Transactions on Graphics (ToG)* **31**, 1-11 (2012).
- 558 33 Bronstein, M. M. & Kokkinos, I. in *2010 IEEE computer society conference on computer vision and pattern*
559 *recognition*. 1704-1711 (IEEE).
- 560 34 Reuter, M., Schmansky, N. J., Rosas, H. D. & Fischl, B. Within-subject template estimation for unbiased
561 longitudinal image analysis. *Neuroimage* **61**, 1402-1418 (2012).
- 562 35 Reuter, M., Rosas, H. D. & Fischl, B. Highly accurate inverse consistent registration: a robust approach.
563 *Neuroimage* **53**, 1181-1196 (2010).
- 564 36 Markello, R. D. *et al.* Neuromaps: structural and functional interpretation of brain maps. *Nature Methods* **19**,
565 1472-1479 (2022).
- 566 37 Ciric, R. *et al.* TemplateFlow: FAIR-sharing of multi-scale, multi-species brain models. *Nature Methods*, 1-4
567 (2022).
- 568 38 Weems, A. D. *et al.* Blebs Promote Cell Survival by Assembling Oncogenic Signaling Hubs. *Nature*, 1-9 (2023).
- 569 39 Choi, P. T., Lam, K. C. & Lui, L. M. FLASH: Fast Landmark Aligned Spherical Harmonic Parameterization for
570 Genus-0 Closed Brain Surfaces. *SIAM Journal on Imaging Sciences* **8**, 67-94, doi:10.1137/130950008 (2015).
- 571 40 Floater, M. S. & Hormann, K. Surface parameterization: a tutorial and survey. *Advances in multiresolution for*
572 *geometric modelling*, 157-186 (2005).
- 573 41 Nadeem, S., Su, Z., Zeng, W., Kaufman, A. & Gu, X. Spherical parameterization balancing angle and area
574 distortions. *IEEE transactions on visualization and computer graphics* **23**, 1663-1676 (2016).
- 575 42 Joshi, A., Shattuck, D., Thompson, P. & Leahy, R. Brain image registration using cortically constrained
576 harmonic mappings. *Inf Process Med Imaging* **20**, 359-371, doi:10.1007/978-3-540-73273-0_30 (2007).
- 577 43 Zhao, F. *et al.* S3Reg: superfast spherical surface registration based on deep learning. *IEEE Transactions on*
578 *Medical Imaging* **40**, 1964-1976 (2021).
- 579 44 Lyu, I., Kang, H., Woodward, N. D., Styner, M. A. & Landman, B. A. Hierarchical spherical deformation for
580 cortical surface registration. *Medical image analysis* **57**, 72-88 (2019).
- 581 45 Driscoll, M. K. *et al.* Robust and automated detection of subcellular morphological motifs in 3D microscopy
582 images. *Nat Methods* **16**, 1037-1044, doi:10.1038/s41592-019-0539-z (2019).
- 583 46 Lefevre, J. G. *et al.* LLAMA: a robust and scalable machine learning pipeline for analysis of large scale 4D
584 microscopy data: analysis of cell ruffles and filopodia. *BMC bioinformatics* **22**, 1-26 (2021).
- 585 47 Castilla, C., Maška, M., Sorokin, D. V., Meijering, E. & Ortiz-de-Solórzano, C. 3-D quantification of filopodia in
586 motile cancer cells. *IEEE transactions on medical imaging* **38**, 862-872 (2018).
- 587 48 Botsch, M., Kobbelt, L., Pauly, M., Alliez, P. & Lévy, B. *Polygon mesh processing*. (CRC press, 2010).
- 588 49 Kazhdan, M., Solomon, J. & Ben - Chen, M. in *Computer Graphics Forum*. 1745-1754 (Wiley Online Library).
- 589 50 Gauss, K. F. & Pesic, P. *General investigations of curved surfaces*. (Courier Corporation, 2005).
- 590 51 Choi, G. P. T., Leung-Liu, Y., Gu, X. & Lui, L. M. Parallelizable Global Conformal Parameterization of Simply-
591 Connected Surfaces via Partial Welding. *SIAM Journal on Imaging Sciences* **13**, 1049-1083,
592 doi:10.1137/19m125337x (2020).
- 593 52 Ahlfors, L. V. *Lectures on quasiconformal mappings*. Vol. 38 (American Mathematical Soc., 2006).
- 594 53 Springborn, B. Hyperbolic polyhedra and discrete uniformization. *arXiv preprint arXiv:1707.06848* (2017).
- 595 54 Gu, X. D., Luo, F., Sun, J. & Wu, T. A discrete uniformization theorem for polyhedral surfaces. *Journal of*
596 *Differential Geometry* **109**, 223-256 (2018).
- 597 55 Gu, X., Guo, R., Luo, F., Sun, J. & Wu, T. A discrete uniformization theorem for polyhedral surfaces II. *Journal*
598 *of differential geometry* **109**, 431-466 (2018).
- 599 56 Heemskerk, I. & Streichan, S. J. Tissue cartography: compressing bio-image data by dimensional reduction.
600 *Nature methods* **12**, 1139-1142 (2015).
- 601 57 Li, M., Kaufman, D. M., Kim, V. G., Solomon, J. & Sheffer, A. Optcuts: Joint optimization of surface cuts and
602 parameterization. *ACM Transactions on Graphics (TOG)* **37**, 1-13 (2018).
- 603 58 Zhou, K., Synder, J., Guo, B. & Shum, H.-Y. in *Proceedings of the 2004 Eurographics/ACM SIGGRAPH*
604 *symposium on Geometry processing*. 45-54.
- 605 59 Sander, P. V., Wood, Z. J., Gortler, S., Snyder, J. & Hoppe, H. Multi-chart geometry images. (2003).
- 606 60 Mazloom-Farsibaf, H., Zou, Q., Hsieh, R., Danuser, G. & Driscoll, M. Cellular Harmonics for the Morphology-
607 invariant Analysis of Molecular Organization at the Cell Surface. *bioRxiv* (2022).

- 608 61 Stutz, D. (Master's thesis, RWTH Aachen University, 2017).
- 609 62 Hormann, K. & Greiner, G. MIPS: An efficient global parametrization method. (Erlangen-Nuernberg Univ
610 (Germany) Computer Graphics Group, 2000).
- 611 63 Degener, P., Meseth, J. & Klein, R. An Adaptable Surface Parameterization Method. *IMR* **3**, 201-213 (2003).
- 612 64 Bonneel, N., Rabin, J., Peyré, G. & Pfister, H. Sliced and radon wasserstein barycenters of measures. *Journal
613 of Mathematical Imaging and Vision* **51**, 22-45 (2015).
- 614 65 Saltukoglu, D. *et al.* Plasma membrane topography governs the three-dimensional dynamic localization of
615 IgM B cell receptor clusters. *bioRxiv* (2022).
- 616 66 Das, N. *et al.* 3dSpAn: An interactive software for 3D segmentation and analysis of dendritic spines.
617 *Neuroinformatics* **20**, 679-698 (2022).
- 618 67 Eilers, P. H. A perfect smoother. *Analytical chemistry* **75**, 3631-3636 (2003).
- 619 68 Whittaker, E. T. On a new method of graduation. *Proceedings of the Edinburgh Mathematical Society* **41**, 63-
620 75 (1922).
- 621 69 Liu, R. & Zhang, H. in *12th Pacific Conference on Computer Graphics and Applications, 2004. PG 2004.
622 Proceedings.* 298-305 (IEEE).
- 623 70 Rodrigues, R. S., Morgado, J. F. & Gomes, A. J. in *Computer Graphics Forum.* 235-274 (Wiley Online Library).
- 624 71 Agathos, A., Pratikakis, I., Perantonis, S. & Sapidis, N. S. Protrusion-oriented 3D mesh segmentation. *The
625 Visual Computer* **26**, 63-81 (2010).
- 626 72 Zhao, W., Gao, S. & Lin, H. A robust hole-filling algorithm for triangular mesh. *The Visual Computer* **23**, 987-
627 997 (2007).
- 628 73 Elliott, H. *et al.* Myosin II controls cellular branching morphogenesis and migration in three dimensions by
629 minimizing cell-surface curvature. *Nature cell biology* **17**, 137-147 (2015).
- 630 74 O'Shaughnessy, E. C. *et al.* Software for lattice light-sheet imaging of FRET biosensors, illustrated with a new
631 Rap1 biosensor. *Journal of Cell Biology* **218**, 3153-3160 (2019).
- 632 75 Charras, G. T., Coughlin, M., Mitchison, T. J. & Mahadevan, L. Life and times of a cellular bleb. *Biophysical
633 journal* **94**, 1836-1853 (2008).
- 634 76 Charras, G. A short history of blebbing. *Journal of microscopy* **231**, 466-478 (2008).
- 635 77 Driscoll, M. K. *et al.* Proteolysis-free cell migration through crowded environments via mechanical worrying.
636 *bioRxiv*, 2020.2011.2009.372912 (2022).
- 637 78 Leyden, F. *et al.* Rac1 activation can generate untemplated, lamellar membrane ruffles. *BMC biology* **19**, 1-14
638 (2021).
- 639 79 Ridley, A. J., Paterson, H. F., Johnston, C. L., Diekmann, D. & Hall, A. The small GTP-binding protein rac
640 regulates growth factor-induced membrane ruffling. *Cell* **70**, 401-410, doi:10.1016/0092-8674(92)90164-8
641 (1992).
- 642 80 Borm, B., Requardt, R. P., Herzog, V. & Kirfel, G. Membrane ruffles in cell migration: indicators of inefficient
643 lamellipodia adhesion and compartments of actin filament reorganization. *Experimental cell research* **302**,
644 83-95 (2005).
- 645 81 Planchon, T. A. *et al.* Rapid three-dimensional isotropic imaging of living cells using Bessel beam plane
646 illumination. *Nature methods* **8**, 417-423 (2011).
- 647 82 Spracklen, A. J., Fagan, T. N., Lovander, K. E. & Tootle, T. L. The pros and cons of common actin labeling tools
648 for visualizing actin dynamics during Drosophila oogenesis. *Developmental biology* **393**, 209-226 (2014).
- 649 83 Zhou, F. Y. *et al.* Characterization of Biological Motion Using Motion Sensing Superpixels. *Bio Protoc* **9**,
650 e3365, doi:10.21769/BioProtoc.3365 (2019).
- 651 84 Zhou, F. Y. *et al.* Motion sensing superpixels (MOSES) is a systematic computational framework to quantify
652 and discover cellular motion phenotypes. *Elife* **8**, doi:10.7554/eLife.40162 (2019).
- 653 85 Ponti, A., Machacek, M., Gupton, S. L., Waterman-Storer, C. M. & Danuser, G. Two distinct actin networks
654 drive the protrusion of migrating cells. *Science* **305**, 1782-1786 (2004).
- 655 86 Ju, T., Losasso, F., Schaefer, S. & Warren, J. in *Proceedings of the 29th annual conference on Computer
656 graphics and interactive techniques.* 339-346.
- 657 87 Portaneri, C., Rouxel-Labbé, M., Hemmer, M., Cohen-Steiner, D. & Alliez, P. Alpha wrapping with an offset.
658 *ACM Transactions on Graphics (TOG)* **41**, 1-22 (2022).
- 659 88 Huang, J., Zhou, Y. & Guibas, L. Manifoldplus: A robust and scalable watertight manifold surface generation
660 method for triangle soups. *arXiv preprint arXiv:2005.11621* (2020).
- 661 89 Huang, J., Su, H. & Guibas, L. Robust watertight manifold surface generation method for shapenet models.
662 *arXiv preprint arXiv:1802.01698* (2018).
- 663 90 El-Sana, J. & Varshney, A. in *Proceedings. Visualization'97 (Cat. No. 97CB36155).* 403-410 (IEEE).

- 664 91 Wood, Z., Hoppe, H., Desbrun, M. & Schröder, P. Isosurface topology simplification. *Microsoft Research MSR-*
665 *TR-2002* **28** (2002).
- 666 92 Hughes-Hallett, D., Gleason, A. M. & McCallum, W. G. *Calculus: Single and multivariable*. (John Wiley & Sons,
667 2020).
- 668 93 Aigerman, N. & Lipman, Y. Orbifold tutte embeddings. *ACM Trans. Graph.* **34**, 190:191-190:112 (2015).
- 669 94 Meng, T. W., Choi, G. P.-T. & Lui, L. M. Tempo: feature-endowed Teichmüller extremal mappings of point
670 clouds. *SIAM Journal on Imaging Sciences* **9**, 1922-1962 (2016).
- 671 95 Soliman, Y., Slepčev, D. & Crane, K. Optimal cone singularities for conformal flattening. *ACM Transactions on*
672 *Graphics (TOG)* **37**, 1-17 (2018).
- 673 96 Mildenhall, B. *et al.* Nerf: Representing scenes as neural radiance fields for view synthesis. *Communications*
674 *of the ACM* **65**, 99-106 (2021).
- 675 97 Yu, A., Ye, V., Tancik, M. & Kanazawa, A. in *Proceedings of the IEEE/CVF Conference on Computer Vision and*
676 *Pattern Recognition*. 4578-4587.
- 677 98 Yang, Y., Feng, C., Shen, Y. & Tian, D. in *Proceedings of the IEEE conference on computer vision and pattern*
678 *recognition*. 206-215.
- 679 99 Groueix, T., Fisher, M., Kim, V. G., Russell, B. C. & Aubry, M. in *Proceedings of the IEEE conference on*
680 *computer vision and pattern recognition*. 216-224.
- 681 100 Ern, A. & Guermond, J.-L. *Theory and practice of finite elements*. Vol. 159 (Springer, 2004).
- 682 101 Jacobson, A. *et al.* (2018).
- 683 102 Sharp, N. & Crane, K. in *Computer Graphics Forum*. 69-80 (Wiley Online Library).
- 684 103 Meyer, M., Desbrun, M., Schröder, P. & Barr, A. H. in *Visualization and mathematics III* 35-57 (Springer,
685 2003).
- 686 104 Lewiner, T., Lopes, H., Vieira, A. W. & Tavares, G. Efficient implementation of marching cubes' cases with
687 topological guarantees. *Journal of graphics tools* **8**, 1-15 (2003).
- 688 105 Valette, S. & Chassery, J. M. in *Computer Graphics Forum*. 381-389 (Wiley Online Library).
- 689 106 Jacobson, A. *Algorithms and interfaces for real-time deformation of 2d and 3d shapes*, ETH Zurich, (2013).
- 690 107 Desbrun, M., Meyer, M., Schröder, P. & Barr, A. H. in *Proceedings of the 26th annual conference on*
691 *Computer graphics and interactive techniques*. 317-324.
- 692 108 Kass, M., Witkin, A. & Terzopoulos, D. Snakes: Active contour models. *International journal of computer*
693 *vision* **1**, 321-331 (1988).
- 694 109 Eilers, P. H. & Boelens, H. F. Baseline correction with asymmetric least squares smoothing. *Leiden University*
695 *Medical Centre Report* **1**, 5 (2005).
- 696 110 Zhou, D., Bousquet, O., Lal, T., Weston, J. & Schölkopf, B. Learning with local and global consistency.
697 *Advances in neural information processing systems* **16** (2003).
- 698 111 Eck, M. *et al.* in *Proceedings of the 22nd annual conference on Computer graphics and interactive techniques*.
699 173-182.
- 700 112 Zou, G., Hu, J., Gu, X. & Hua, J. Authalic parameterization of general surfaces using Lie advection. *IEEE*
701 *Transactions on Visualization and Computer Graphics* **17**, 2005-2014 (2011).
- 702 113 Fong, C. Analytical methods for squaring the disc. *arXiv preprint arXiv:1509.06344* (2015).
- 703 114 Eschweiler, D., Smith, R. S. & Stegmaier, J. in *2022 IEEE International Conference on Image Processing (ICIP)*.
704 191-195 (IEEE).
- 705 115 Stringer, C., Wang, T., Michaelos, M. & Pachitariu, M. Cellpose: a generalist algorithm for cellular
706 segmentation. *Nature methods* **18**, 100-106 (2021).
- 707 116 Telea, A. An image inpainting technique based on the fast marching method. *Journal of graphics tools* **9**, 23-
708 34 (2004).
- 709 117 Panozzo, D., Puppo, E. & Rocca, L. Efficient multi-scale curvature and crease estimation. *Proceedings of*
710 *Computer Graphics, Computer Vision and Mathematics (Brno, Czech Republic)* **1** (2010).
- 711 118 Shewchuk, J. What is a good linear finite element? interpolation, conditioning, anisotropy, and quality
712 measures (preprint). *University of California at Berkeley* **2002** (2002).
- 713 119 Cignoni, P. *et al.* in *Eurographics Italian chapter conference*. 129-136 (Salerno, Italy).
- 714 120 Dean, K. M., Roudot, P., Welf, E. S., Danuser, G. & Fiolka, R. Deconvolution-free Subcellular Imaging with
715 Axially Swept Light Sheet Microscopy. *Biophys J* **108**, 2807-2815, doi:10.1016/j.bpj.2015.05.013 (2015).
- 716 121 Garcia, D. Robust smoothing of gridded data in one and higher dimensions with missing values.
717 *Computational statistics & data analysis* **54**, 1167-1178 (2010).
- 718 122 Chen, B. *et al.* Increasing the field-of-view in oblique plane microscopy via optical tiling. *Biomedical Optics*
719 *Express* **13**, 5616-5627 (2022).

- 720 123 Orieux, F., Giovannelli, J.-F. & Rodet, T. Bayesian estimation of regularization and point spread function
721 parameters for Wiener–Hunt deconvolution. *JOSA A* **27**, 1593-1607 (2010).
722 124 Farnebäck, G. in *Scandinavian conference on Image analysis*. 363-370 (Springer).
723 125 Dean, K. M. *et al.* Diagonally scanned light-sheet microscopy for fast volumetric imaging of adherent cells.
724 *Biophysical journal* **110**, 1456-1465 (2016).
725 126 Vollmer, J., Mencl, R. & Mueller, H. in *Computer graphics forum*. 131-138 (Wiley Online Library).
726